

**UiO** : **Department of Chemistry**  
University of Oslo

**Synthesis and characterisation of  
PEDOT:PSS/silicon interfaces for  
use in low cost, high efficiency solar  
cells**

**Erlend Hall**

Master's Thesis, Spring 2020



# Synthesis and characterisation of PEDOT:PSS/silicon interfaces for use in low cost, high efficiency solar cells

Erlend Hall



M.Sc. Thesis in Materials Science for Energy and  
Nanotechnology  
60 credits

Department of Chemistry  
Institute for Energy Technology  
Faculty of mathematics and natural sciences

UNIVERSITY OF OSLO

Spring 2020

© 2020 Erlend Hall

Synthesis and characterisation of PEDOT:PSS/silicon interfaces for use in low cost, high efficiency solar cells

<http://www.duo.uio.no/>

Printed: Representralen, University of Oslo

# Preface

The work on this master thesis has been conducted as a collaboration between the Light and Electricity from Novel Semiconductors (LENS) group at the University of Oslo and the Solar Energy department at the Institute for Energy Technology from January 2019 to May 2020.

First and foremost, I would like to thank my supervisors, Assoc. Prof. Halvard Haug, Prof. Erik Stensrud Marstein and Prof. Eduard Monakhov. You have all provided invaluable guidance, good ideas and brilliant feedback, for which I am very grateful.

This last term turned out a little different than expected due to the covid-19 pandemic. Nevertheless, you have all pulled through and been supportive from a distance through chat, video calls, emails and phone calls, enabling the finalisation of this thesis.

Halvard, you have really been there to answer all my questions, both big and minuscule. You also deserve thanks for providing lab training and operating the PECVD for me. Erik, you had me sold on solar energy from our first conversation. Thank you for sharing your vast knowledge and enthusiasm of the field and helping me focus on the essentials. Eduard, thank you for being a great resource, providing invaluable insight into my results, good ideas and always cracking a smile.

A big thanks to everyone at LENS and the Solar Department for being inclusive and creating excellent working environments, interesting lunch discussions and joining me in drinking excessive amounts of coffee.

A special thanks to Chang Chuan You and Ørnulf Nordseth for providing me with lab training, supplying wafers and helping me fix broken instruments. Also a big thanks to Damir Zamirov Mamedov, Dmitrii Moldarev, Antonio Vázquez López and Marina García for filling me in on previous work, teaching me the established fabrication process at IFE which this thesis builds on, and keeping me company in the lab.

I would also like to thank Eirik Koch Jubskås for operating the ALD, Espen Førdestrøm Verhoeven for doing DLTS measurements and Kristian Sørnes for providing some very valuable last-minute proof-reading and teaching me how to properly write *et al.*

A huge thanks to my family and friends for your love and support, and always cheering me on. Finally, the warmest thanks to Karoline. Thank you for dragging me up in the morning, providing the ultimate home office experience, your never-ending support and being the greatest motivator of them all.

*Erlend Hall*  
*15.05.2020*  
*Home office, Oslo*

# Abstract

Hybrid solar cells, combining low-cost organic material with the well-known merits of inorganic silicon, have recently attracted significant interest for its great potential as low-cost, high-efficiency solar cells. In this thesis, hybrid solar cells consisting of the polymer poly(3,4-ethylenedioxythiophene):polystyrene sulfonate (PEDOT:PSS) and n-type silicon have been fabricated and characterised. The objectives have been to develop a process for making reproducible PEDOT:PSS/n-Si solar cells with sufficient passivation and good performance. Moreover, to explore the stability of these cells and gain fundamental knowledge regarding the interface between PEDOT:PSS and Si, including the exploration of various interlayers.

Solar cells and symmetrically passivated wafers have been made with various interface treatments and subsequent spin-coating of PEDOT:PSS. The samples have then undergone rigorous characterisation to understand the effect of different interface layers, including their advantages and limitations. Furthermore, the long-term stability of both solar cells and doubly-passivated wafers have been studied.

This work has demonstrated the excellent passivation provided by PEDOT:PSS on n-type Si. This is evidenced by high minority carrier lifetimes, as measured by quasi-steady state photoconductance and photoluminescence imaging, which reflects low surface recombination velocities.

Moreover, the role and limitations of the interfacial layer are thoroughly explored by current-voltage and capacitance-voltage measurements. A regrown  $\text{SiO}_2$  layer grown for 45 min at ambient conditions has provided the best solar cell in this study with an efficiency approaching 10 % by adjusting the active area to a theoretical 5 % shading. It is further shown that all solar cells with a thin interfacial native  $\text{SiO}_2$ , i.e. grown for 15 minutes to 7 days at room temperature, show initially similar performance. However, only the thinnest oxides (15 - 60 minutes growth time) retain the best performance after storage for several months.

The importance of fine-tuning the interface is further demonstrated by a fine line between excellent passivating properties, sufficiently low tunnelling barriers and oxide density. This is particularly displayed by solar cells with a thin interfacial  $\text{Al}_2\text{O}_3$  layer where a difference in oxide thickness of merely 4 Å alters the performance completely. With an oxide thickness of 1.7 nm, the PEDOT:PSS/ $\text{Al}_2\text{O}_3$ /n-Si solar cell shows performance approaching the level of the samples with native  $\text{SiO}_2$ , albeit with some limiting extraction barriers. By increasing the oxide thickness to 2.1 nm, however, the performance is severely diminished with close to no flow of current in the measured range (-1 to 1 V).

Furthermore, this work has, for the first time, explored PEDOT:PSS/n-Si solar cells with interfacial layers of untreated Si wafers, chemically grown SiO<sub>2</sub> using HNO<sub>3</sub> and amorphous silicon. While all these solar cells show extraction barriers, severely limiting the solar cell performance through s-shapes in the current-voltage curves, they provide valuable insight into the limitations and possibilities of tailoring the interface between PEDOT:PSS and Si.

Lastly, this work has shown a significant degradation in both passivation and electrical solar cell performance to occur with exposure to ambient conditions. This has further been shown to stabilise with storage at reduced humidity and reduced temperatures, demonstrating the crucial need for sufficient encapsulation. The fact that PEDOT:PSS/Si solar cells show degradation has been stated often in the literature. However, almost no work has been done to explore the extent of this degradation and obtain a thorough understanding of the mechanisms taking place. In this regard, the extensive long-term stability series presented in this work is a significant contribution to further stability work concerning PEDOT:PSS/Si solar cells.

# Contents

<b>Preface</b>	<b>iii</b>
<b>Abstract</b>	<b>iv</b>
<b>1 Introduction</b>	<b>1</b>
1.1 Aim of study . . . . .	3
1.2 Structure . . . . .	5
<b>2 Theory and Background</b>	<b>6</b>
2.1 Semiconductor physics . . . . .	6
2.1.1 p-n junctions . . . . .	6
2.1.2 S-shaped IV curves . . . . .	11
2.1.3 Oxidation of silicon . . . . .	12
2.2 Carrier recombination and surface passivation . . . . .	14
2.2.1 Recombination mechanisms . . . . .	15
2.2.2 Effective carrier lifetime . . . . .	17
2.2.3 Surface passivation . . . . .	18
2.3 Solar cells . . . . .	18
2.3.1 Solar cell parameters . . . . .	19
2.3.2 Organic photovoltaics . . . . .	19
2.3.3 Organic-inorganic hybrid heterojunction solar cells . . . . .	19
2.4 PEDOT:PSS . . . . .	21
2.5 PEDOT:PSS/c-Si interface . . . . .	23
2.5.1 Passivation by PSS . . . . .	24
2.5.2 Junction formation and current transport mechanisms in PEDOT:PSS	25
2.6 Previous work . . . . .	25
2.6.1 Absorption enhancement . . . . .	27
2.6.2 Modification of the PEDOT:PSS dispersion . . . . .	27
2.6.3 Optimising the interface between PEDOT:PSS and Si . . . . .	28
2.6.4 Optimising the contacts and contact interfaces . . . . .	29

2.6.5	Suggested optimised process . . . . .	29
<b>3</b>	<b>Methods and experimental</b>	<b>31</b>
3.1	Methods for sample processing . . . . .	31
3.1.1	Spin coating . . . . .	31
3.1.2	Contacting . . . . .	32
3.1.3	Thermal evaporation . . . . .	32
3.2	Methods for characterisation . . . . .	33
3.2.1	Current-voltage . . . . .	33
3.2.2	Sheet resistance . . . . .	33
3.2.3	Capacitance-voltage . . . . .	34
3.2.4	Quasi-steady state photoconductance . . . . .	36
3.2.5	Photoluminescence imaging . . . . .	36
3.3	Experimental design . . . . .	38
3.3.1	Materials . . . . .	38
3.3.2	Sample preparation . . . . .	39
3.4	Preliminary testing . . . . .	41
3.4.1	PEDOT:PSS sample preparation . . . . .	41
3.4.2	Fabrication of samples for electrical characterisation and solar cells	42
3.4.3	Experiments on different interfacial layers . . . . .	45
<b>4</b>	<b>Results and Discussion</b>	<b>47</b>
4.1	Passivation by PEDOT:PSS . . . . .	47
4.2	Stability . . . . .	48
4.2.1	Degradation . . . . .	49
4.2.2	Storing at different conditions . . . . .	52
4.2.3	Light-induced enhancement . . . . .	55
4.3	Electrical characterisation . . . . .	56
4.3.1	Sheet Resistance . . . . .	56
4.3.2	Current-voltage . . . . .	57
4.3.3	Growing a native oxide . . . . .	59
4.3.4	Summary . . . . .	62
4.4	The effect of different interfacial layers . . . . .	62
4.4.1	Native SiO <sub>2</sub> grown in ambient . . . . .	62
4.4.2	Aluminium Oxide . . . . .	70
4.4.3	Amorphous silicon . . . . .	74
4.4.4	Chemically grown silicon dioxide . . . . .	76

---

4.4.5	Summary of the various interface layers . . . . .	77
4.5	The PEDOT:PSS/Si solar cell . . . . .	77
4.5.1	Realising the full potential . . . . .	78
<b>5</b>	<b>Concluding remarks</b>	<b>81</b>
5.1	Summary . . . . .	81
5.2	Further work . . . . .	82
	<b>Bibliography</b>	<b>83</b>
	<b>Appendix</b>	<b>i</b>

# 1

## Introduction

The world has an ever-growing need for energy, and providing this energy in a manner which is both socially inclusive and environmentally sustainable is one of the biggest challenges of the 21st century.

According to the United Nations World Population Prospects 2019 [1], the world's population is expected to increase by 2 billion in the next 30 years with a majority of this growth coming from countries of sub-Saharan Africa. In fact, the 47 least developed countries are among the world's fastest-growing. Besides, many countries are experiencing increased living standards. Together, this leads to a highly increased global energy demand [2].

At the same time, global emissions keep reaching historical highs leading to climate changes as evidenced by e.g. accelerated sea levels, ocean warming, ocean acidification and more extreme weather [3].

The energy world is marked by large discrepancies. While wealthy countries are building 5G networks, switching to electric vehicles and developing smart grids, 840 million people in the world still live without access to electricity.

In the Sustainable Development Goals (SDGs), the globally shared blueprint for improving economic prosperity and social well-being while also protecting the environment, access to affordable and clean energy is one of the goals. Energy is central to nearly every major challenge and opportunity the world faces today. Be it for jobs, security, food production or increasing incomes, access to energy for all is essential. Additionally, working towards this goal is especially important as it interlinks with other SDGs [4].

Among the candidates for sustainable sources of energy, solar energy is one of the most promising and the fastest growing, and for good reasons. Solar cells elegantly utilise the photovoltaic (PV) effect to convert sunlight directly into electricity. Solar energy is available over the entire globe and highly abundant - in a single hour, the solar radiation hitting the earth contains more energy than the entire annual human energy consumption. It should hence come as no surprise that the International Energy Agency predicts Solar PV to become the largest component of global installed capacity in the Stated Policies Scenario as seen in figure 1.1 [2].

For this to become a reality, however, further advances are required in terms of better efficiencies, lower cost and suitable infrastructure.

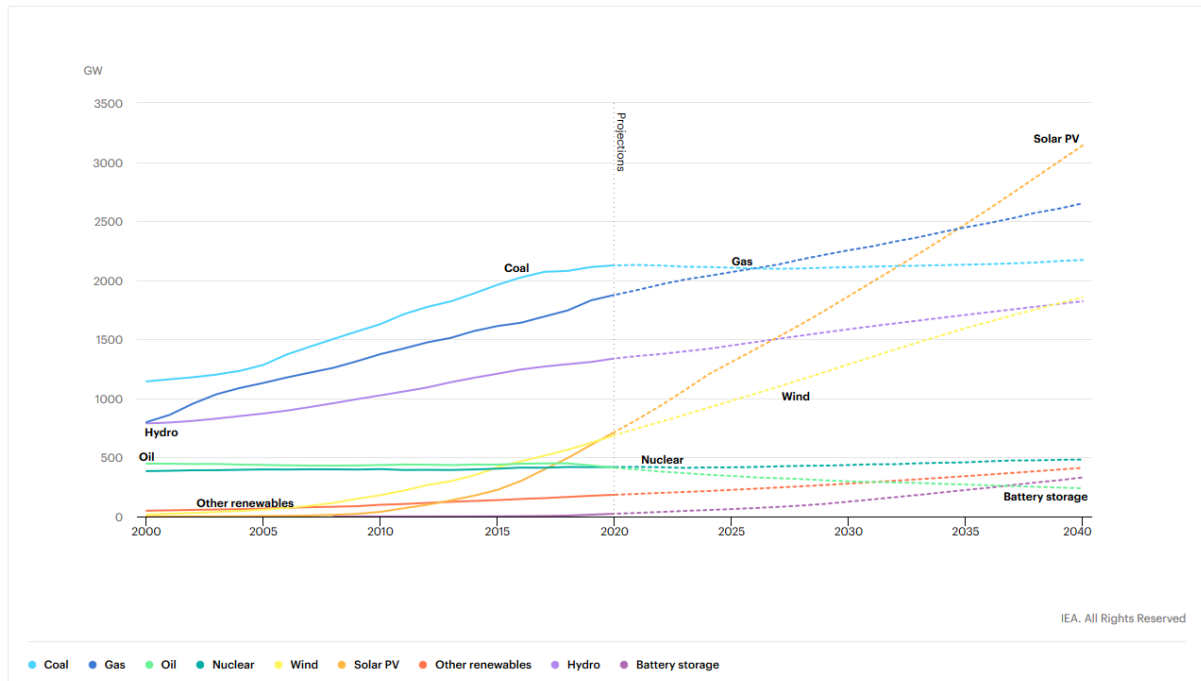


Figure 1.1: Installed power generation capacity by source in the Stated Policies Scenario, 2000-2040. Solar PV is predicted have a tremendous growth and overtake coal and gas before 2035. Source: IEA(2019) World Energy Outlook. All rights reserved.

Silicon (Si) is widely considered to be the material of choice for solar cells, with Si-based technologies accounting for more than 95% of the globally produced cells in 2017 [5]. Nowadays, with improved passivation, wafer quality and optimised structures, high-end single-junction silicon solar cells are approaching the theoretical Shockley-Queisser limit. In short, this means that they are starting to become as good as they ever can be. Further advances should thus be obtained by reducing the cost of manufacturing.

Compared to conventional energy sources, such as oil and gas, the cost of silicon solar cells has finally started to become competitive. However, to further accelerate the growth of solar cells and make solar cells a viable option even in the most impoverished rural areas of the world, a further cost reduction is needed.

Commercial Si solar cells are typically made by a high-temperature diffusion (900–1100 °C) of phosphorus into p-type silicon, creating an n-type emitter and a p-type base. By adding a few additional steps to increase the light absorption and passivation, an Aluminium Back Surface Field (Al-BSF) Si solar cell is made. From the cost overview of such a cell, shown in figure 1.2, 23% of the cost comes from the diffusion step.

By going from such a Si homojunction to a heterojunction consisting of Si and some other material, plenty of possibilities emerge. One up-and-coming candidate combining low cost and high efficiency is the hybrid organic-inorganic solar cell. One such solar cell is the silicon-organic heterojunction which has been actively studied in the last 10 years [6]–[12]. This typically consists of a Si absorber base and an organic emitter, coupling existing mature Si wafer technology with a low-temperature solution-based emitter formation process.

This means that one, by going from a Si homojunction to an organic-inorganic heterojunction, may achieve a price reduction of almost 25%, provided a viable low-cost alternative [13].

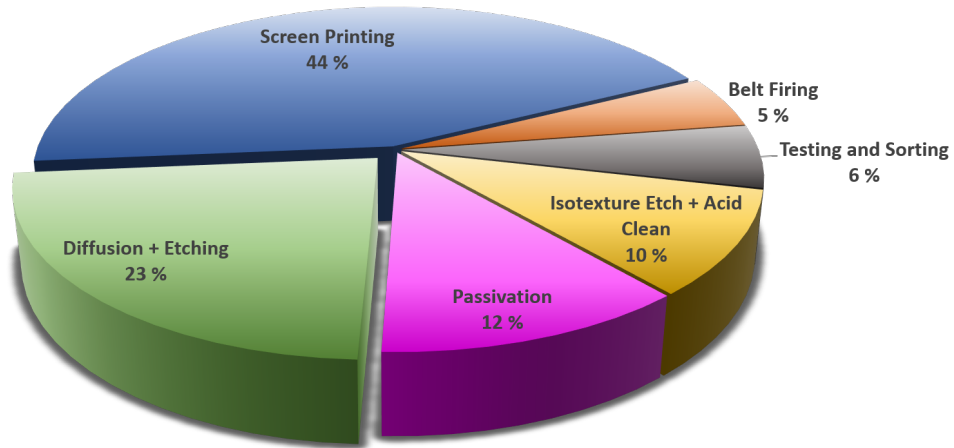


Figure 1.2: Overview of the cost of different processes in a common Al-BSF Si homojunction solar cell. Diffusion and etching accounts for 23%. Adapted from [13].

This type of organic-inorganic hybrid solar cell has gained considerable interest in recent years, combining the excellent properties of silicon, such as high carrier mobility, excellent stability and established fabrication processes with benign, low-cost organic material exhibiting properties such as low-temperature solution processability and flexibility of organic chemistry, making it possible to tune energy levels as well as luminescent and conducting properties.

One of the most promising candidates for this type of solar cell is based on the p-type conducting polymer poly(3,4-ethylenedioxythiophene):polystyrene sulfonate (PEDOT:PSS) on a crystalline silicon (c-Si) substrate.

## 1.1 Aim of study

Several authors have shown the great potential of organic-inorganic hybrid heterojunction solar cells, in particular the PEDOT:PSS/c-Si cell. PEDOT:PSS is particularly interesting because of its p-type conductivity, high light transmittance and availability as an aqueous dispersion, making for simple device processing. Furthermore, the hole mobility and conductance in PEDOT:PSS are reported to be much higher than those of most other polymers [14].

Overall, the technology has shown power conversion efficiencies of 10–17% for small area research-scale devices with PEDOT:PSS on the front side. The record efficiencies to date are 17.6% with the junction on the front side [15] and 20.6% with a backside junction [12]. However, several groups have also reported cells with considerably lower efficiencies

with very similar procedures, pointing to some critical aspects of fabrication which may not be completely understood. Moreover, most of the cells exceeding 13% are fabricated with energy-demanding processes which increase the fabrication cost.

Significant improvements to the cell performance have, among others, been credited to better interface control. However, there are relatively few studies of the PEDOT:PSS/Si interface and conflicting reports regarding the nature of the interface and the effects of various interlayers.

Furthermore, little is known about the long-term stability of this solar cell. With the exception of Schmidt et al [10], reports about the degradation of these cells have been scarce. This is a little surprising considering that organic material tends to degrade when exposed to ultraviolet radiation, humidity, and in some cases, even oxygen - all of which a solar cell typically is exposed to. Since solar modules are expected to maintain a relatively high power output through at least 20 years, understanding the mechanism of degradation and finding ways to enhance long-term stability is of tremendous importance.

This work aims to further develop the process and ensure reproducibility in the fabrication of PEDOT:PSS/Si solar cells. Furthermore, it aims to obtain a deeper understanding of the properties and limitations, especially related to the interface between the polymer and Si, along with the overall stability. This can be divided further into the following aims:

- Validate the passivating properties of PEDOT:PSS and ensure homogeneity.
- Study the stability of passivation.
- Optimise the process to obtain a fully operational hybrid PEDOT:PSS solar cell with suitable rectifying properties.
- Perform a comprehensive study of the stability of fabricated solar cells, both concerning the passivating properties represented by minority carrier lifetimes and the solar cell performance represented by the open-circuit voltage, short-circuit current, fill factor and the efficiency.
- Explore different interlayers between PEDOT:PSS and Si.
- Obtain a deeper understanding and control of the interface between PEDOT:PSS and Si.

The majority of the literature utilises a native silicon dioxide ( $\text{SiO}_2$ ) or a hydrogen (H)-terminated surface as the interface. Little or no reports exist on different interlayers or the use of an un-treated Si wafer.

## 1.2 Structure

This thesis is divided into five chapters. The present chapter (Chapter 1) intends to place the work in a broader context together with a short motivation for the work. Moreover, specific aims for the present study are defined, which will be answered throughout this thesis.

To start off after this introduction, Chapter 2 presents the relevant theory to discuss the findings from this work. General theory regarding p-n junctions, carrier recombination, surface passivation and solar cells is given together with more specific theory regarding PEDOT:PSS and the PEDOT:PSS/Si interface. Finally, the chapter provides a brief overview of the history and previous work.

This is closely followed by short descriptions of the methods used for synthesis and characterisation and a detailed description of the experimental work conducted, together with some preliminary testing, in Chapter 3.

Chapter 4 consists of the results and a thorough discussion of these. The chapter is divided into sections of results from various series of experiments, aiming at keeping a reasonable structure based on the nature of the results and what can be understood from them. The chapter starts by showing the passivation provided by PEDOT:PSS and its stability. Then, initial electrical characterisation is presented before the focus shifts to the effect of different interfacial layers and their stability. Lastly, the optimal process is reviewed, and steps for further improvements are discussed.

Last but not least, Chapter 5 provides concluding remarks on the main results and suggestions for further work.

# 2

## Theory and Background

In the following chapter theory regarding photovoltaics, deposition and characterisation relevant for the thesis is presented. This is followed by specific theory regarding PEDOT:PSS and the PEDOT:PSS/Si interface and concludes with a review of previous work. The chapter is mostly based on Reinders [16], Nelson [17], Smets [18] and Streetman [19].

### 2.1 Semiconductor physics

In the following, basic knowledge within semiconductor physics is assumed, herein crystal structures, energy bands and charge carriers. The interested reader is referred to one of many excellent textbooks on the area, such as Reinders [16], Smets [18], Streetman [19] or Schroder [20].

#### 2.1.1 p-n junctions

The p-n junction is the heart of many solar cells. A p-n junction formed by different doping in the same material is called a homojunction (figure 2.1). If two semiconductors of different band gap form the junction, the term used is heterojunction (figure 2.2).

In order to extract any of the generated charge carriers in a solar cell, there is a need for a built-in skewness, or asymmetry, to avoid the generated carriers to simply recombine straight after they are formed. An electric field may provide this asymmetry, separating the charges as they are generated and thus helping them reach the contacts of the device.

By the joining of a p-type and an n-type material, majority charge carriers will diffuse from their carrier-rich side to the carrier-deficient side. Electrons will thus move from the n-type material to the p-type material, and holes will move the opposite way. This flow of carriers leaves behind uncompensated ionised acceptors and donors in a region close to the junction. This creates the desired built-in electric field and defines the space charge region (SCR), also known as the depletion zone due to its depletion of free charge carriers. The built-in voltage can be found considering the difference in work function at each side of the junction.

At equilibrium, the charge carriers will diffuse until the diffusion and drift current are exactly balanced. Now the Fermi levels are aligned, causing the conduction and valence

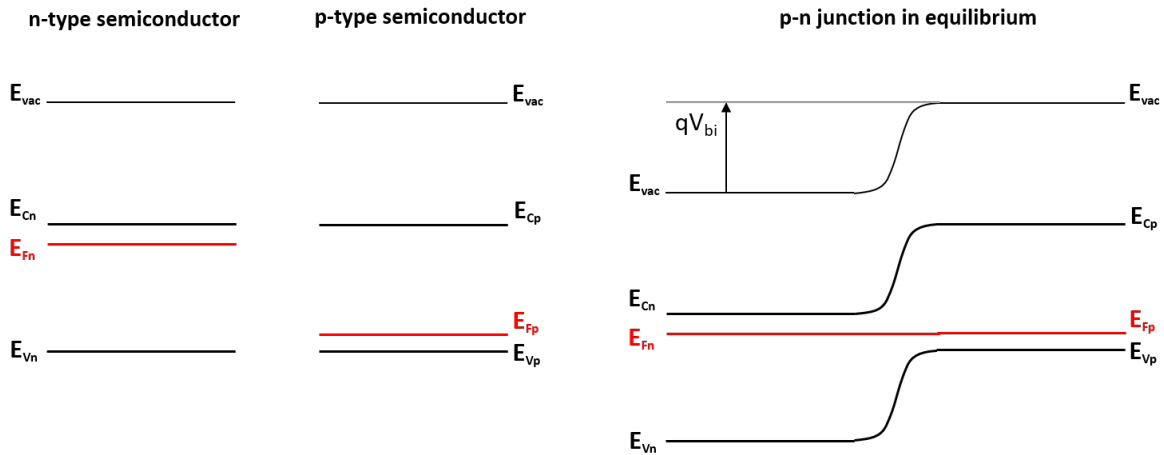


Figure 2.1: Band profiles of a p- and n-type semiconductor of the same material, and thus the same band gap, before (left) and after (right) forming a junction.

bands to bend and consequently creating a barrier for electrons in one direction, and holes in the other. This provides the rectifying behaviour characteristic of a diode.

The Fermi level,  $E_F$ , represents the averaged energy of electrons in a material and describes the energy up to which states are filled at absolute zero. At finite temperature some electrons will be excited into states above  $E_F$  due to thermal energy.

Other important physical quantities are the electron affinity,  $\chi$ , and the vacuum level,  $E_{vac}$ .  $E_{vac}$  is the energy of an electron just outside of any influence from the solid, or atom, and  $\chi$  is the potential that an electron present in the conduction band requires to be elevated to  $E_{vac}$ . Lastly, the work function,  $\phi$ , which applies to both semiconductors and metals, is the energy required to remove an electron from the Fermi level to  $E_{vac}$ .

## Heterojunction

With the formation of a heterojunction, the band gaps will not be of equal size. As seen in figure 2.2, there will then exist a discontinuity in the conduction and valence band edges due to the different band gaps. This step in potential leads to different effective fields for the minority carriers, usually assisting the electrostatic field for one carrier type and opposing it for the other. Such barriers can lead to enhanced recombination in the junction region.

## Interface states

Solid surfaces are likely to contain some degree of defects and impurities. The interruption of the crystal lattice at the surface and adsorbed impurity atoms will cause intrinsic and extrinsic defects, respectively. These defects often introduce different electronic states with energies within the band gap. This will make the defects capable of trapping charge and thus influence the potential distribution across the interface.

Interface states cannot alter the net potential difference across the junction, which always equals the difference in work functions. However, they influence how said potential

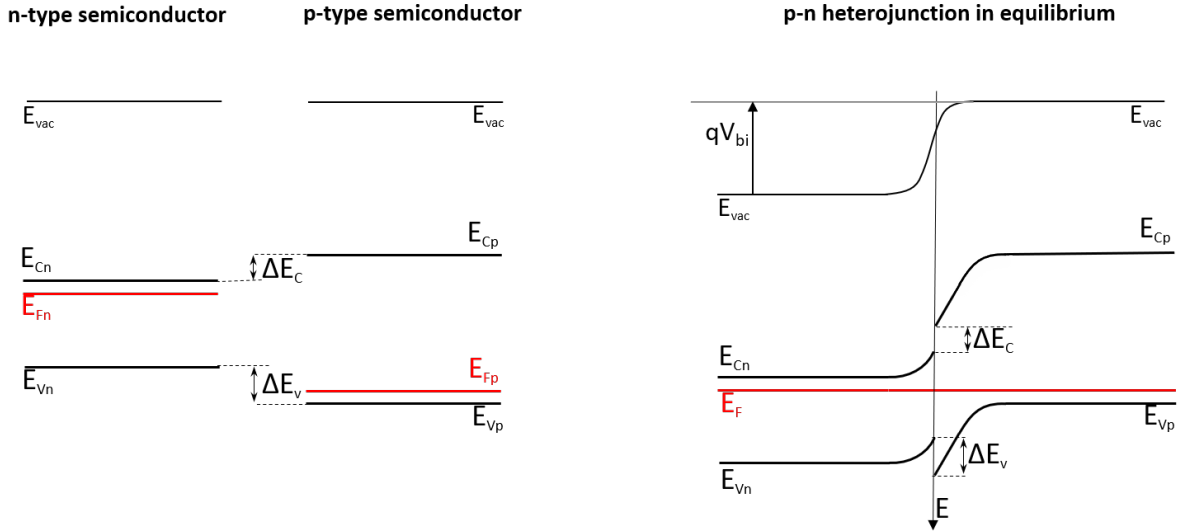


Figure 2.2: Band profiles of a p- and n-type semiconductor of two materials with different band gaps, before (left) and after (right) forming a heterojunction.

is divided between the two materials. If the interface states trap negative charge, a smaller negative space charge needs to be developed in the p-side to compensate the positive charge on the n-side. Consequently, more of the potential difference is dropped on the n-side, which again may lead to an inversion layer of accumulated mobile holes on the n-side.

### Ideal p-n Diode in the Dark

Solar cells typically behave like diodes in the dark, admitting a much larger current in forward bias ( $V > 0$ ) than in reverse bias ( $V < 0$ ), in other words displaying a rectifying behaviour. In the simplest case with infinite shunt resistance and negligible series resistance, the dark current density  $J_{dark}(V)$  varies like

$$J_{dark}(V) = J_0(e^{qV/nk_B T} - 1) \quad (2.1)$$

where  $q$  is the electron charge,  $V$  is the applied bias,  $k_B$  is Boltzmann's constant and  $T$  is the temperature. Further,  $J_0$  is the saturation current density which is due to carrier diffusion in the quasi-neutral region and given by

$$J_0 = qn_i^2 \left( \frac{D_n}{L_n N_A} + \frac{D_p}{L_p N_D} \right) \quad (2.2)$$

where  $n_i$  is the intrinsic carrier concentration,  $D_n(D_p)$  is the electron (hole) diffusion coefficient,  $L_n(L_p)$  is the electron (hole) diffusion length and  $N_A(N_D)$  is the concentration of acceptors (donors). Its derivation is lengthy and can be found elsewhere [17], [18].

$J_0$  is an important parameter for a diode, reflecting the recombination in the device. The saturation current density is typically a very small number, on the order of 100 fA/cm<sup>2</sup> in Si. The ideality factor,  $n$ , describes the ideality of the diode where  $n = 1$  for an ideal,

diffusion current limited diode and  $n = 2$  for an SCR recombination current limited diode. A fitted ideality factor greater than 2 may be found in heterojunctions due to tunnelling through barriers. However, its physical significance is limited besides the fact that it points to a reduced fill factor of the solar cell.

### IV under illumination

By illuminating the solar cell, electron-hole pairs are generated, and the electron and hole densities are enhanced above their equilibrium values, leading to a flow of the minority carriers across the depletion region. This flow of photogenerated carriers causes the photogeneration current density,  $J_{ph}$ , which moves in the opposite direction of current flow under bias. The current-voltage (IV) characteristics now become a superposition of the dark IV and a light-generated current

$$J(V) = J_0(e^{qV/nk_B T} - 1) - J_{ph}$$

Without any external electrical contact between the n- and p-type regions, the junction is in open circuit. Hence, no current is flowing out of the device, and the current resulting from generated carriers has to be balanced by the opposite recombination current. In the open-circuit condition, the electron and hole quasi-Fermi levels are split by  $qV_{oc}$  with the open-circuit voltage,  $V_{oc}$ , being the maximum value for the voltage.

Experimentally,  $V_{oc}$  occurs when the dark current and short-circuit photocurrent cancel out

$$V_{oc} = \frac{k_B T}{q} \ln \left( \frac{J_{sc}}{J_0} + 1 \right) \quad (2.3)$$

where the short-circuit photocurrent,  $J_{sc}$ , (i.e no applied voltage) is equal to the photogeneration current for an ideal diode. Figure 2.3 shows the current-voltage characteristics of a p-n diode in the dark and under illumination.

### Real solar cells

In real cells, power is lost through resistive effects and leakage currents. In the diode model (equation 2.4), the series resistance,  $R_s$ , acts in series with the diode while the shunt resistance,  $R_{sh}$ , acts in parallel. As a consequence, efficient cells have a low series, and a high shunt resistance.

$$J = J_0 \left( e^{\frac{q(V+JAR_s)}{k_B T}} - 1 \right) - \frac{V + JAR_s}{R_{sh}} - J_{sc} \quad (2.4)$$

Series resistance may occur from high-resistivity absorber materials or from charge transport in the contact materials. Shunt resistance may occur through pin holes, the absence of proper minority charge carrier blocking layers or edge currents.

Moreover, the current is not purely originating from minority carrier diffusion, but also recombination current from the SCR, also referred to as generation-recombination current. This also has a lengthy derivation which can be found elsewhere [17] and has the approximate form

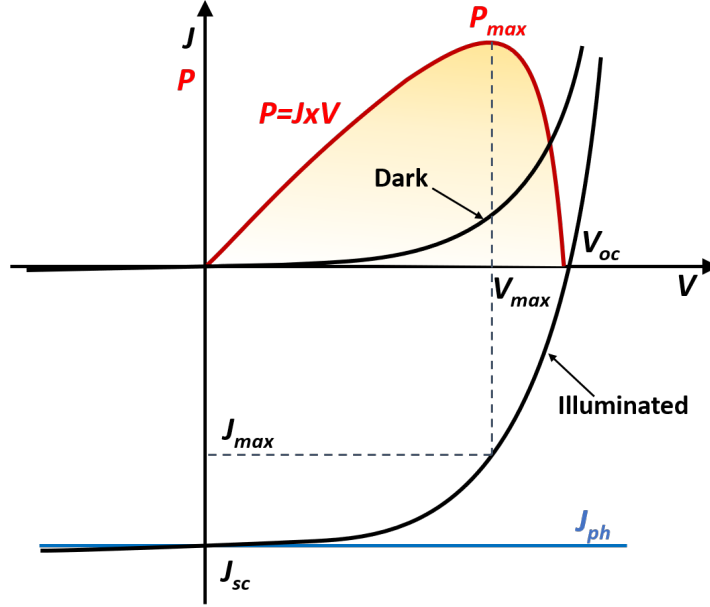


Figure 2.3: Current-voltage characteristics of p-n diode in the dark and under illumination. Adapted from [18].

$$J_{scr}(V) = J_{scr,0} \left( e^{\frac{qV}{2k_B T}} - 1 \right) \quad (2.5)$$

where  $J_{scr,0}$  takes the width of the space charge region,  $\omega_{scr}$ , and the electron(hole) lifetime,  $\tau_n(\tau_p)$ , into account:

$$J_{scr,0} = \frac{qn_i(\omega_{scr})}{\sqrt{\tau_n \tau_p}} \quad (2.6)$$

To account for this, especially at low bias or under low illumination, the current-voltage characteristics should be described by the two-diode model where  $J_{01}$  corresponds to the dark saturation current density from bulk diffusion (equation 2.2) and  $J_{02}$  accounts for trap-assisted generation and recombination processes in the space-charge region (equation 2.6):

$$J = J_{01} \left( e^{\frac{q(V-JR_s)}{k_B T}} - 1 \right) + J_{02} \left( e^{\frac{q(V-JR_s)}{2k_B T}} - 1 \right) - \frac{V - JR_s}{R_{sh}} - J_{sc} \quad (2.7)$$

This model includes area specific serial and parallel resistances as well as current contributions from diffusion and recombination in the bulk, and generation and recombination at defects in the space charge region.

$J_{02}$  will tend to dominate the IV curve at lower voltage bias. By examining a logarithmic plot of current density (figure 2.4), we can usually see a marked change in the slope between the SCR and diffusion-dominated regions of the dark IV curve.

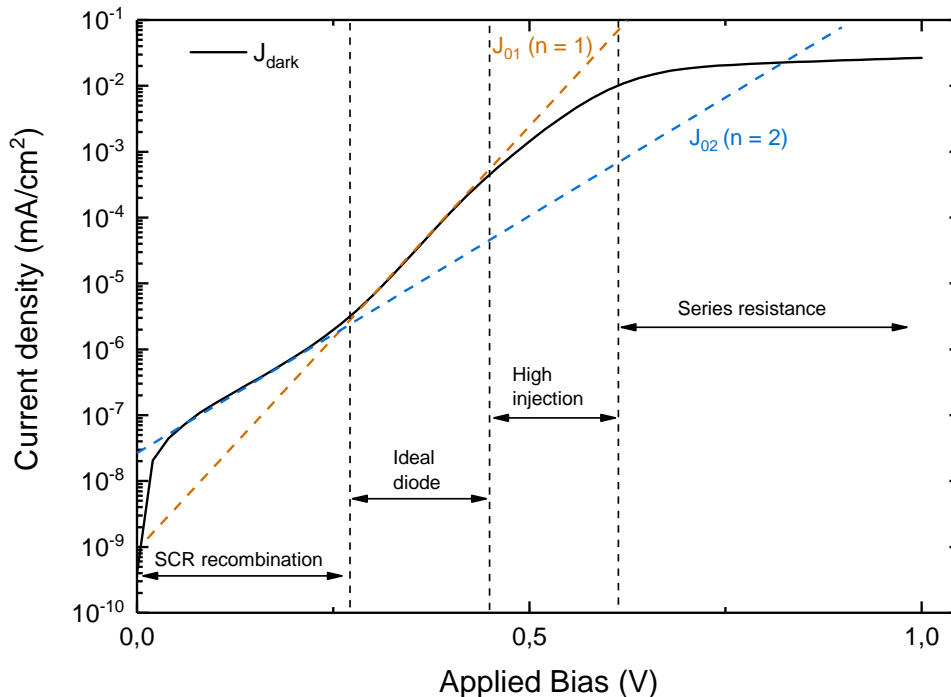


Figure 2.4: Dark current of a real non-ideal diode, resolved into different regions and contributions. From a solar cell with PEDOT:PSS/SiO<sub>2</sub>/n-Si.  $J_{02}$  corresponding to SCR recombination dominates at low bias, while the diffusion-limited  $J_{01}$  dominates at higher bias before high injection causes an increased recombination and ultimately the series resistance dominates.

### 2.1.2 S-shaped IV curves

S-shaped IV characteristics, as depicted in figure 2.5, are a quite common and dreaded obstacle encountered when developing novel solar cell concepts. Pointing to the existence of a charge transport bottleneck, it needs to be removed in order to get high fill factors and power conversion efficiencies. A variety of causes, mechanisms and mitigations have been proposed by several authors [21]–[25] from which this section is based.

The simple modification to the IV curve with a constant series and shunt resistance shown previously is not sufficient to explain the occurrence of s-shapes. In addition to reducing the fill factor, the mechanism causing the s-shape often reduces  $V_{oc}$  and  $J_{sc}$  as well.

In silicon heterojunction (SHJ) solar cells, s-shapes have been attributed to unfavourable band alignment between Si and the passivating contact, charge transport blocking due to intermixing of layers and high band offset leading to a high charge transport barrier.

In organic solar cells, interface dipoles, unfavourable selective contacts and potential drop at interfaces are found as the culprit. Furthermore, Tress *et al.* [22] observed that a mismatch factor of more than 100 between hole mobility in the donor and electron mobility in the acceptor leads to the onset of s-shaped IV curves. Wagner *et al.* [23] observed the importance of proper energetic alignment between the absorber and the contact material in order to avoid s-shapes.

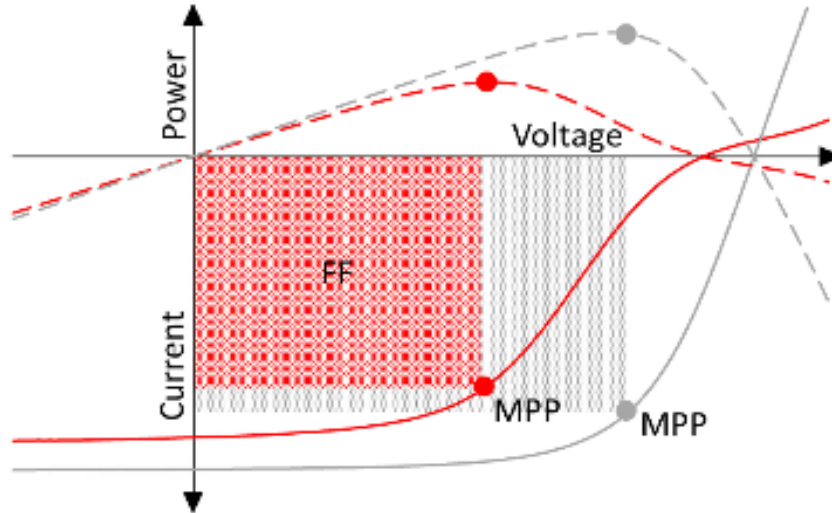


Figure 2.5: Expected (grey curve) and s-shaped (red curve) current-voltage and power-voltage characteristics. The severe effect on FF is evident. Reproduced from [21].

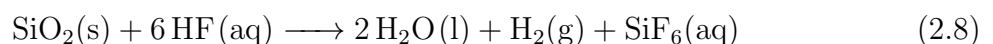
In perovskite solar cells, s-shaped behaviour has been found to increase after storage in the dark and after light soaking under reverse bias. A hole extraction barrier was determined as the culprit by Tress and Inganäs [25]. An extraction barrier implies that charges cannot leave the device because the interface (layer) is not well-conducting or shows a huge energy barrier for charges when being extracted. Chemical degradation of the metal contact leading to charge extraction barriers has also been suggested.

In summary, the s-shaped IV-curves mostly arise from a mismatch between the energy levels of the absorber layer and the charge extraction layer, or the contact interface, resulting in a barrier for charge extraction. Energy onset at the interface to PEDOT:PSS corresponds to the hole injection barrier at the acceptor-donor interface. A reduction of this barrier reduces the series resistance and thus decreases the s-shaped behaviour. Additionally, decreasing the thickness of passivating, charge blocking, or buffer layers has been shown to mitigate the s-shape.

### 2.1.3 Oxidation of silicon

One of the reasons for silicon's conquering of the electronics industry is that it very easily forms a high-quality insulating oxide when bound to oxygen,  $\text{SiO}_2$ . Often, an oxide layer from tens to hundreds of nm is desired; for instance, to form gate oxides or fully isolate the active devices on a transistor. In the role as an interface layer, this changes to merely 0–2 nm to enable tunnelling of electrons and holes.

Before a controlled oxide layer can be produced, the natural oxide layers, various contaminations and impurities need to be removed. This wafer cleaning is done by hydrofluoric acid (HF) which reacts with  $\text{SiO}_2$  through the following overall reaction



Solutions of HF are highly selective of oxide over silicon and the etching is completely isotropic [26].

Straight after HF cleaning, most of the Si atoms on the surface are terminated by hydrogen, causing the surface to be hydrophobic.

Depending on whether dry O<sub>2</sub> or H<sub>2</sub>O is used in the oxidation, the process is referred to as dry oxidation (2.9) or wet oxidation (2.10).



For both methods, Si is consumed from the surface of the substrate. Initially, the oxidant directly reaches Si atoms on the surface. Subsequently, the oxidant molecules have to diffuse through the already grown oxide to the Si–SiO<sub>2</sub> interface in order to keep oxidising Si. Said diffusion is highly kinetically limited at room temperature. This is why, for instance, gate oxides in transistors typically are grown thermally. In the case of a thin interface oxide, however, this limited diffusion can be exploited to grow a very thin, native oxide at room temperature.

### Native oxide growth

Morita *et al.* studied the native oxide growth in air and ultrapure water at room temperature [27]. Measuring an accurate thickness of SiO<sub>2</sub> layers of only a couple Å is not an easy task. Nevertheless, by employing a combination of ellipsometry and x-ray photoelectron spectroscopy (XPS), the obtained thicknesses should be reliable as long as the atomic density of the native oxide is equal to that of the thermal oxide.

Their results from oxidation in air (figure 2.6) display indications of a step-wise growth with an initial thickness of 0.19 nm, mainly credited to the rinsing with ultrapure water and drying procedure after a diluted HF treatment. This thickness stays constant until about 1000 min where the thickness increases to 0.54 nm and a succeeding increase to 0.76 nm after roughly  $2 \times 10^4$  min. After seven days of exposure ( $10^4$  min), an oxide thickness of 0.67 nm was measured. These experiments were conducted for n-type Cz (100) wafers with a resistivity of 2–4 Ωcm. The wafers were stored in a clean room with an average temperature of 23.7°C and average humidity of 42 % (1.2 % H<sub>2</sub>O in the air).

Similar experiments performed by Raider *et al.* showed a negligible change in oxide thickness from 2 weeks to 1 year and estimated an equilibrium oxide thickness of less than 14 Å in air at room temperature unless the substrate dopant concentration is higher than  $10^{19} \text{ cm}^{-3}$  [28].

### Nitric acid oxidation

Kobayashi *et al.* showed that ultrathin SiO<sub>2</sub> layers can be formed by immersion of Si in nitric acid (HNO<sub>3</sub>) [29]. They showed that immersion of an HF etched Si sample in 68 wt% HNO<sub>3</sub> at 121°C formed a 1.4 nm SiO<sub>2</sub> layer after 10 min, and further immersion did not change the thickness. They also oxidised Si samples with 61 wt% HNO<sub>3</sub> at both room

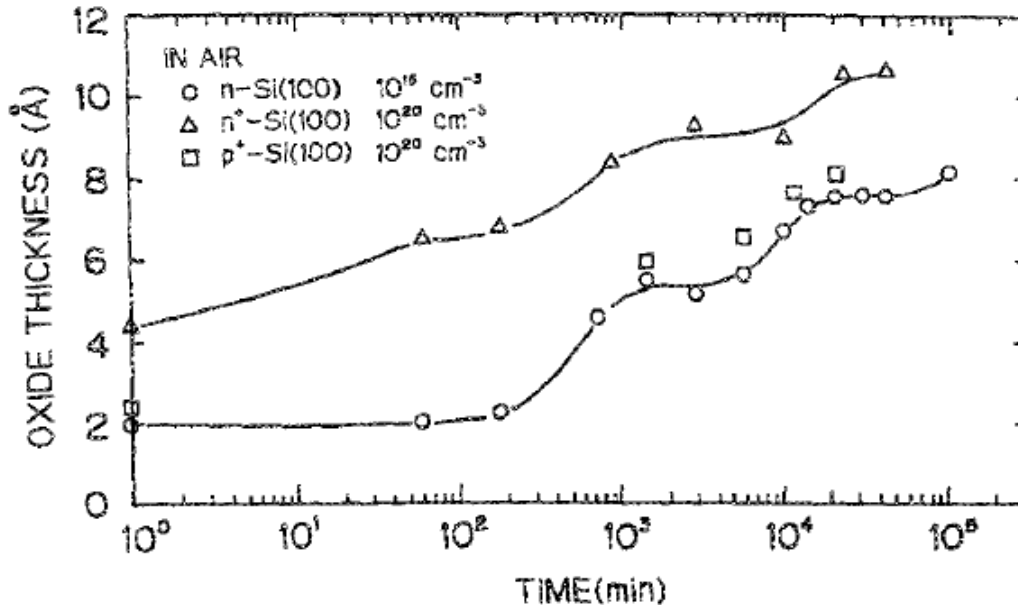


Figure 2.6: Oxide thickness as a function of exposure time of wafers to air at room temperature. There is a clear step-wise growth corresponding to growth of consecutive mono-layers. The circles correspond to n-Si with orientation (100) and a donor concentration of  $10^{16} \text{ cm}^{-3}$ . From [27].

temperature and elevated temperatures. At room temperature, the  $\text{SiO}_2$  had a thickness of 0.7 nm after 10 min and followed a parabolic increase up to  $\sim 1$  nm after 8 h. Their work was directed at its application to gate oxides in transistors, but the relatively good thickness control makes this process interesting for our interface oxides. The oxidation proceeds at low temperatures due to a high concentration of atomic oxygen produced by the decomposition of  $\text{HNO}_3$ . The oxidation occurs in two steps, where nitric acid first decomposes following equation 2.11 and the resulting high concentration of atomic oxygen is able to oxidise Si at low temperatures.



## 2.2 Carrier recombination and surface passivation

The following section is mostly based on Reinders [16] and Haug [30].

One major factor limiting the efficiency of solar cells is carrier recombination, where generated electrons and holes recombine before they contribute to the collected current.

Generation is a process that occurs in all semiconductors, which increases the density of free charge carriers. Two of the basic processes which stimulate this is thermal generation and photogeneration. Thermal generation occurs due to lattice vibrations, called phonons, and photogeneration occurs due to photons with energy higher than, or equal to, the band gap of the semiconductor. The latter occurs when the semiconductor is exposed to light. From the principle of microscopic reversibility, this process naturally needs a counterpart where generated carriers relax back to their ground state. That is, a free electron in

the conduction band combines with a hole in the valence band, and the excess energy is released. Consequently, the system returns to thermal equilibrium. This process is termed recombination and can be measured experimentally as the recombination lifetime  $\tau$ , defined by

$$\tau = \frac{\Delta n}{U} \quad (2.12)$$

with  $\Delta n$  being the excess carrier concentration and  $U$  the recombination rate.

### 2.2.1 Recombination mechanisms

There are three types of recombination in the bulk of a semiconductor: radiative recombination, Auger recombination and recombination through defects. Of these types of recombination, radiative and Auger are intrinsic, meaning they are a fundamental property of the material being used. On the other hand, recombination through defects is dependent on the purity of the material.

#### Radiative recombination

Radiative recombination is the direct recombination of an electron in the conduction band with a hole in the valence band, resulting in the emission of a photon with energy corresponding to  $E_g$ . It is the opposite process of optical generation and a dominant mechanism in direct bandgap semiconductors, such as GaAs. The radiative recombination rate is given by the difference in the non-equilibrium electron-hole population from the intrinsic thermal carrier population,  $n_0 p_0 = n_i^2$

$$U_{rad} = B_{rad}(np - n_i^2) \quad (2.13)$$

where  $B_{rad}$  is the material-specific radiative recombination coefficient and  $n(p)$  is the electron (hole) concentration. Si, being an indirect band gap material has a  $U_{rad}$  considered to be small or even negligible compared to other recombination mechanisms. It is, however, relevant for lifetime measurements based on photoluminescence.

#### Auger recombination

Auger recombination is a three-particle interaction where the energy of the photogenerated carrier is dissipated by increasing the kinetic energy of another free carrier. This kinetic energy is then very quickly dissipated through thermalisation. Similarly to radiative recombination, the recombination rate is given as the product of the concentrations of the involved carriers

$$U_{Aug} = (C_n n + C_p p)(np - n_i^2) \quad (2.14)$$

where  $C_n$  ( $C_p$ ) is the electron (hole) Auger coefficient. Since this is a three-carrier process, the rate varies as the square of one of the carrier types. Thence, Auger recombination dominates for very high injection levels or in heavily doped regions.

### Non-radiative (Shockley-Read-Hall) recombination

To some extent, defects will be present in any semiconductor. These defects may lead to spatially localised energy levels within the band gap and are often referred to as trap states due to their ability to trap free carriers. This can often be a huge contribution to the recombination through a two-step process where the trap captures an electron and a hole, making them recombine at the trap; or for instance, capturing an electron which then relaxes to the valence band and annihilates a hole. This recombination process is called Shockley-Read-Hall (SRH) recombination, after the scientists who first investigated this type of trap-assisted recombination behaviour [31], [32]. The rate is given by

$$U_{SRH} = \frac{np - n_i^2}{\tau_{p0}(p + p_1) + \tau_{n0}(n + n_1)} \quad (2.15)$$

where  $\tau_{n0}$  ( $\tau_{p0}$ ) is the electron (hole) capture time constants, representing the minimum lifetime for electrons (holes) when all traps are filled with carriers of the opposite type. The carrier densities  $n_1$  and  $p_1$  represent the electron and hole densities if the Fermi level would be at the defect energy level,  $E_t$ :

$$\tau_{n0} = \frac{1}{\sigma_n N_t \nu_{th}}, \quad \tau_{p0} = \frac{1}{\sigma_p N_t \nu_{th}} \quad (2.16)$$

$$n_1 = n_i \exp\left(\frac{E_t - E_i}{k_B T}\right), \quad p_1 = n_i \exp\left(\frac{E_i - E_t}{k_B T}\right) \quad (2.17)$$

Here,  $N_t$  is the defect (trap) concentration,  $\sigma$  represents the capture cross sections for each carrier,  $\nu_{th}$  is the carrier thermal velocity,  $n_i$  is the intrinsic carrier concentration and  $E_i$  is the intrinsic energy level.

### Surface recombination

At the surface of a semiconductor, the periodicity of the crystal lattice is abruptly terminated, introducing localised states at the surface consisting of dangling unpassivated bonds, adsorbed impurity molecules or local stress in the crystal lattice. These trap states form an almost continuous distribution across the band gap, as shown in figure 2.7, and is therefore a significant source for carrier recombination if left unpassivated.

This recombination can be treated similar to the bulk SRH recombination, merely formulated in terms of recombination per surface area instead of volume. For a surface with a single, effective defect level with a density  $N_{it}$ , the surface recombination rate is given by

$$U_S = \frac{S_{n0} S_{p0} (n_s p_s - n_i^2)}{S_{n0} (n_s + n_1) + S_{p0} (p_s + p_1)} \quad (2.18)$$

where  $n_s$  and  $p_s$  are the surface electron and hole concentrations.  $S_{n0}$  and  $S_{p0}$  are the effective surface recombination parameters, defined as

$$S_{n0} = \sigma_n N_{it} \nu_{th}, \quad S_{p0} = \sigma_p N_{it} \nu_{th} \quad (2.19)$$

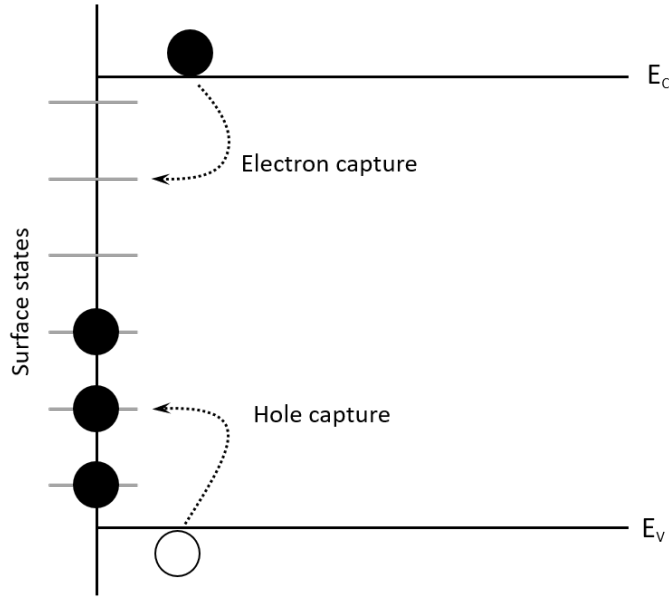


Figure 2.7: Electron and hole capture at the surface of a semiconductor. Adapted from [16].

To accommodate the recombination rate at the surface we use the surface recombination velocity (SRV),  $S$ , defined as the surface recombination rate divided by the excess carrier concentration at the surface  $\Delta n_s$ , leading to the inverse form of equation 2.12:

$$\frac{1}{S} = \frac{\Delta n_s}{U_s} \quad (2.20)$$

The SRV is measured in cm/s and a high SRV corresponds to a high recombination activity at the interface. Unpassivated surfaces or low quality interfaces can have SRVs as high as  $10^5 - 10^6$  cm/s whereas a good surface passivation can reduce this value towards or even below 1 cm/s.

### 2.2.2 Effective carrier lifetime

All the recombination mechanisms explained above will typically occur simultaneously in a semiconductor. The total bulk recombination rate is simply the sum of the different contributions,  $U_b = U_{rad} + U_{Aug} + U_{SRH}$ . Since the lifetime is inversely proportional to the recombination rate, as seen in equation 2.12, the total bulk lifetime is given by

$$\frac{1}{\tau_b} = \frac{1}{\tau_{rad}} + \frac{1}{\tau_{Aug}} + \frac{1}{\tau_{SRH}} \quad (2.21)$$

For a symmetrically passivated sample with a small  $S$ , which is the case for the samples presented in this thesis, the effective lifetime is given by

$$\frac{1}{\tau_{eff}} = \frac{1}{\tau_b} + \frac{2S}{W} \quad (2.22)$$

where  $W$  is the sample thickness.

### 2.2.3 Surface passivation

Surface recombination may have a tremendous impact on solar cell performance, especially when reducing the cell thickness. Consequently, there is a need to increase the effective lifetime of the wafer by reducing the SRV at the surface. This is accomplished by surface passivation.

There are two different strategies to passivate the surface, often used in combination to achieve sufficiently low SRVs. The recombination rate is directly proportional to the interface defect density,  $D_{it}$ . Hence, one strategy is to simply reduce the number of defects at the interface, often referred to as chemical passivation. This can typically be achieved by the deposition of a dielectric film on the c-Si surface. By growing a thermal  $\text{SiO}_2$  followed by an anneal in  $\text{H}_2$ , the interface state density  $D_{it}$  can be reduced by several orders of magnitude to values of  $10^9 \text{ eV}^{-1} \text{ cm}^{-2}$  [16], [30]. Other methods for chemical passivation include creating a clean hydrogen-terminated surface by stripping off the native oxide layer in an HF solution and depositing amorphous hydrogenated silicon (a-Si:H).

The other strategy is to reduce the concentration of one of the charge carriers at the interface since the surface recombination process requires the presence of both electrons and holes. Termed field-effect passivation, this is accomplished by having an internal field below the surface. This internal field can be obtained by the application of a doping profile below the interface, or by the presence of a fixed charge density,  $Q_f$ , in a dielectric layer on the surface.

A doping profile is often used to passivate the rear of the Si solar cell and is referred to as a back surface field (BSF). Alternatively, in the case of a solar cell with the junction placed on the backside, the equivalent front surface field (FSF) is often used. Here, a high-low (same polarity, i.e.  $p^+p$  or  $n^+n$ ) doped junction acts as a barrier to the minority carrier, and simultaneously serves as a passivation layer for the defects at the contact interface, allowing higher minority carrier densities in the bulk [18].

## 2.3 Solar cells

Solar cells are based on exciting electrons from electron states with low energy, known as the valence band (VB), to electron states with higher energy, termed the conduction band (CB). This excitation occurs by absorption of photons. If now these electrons can be extracted from the high energy states, some of this increased energy can be harvested before the electrons are re-instated to their low-energy states.

The basic processes of solar cell operation are absorption of photons generating charge carrier pairs, separation of these carriers at the junction and collection of the photogenerated charge carriers at the terminals of the junction.

When dealing with organic material, the equivalents of the VB maximum and CB minimum are the Lowest Unoccupied Molecular Orbital (LUMO), and the Highest Occupied Molecular Orbital (HOMO), respectively.

### 2.3.1 Solar cell parameters

To characterise and quantify the performance of solar cells, the main parameters used are the peak power,  $P_{max}$ , open-circuit voltage,  $V_{OC}$ , short-circuit current density,  $J_{SC}$ , the fill factor,  $FF$ , and the conversion efficiency,  $\eta$ . These should be measured under standard test conditions (STC), meaning that the total irradiance on the solar cell is  $1000 \text{ W/m}^2$  with a spectrum resembling AM1.5 and the solar cell kept at a constant temperature of  $25^\circ\text{C}$ .

The power density of a solar cell is given by

$$P = JV \quad (2.23)$$

The maximum power occurs at some voltage  $V_{max}$  with a corresponding current density  $J_{max}$ . The 'squareness' of the J-V curve is described by the fill factor, FF, which is defined as the ratio

$$FF = \frac{J_{max}V_{max}}{J_{sc}V_{oc}} \quad (2.24)$$

The efficiency  $\eta$  of the cell is the ratio between the maximum power density and the power density of the incident light

$$\eta = \frac{P_{max}}{P_s} = \frac{J_{max}V_{max}}{P_s} \quad (2.25)$$

and by using equation 2.24, the efficiency becomes

$$\eta = \frac{J_{sc}V_{oc}FF}{P_s} \quad (2.26)$$

The four quantities  $J_{sc}$ ,  $V_{oc}$ ,  $FF$  and  $\eta$  are the key performance characteristics of a solar cell.

Another important quantity is the quantum efficiency, QE, defined as the probability that an incident photon of a given energy will deliver one electron to the external circuit. This is dependent on the absorption coefficient of the solar cell material and the efficiency of charge separation and collection.

### 2.3.2 Organic photovoltaics

There are a lot of interesting concepts among purely organic photovoltaics, all of which are outside the scope of this thesis. The interested reader is referred to the excellent books by Reinders [16], Tress [33] and Leo [34].

### 2.3.3 Organic-inorganic hybrid heterojunction solar cells

Organic-inorganic hybrid (OIH) solar cells are a fairly new concept which aims at exploiting the merits of both organic and inorganic material. The goal being, in general, to pursue high solar cell efficiencies and low cost.

Generally, solar cells containing organic components have had lower efficiencies than the more traditional inorganic solar cells. However, the low fabrication cost, lightweight and flexibility of organic materials made them suitable for several special applications. In theory, OIH solar cells should be able to adopt the merits of inorganic materials, namely high carrier mobility, stability and compatible fabrication process and simultaneously utilise the advantages of organics.

The general operating principle of organic solar cells involves light absorption, exciton generation and diffusion, exciton dissociation to carriers at the junction interface and carrier transportation and collection. Excitons, which are bound electron-hole pairs, are dissociated into holes and electrons by the built-in electric field at the interface [35].

However, Fan *et al.* showed that the average exciton diffusion lengths are usually shorter than 20 nm in most organic semiconductors, which implies that most of the excitons are quenched before carriers are formed [35]. Thus, the utilised carriers will be the ones generated in silicon and then separated by the junction; consequently, OIH solar cells behave very similarly to pure inorganic solar cells.

Silicon is dominant in the PV market, extensively studied, and one of the most attractive materials for OIH solar cells.

Regarding energy band alignment and effective carrier collection, the following criteria should be satisfied by the organic and inorganic materials: Firstly, for a high photocurrent, the offset between the VB of the inorganic component and the HOMO of the organic component should be small. Secondly, to obtain a high open-circuit voltage, the offset should be large between the CB of the inorganic component and the LUMO of the organic molecule [35].

Figure 2.8 shows a schematic band diagram and operation principle of an organic-inorganic hybrid heterojunction. A charge selective interface promotes the transport of holes to the organic acceptor, while the large offset between  $E_{LUMO}$  and  $E_C$  provides an efficient electron barrier.

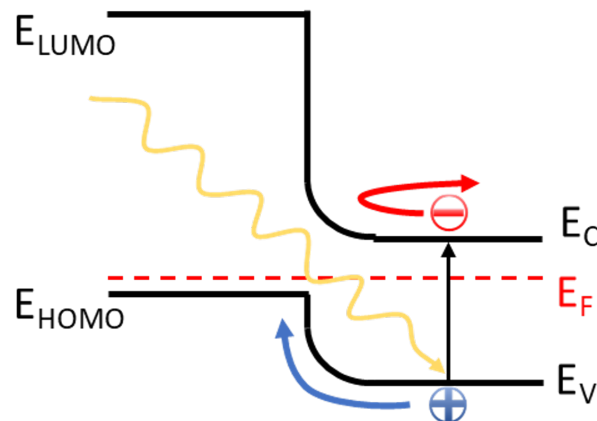


Figure 2.8: Schematic band diagram and operation principle of the OIH PEDOT:PSS/n-Si heterojunction. Adopted from [36].

## 2.4 PEDOT:PSS

Poly(3,4-ethylenedioxythiophene):polystyrene sulfonate (PEDOT:PSS), shown in figure 2.9 has gained considerable interest in recent years as an important conducting polymer. This is mainly contributed to its high conductivity, optical transparency, suitable work function and aqueous form, making it attractive in low-cost processing for hybrid solar cells [37].

Conductive polymers, which were discovered and developed in 1977 by Chiang *et al.* [38], can be either extrinsically or intrinsically conducting. While the former is a polymer that has become conductive by some additive, the latter are conductive on their own due to a conjugated backbone chain - the main chain of the polymer in which all other chains are connected. This leads to a system of delocalised  $\pi$ -bonds and the formation of a band gap between a completely unfilled and a completely filled molecular orbital.

For conjugated polymers, by far the highest conductivity is found in polythiophenes such as PEDOT, especially in a complex with PSS. PSS acts as a charge counterbalance to the oxidised PEDOT backbone during polymerisation and enables highly doped states. As a result, PEDOT:PSS is a very efficient hole transporter with a transmission window in the spectral range. Furthermore, the addition of PSS realises a stable micro-dispersion making the solution easy to process [39].

The specific properties of PEDOT:PSS may be modified by additives to suit different applications. By adding the organic solvent dimethyl sulfoxide (DMSO), the transport properties in the PEDOT:PSS film are optimised [39], leading to even higher conductivity. Furthermore, the addition of a surfactant such as Triton X-100 enhances the wetting and thus the coverage of PEDOT:PSS on Si during spin coating.

Photovoltaic devices combining PEDOT:PSS and crystalline silicon were first proposed in 2005 by Williams *et al.* [40] and have since then received increasing interest as a candidate for high-efficiency, low-cost silicon solar cell technology.

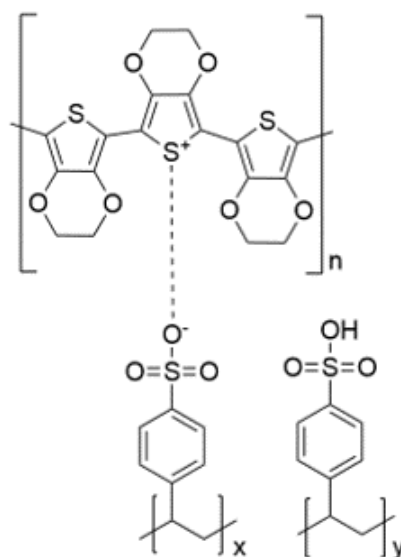


Figure 2.9: The chemical structure of PEDOT:PSS.

### Analysis with a tail state model

The following section is based on Ho *et al.* [41]. The PEDOT:PSS layer serves as both hole transport layer and electron blocking layer. PEDOT:PSS is not like a traditional p-type semiconductor layer where a large density of acceptors is doped to generate a high density of holes. Instead, holes are injected into PEDOT:PSS through its high density of tail states.

The carrier transport property of organic materials is quite different from the carrier transport property of semiconductors. While the electrons/holes in the semiconductor move along the conduction/valence band, carriers in the organic material move by hopping in the molecular orbitals. Unlike inorganic materials, there are still hopping and trapping phenomena inside the band gap of an organic material. This leads to two specific properties: Organic materials can absorb light with photon energy smaller than the band gap energy, and carriers can hop into tail states or be caught by trap states when transporting in the organic material. The tail states near the HOMO of PEDOT:PSS helps to transport holes generated in Si to the PEDOT:PSS layer.

Ho *et al.* proposed that the depletion junction is almost solely confined to the PEDOT:PSS layer due to the smaller relative dielectric constant of PEDOT:PSS compared to Si. Therefore, the electric field in the Si layer is small, leading to stronger recombination near the  $V_{oc}$ . Consequently, chemical passivation is crucial to the device performance.

### Degradation mechanisms

The conductivity of PEDOT:PSS is determined by both the transport of hole polarons into the PEDOT segments and their hopping between segments and grains. In a material consisting of conductive grains embedded into an insulating matrix, thermal degradation can be considered as corrosion – a process which is reducing the size of the grains and consequently enhancing their distance, or equivalently increasing the potential barrier for polaron transport between them [42].

Vitoratos *et al.* [42]. explored the effect of thermally ageing PEDOT:PSS at 120°C for 55 h. They found that the work function of the surface decreases from 4.7 eV to 3.7 eV at the end of the heat treatment, attributed to the removal of the insulating PSS from the surface, which leaves an area enriched in PEDOT [42].

At the first stage of heating, the PSS chains are perplexed and the agitation of the  $\text{Cl}^-$  ions, attached weakly to the hole polarons on the PEDOT oligomers, makes them wander further away from the polaron vicinity, increasing the mobility of the latter. This makes the grains more conductive. At a second stage of the heat treatment, the ionic bonds between the PEDOT oligomers and the PSS chains start to break and finally the bonds fully break down.

In fresh samples, there is an excess of PSS at the surface, which is removed by the heat treatment. Decrease of the work function due to the decomposition of PEDOT:PSS, as Diels-Alder reaction ( $\text{SO}_2$ -extrusion) starts at higher temperatures (225-230°C) [42].

In conclusion, the PEDOT:PSS will not decompose at temperatures below 200°C,

but the bonds between PEDOT and PSS will ultimately break, leading to a decreased conductivity after prolonged exposure to 120°C. This is, however, much higher than typical operating temperatures for solar cells. Moreover, Vitoratos *et al.* showed that heating of the PEDOT:PSS thin film at a maximum of 443 K (170 °C) for 10 min could be beneficial for the conductivity.

Degradation in PEDOT:PSS has also been attributed to oxidative processes within the PEDOT-chains causing interruption of the free charge carrier percolation. These processes are promoted by UV-light and humidity but can be significantly slowed down by a hermetical seal to ambient, by depositing a UV absorption layer, and by applying stabilising additives to the polymer dispersion [43]. Elschner *et al.* also showed that the degradation proceeds faster for thin layers (25 nm) than for thick ones (98 nm) [43].

## 2.5 PEDOT:PSS/c-Si interface

Several authors have shown that a thin native SiO<sub>2</sub> layer significantly enhances solar cell performance compared to cells with just an H-terminated Si surface [8], [36], [44]–[46]. This is credited to the crucial intermediate region provided by the SiO<sub>2</sub> layer which leads to favourable internal electric fields at the interface and reduces the density of interface traps. The SiO<sub>2</sub> layer can not be too thick since a thick oxide layer could create an insulating barrier for electrical transport and thereby reduce the solar cell performance.

Thomas *et al.* [45] used TOF-SIMS to obtain 3D chemical images; these revealed micropore defects at the PEDOT:PSS/SiO<sub>2</sub>/Si interface, which are more apparent with increasing thickness of the native oxide layer. The lowest micropore defect densities, and subsequently highest power conversion efficiencies, were found with native oxide layers naturally grown for one and three hours on the silicon substrate [45].

According to He *et al.* [8] native oxides on the Si surface of a suitable thickness could improve the efficiency from 0.02% to 10.6% compared to a cell with an H-terminated surface. The native oxide layer had a net positive surface dipole and resulted in a favourable band alignment for charge separation. However, the thick oxide layer at the interface increased the series resistance and degraded the cell performance. The thick SiO<sub>2</sub> was found to form a barrier for charge transfer and hence reduce the open-circuit voltage and fill factor of the cells.

The extremely poor efficiency of a solar cell with an H-terminated surface was attributed to a blocking internal electric field induced at the interface.

Figure 2.10 shows energy band diagrams of the PEDOT:PSS/Si heterojunction with an H-terminated Si surface and with a thin SiO<sub>2</sub> interlayer. Bulk Si has an electron affinity ( $\chi_{Si}$ ) of 4.05 eV. However, a covalently bonded passivation layer on the Si surface can either increase or decrease the effective electron affinity ( $\chi_{eff}$ ) at the Si surface relative to that in bulk Si, depending on the polarity of the associated dipole [47], [48].

Synchrotron photoemission study has demonstrated that the H-Si surface would pose a net negative surface dipole of 0.12 eV upon the formation of the covalent H-Si surface

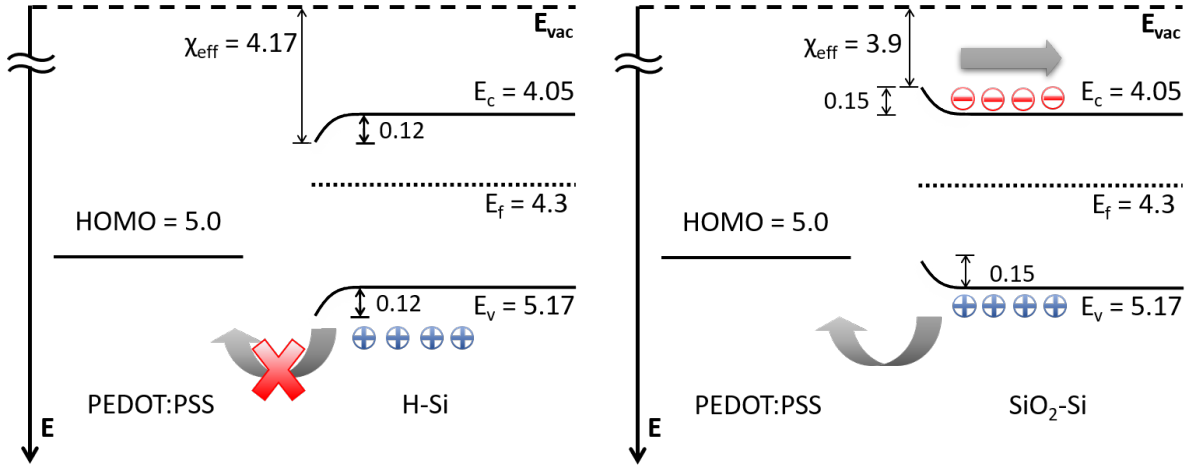


Figure 2.10: Energy band diagrams of the PEDOT:PSS/H-Si (left) and PEDOT:PSS/SiO<sub>2</sub> (right) junctions. The positive effect of a thin SiO<sub>2</sub> is evident in the favourable band alignment. Adapted from [8].

bonding [49]. This leads to an increase in  $\chi_{eff}$  up to 4.17 eV at the Si surface and thus a downward bending of the Si energy band by 0.12 eV near the PEDOT:PSS/Si junction interface. This results in the existence of a blocking internal electrical field which prevents the photoexcited holes in the Si from injecting into PEDOT, resulting in higher carrier recombination at the interface.

The SiO<sub>2</sub>-Si surface, on the other hand, exhibits a net positive surface dipole of 0.15 eV [50], leading to a  $\chi_{eff}$  of 3.9 eV. Now, the Si energy band will bend upward and give rise to a favourable alignment between SiO<sub>2</sub>-Si and PEDOT:PSS to promote carrier separation. Moreover, the SiO<sub>2</sub> layer helps in suppressing the silicon SRV. Thus, lower carrier recombination at the SiO<sub>2</sub>-Si/PEDOT:PSS interface and higher  $J_{sc}$  is expected.

Interface engineering is critical to increase performance; it can optimise the carrier separation [51], minimise interfacial recombination [14] and strengthen the inversion effect [52]. Several advances in these regards are presented in section 2.6.

### 2.5.1 Passivation by PSS

PEDOT:PSS provides good chemical passivation for Si surfaces. Chen *et al.* [53] found that the passivation effect is mainly due to the PSS species rather than the PEDOT ones. Furthermore, the passivation of the Si surface by PSS obeys an electrochemical oxidation mechanism at the PSS/Si interface. This mechanism can be controlled by electron transfer at the Si surface shown by the redox reaction in equation 2.27

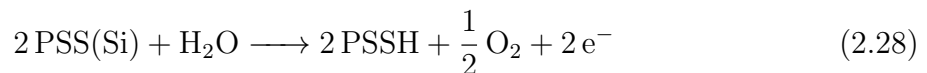


Here, Si represents dangling bonds at the Si surface, and R is the surplus O-containing constituent in the PSS molecule, or simply hydrogen after breakaway of hydroxyl (R'-O-H) from PSS.

Upon light soaking (LS), the passivation is further enhanced by a light-induced effect. Photoexcited electron-hole pairs are created in the Si absorber and then separated by the internal electric field,  $E_{in}$ . This field stimulates the transport of holes across the PEDOT:PSS/Si interface, which drives the forward reaction in equation 2.27 and results in further oxidation of the Si surface. Consequently, the interface defect states are reduced and the minority carrier lifetime increases.

This electrochemical behaviour is reversible, so some time after stopping LS the effect is subdued and the minority carrier lifetime returns to its initial value. However, since solar cells operate in an LS environment, this is considered inconsequential. The oxidation is so rapid that any effects going from night to day should be negligible.

Oxygen can diffuse through PEDOT:PSS thin films due to the gas permeability of the material. At the PSS/Si interface, the penetrating oxygen can oxidise the Si surface and transform it into an electron donor. This will, in turn, accelerate the forward reaction in Eq. 2.27 and lead to further oxidation of the Si surface by PSS, which improves passivation. Water, on the other hand, will be absorbed by PSS making PSS an electron donor via:



This will clearly contribute electrons to the Si surface, favouring the reverse reaction in Eq. 2.27 and degrading the passivation.

### 2.5.2 Junction formation and current transport mechanisms in PEDOT:PSS

In a p-n junction, the transport processes are dominated by the diffusion of minority carriers, as opposed to a Schottky diode where the majority carriers dominate transport. Jäckle *et al.* [39], [46], [54] showed that the transport across the PEDOT:PSS/Si junction is governed by diffusion of minority charge carriers and not by thermionic emission of majority carriers over a Schottky barrier. Thus, PEDOT:PSS forms a hybrid heterojunction with n-Si, similar to a conventional p-n junction.

Further, they showed that PEDOT:PSS induces a strong inversion at the silicon surface due to the accumulation of holes [55]. The n-type silicon is completely converted to p-type silicon at the interface to the polymer and hybrid PEDOT:PSS/n-Si solar cells should, therefore, be described as abrupt  $p^+n$ -heterojunctions [39].

## 2.6 Previous work

The first silicon solar cell was reported in 1954 by Chapin, Fuller and Pearson [56] and had an efficiency of 6%. This was about six times higher than previous attempts, but the production cost compared to the power generated was still too high. Nonetheless, the possibility of getting electricity in remote locations caused silicon solar cells to be widely developed for applications in space during the 1950s and 60s.

The oil crisis in the 1970s led to an increased interest in, and funding for, photovoltaics and despite lacking widespread commercial development, this period is credited to a majority of our understanding of the science of PV and advances in processing technology. Along with growing awareness of the need to secure alternative sources of energy to fossil fuels in the 1990s, interest in PV expanded further, and the prices dropped primarily through economies of scale.

Reports on the study of the photovoltaic effect in organic solid-state materials date back to only a few years after the discovery of the silicon solar cell, and between 1978 and 1986, several thin-film solar cells with efficiencies exceeding 1% were reported [57]–[59]. In recent years, efficiencies exceeding 10% have been achieved in pure organic semiconductors [9], [60].

Sailor *et al.* reported one of the first hybrid heterojunctions in 1990 [61] and in 2005 and 2006 PEDOT:PSS and PEDOT:BF<sub>3</sub> was used with a Si base layer by Williams *et al.* [40] and Chen *et al.* [62], respectively. The more widespread interest, however, did not appear until Avashti *et al.* realised the first hybrid solar cell with an efficiency exceeding 10% in 2011 [6] with a PEDOT:PSS/poly(3-hexylthiophene) (P3HT)/Si structure. Here, the junction is formed between the P3HT and Si, with PEDOT:PSS acting as a conductivity enhancer. In the next year, He *et al.* [8] reported the first pure PEDOT:PSS/Si cell with similar efficiency.

Schmidt *et al.* [10] reported a 12.3% efficient cell with random pyramid texture and Al-BSF, albeit with significant degradation of the efficiency after 100 h. The same research group has had great success with moving the PEDOT:PSS to the backside with a record efficiency of 18.3% and 20.6% on respectively n- and p-type silicon, reported by Zielke *et al.* [11], [12]. The BackPEDOT concept has also been implemented in a 15.6 x 15.6 cm<sup>2</sup> p-type Si/PEDOT:PSS solar cell with a phosphorous-diffused emitter and high-T-fired screen-printed Ag grid reaching an efficiency of 20.2% [63]. It is worth noting that these structures have involved diffused emitters and anti-reflective coatings (ARC) that require vacuum, high temperature, or both, somewhat defying the purpose of fabricating low-cost solar cells. Nevertheless, it is very useful to demonstrate the potential of these cells.

While 20.6% is the highest reported efficiency to date, a lot of effort has gone into reaching an equally high efficiency on solar cells with PEDOT:PSS on the front side, and preferably while still keeping production costs low. Until 2015, the highest reported efficiencies on planar PEDOT:PSS/Si solar cells were  $\sim$  13%, credited to optimised PEDOT:PSS blend or solvent treatment [64]–[66], improved passivation and contacting on the rear side [10], [67], [68] or improved PEDOT:PSS interface [8], [36], [44], [46], [69].

In 2015, Liu *et al.* [70] achieved 15.5% through the use of titanium dioxide (TiO<sub>2</sub>) ARC and in 2018, the technology took a further leap by exceeding 16.5% on a planar structure [71] and a record of 17.3% by Yoon and Khang [72] by the combination of a hierarchical structure, optimised blend and thickness of PEDOT:PSS, and siloxane oligomers to enhance the interfaces of both top and bottom contacts.

The solar cell efficiency is fundamentally determined by optical absorption in the silicon absorber, charge transport associated with organic morphology and contact properties, as well as various carrier recombination mechanisms [73]. The potential improvements thus lie in enhancing the absorption of light, optimising the PEDOT:PSS blend, optimising the PEDOT:PSS interface and improving the contact interfaces. Summaries of advances for the different areas are given below.

### 2.6.1 Absorption enhancement

There have been numerous attempts at employing various surface texturing, including traditional random pyramids by anisotropic chemical etching [10], [74], nanostructures by metal-assisted chemical etching, and hierarchical structures by combining the two former [15], [72], [75].

The different nanostructures attempted involve nanowires [76]–[79], nanopyramids [44], [80], nanoarrays [14], nanotubes [81], nanocones [82] and nano-stalagmites [83]. Several groups have also used nanostructures embedded in PEDOT:PSS to enhance light absorption, increase the effective area and shorten the carrier diffusion distance. However, aggregation of the nanowires are in the majority of the cases limiting the performance to  $\sim 9\%$  due to severe carrier recombination at the interface and poor junction quality. Moreover, the fabrication of nanostructures typically involves some complicated fabrication processes, which again defies the purpose of a low-cost fabrication.

The inherent challenge with textured surfaces of any kind is to obtain full coverage of PEDOT:PSS on the surface. The pyramidal structures are made by anisotropic chemical etching, such as potassium hydroxide (KOH) or Tetramethylammonium hydroxide (TMAH), resulting in pyramids with "V"-shapes in the valleys between neighbouring pyramids. Dai *et al.* [74] used a mixed acid solution to curve the bottom of the pyramids via isotropic etching and obtained uniform conformal contact between PEDOT:PSS and Si. This was also utilised on the record cells by Yoon *et al.* [15], [72].

Other promising advances have been made with applying a layer on top of PEDOT:PSS to act as a capping layer. He *et al.* [51] applied the water-insoluble phthalic acid ester, diethyl phthalate (DEP) onto the PEDOT:PSS layer. This provided external tensile stress which resulted in tight contact between PEDOT:PSS and textured Si. An antireflection coating consisting of molybdenum oxide ( $\text{MoO}_3$ ) [84] or  $\text{TiO}_2$  [70] has also been utilised.

### 2.6.2 Modification of the PEDOT:PSS dispersion

Numerous efforts have been made to enhance the conductivity and wetting of PEDOT:PSS by adding co-solvents in the solution and by post-treatments on its thin-film form. Effective co-solvents include DMSO [64], [85], [86], ethylene glycol (EG) [37], [87], methanol [66], [87] and sorbitol [88], [89]. Among the wetting agents, the most frequently used are Triton-X100 [8], [45], [90] and Zonyl fluorosurfactant [65].

Halbich *et al.* [88], [89] found 4 wt% sorbitol to be a great candidate in the case of BackPEDOT due to a reduction in infrared parasitic absorption and improved passivation quality. Interestingly, Halbich *et al.* claimed that the PEDOT:PSS layer should be as thin as possible and reported the best efficiency with a 67 nm layer, while Zhang *et al.* [47] reported the best efficiency with a 200 nm layer of PEDOT:PSS. It appears as though excellent efficiencies can be obtained with a range of PEDOT:PSS thicknesses, especially for the back junction.

Enhancements have also been made by the removal of PSS and reduction of film thickness, both of which can be achieved by post-deposition washing with methanol. Regulating the spin speed also modulates the thickness. Thomas *et al.* [37] found that methanol fills the micropores on the Si surface and helps to rearrange the PEDOT grains to a closer packing, enhancing the charge carrier transport and suppressing the interface defect generation. Liu *et al.* [70] have also had success with post-treatment of p-toluenesulfonic acid and DMSO.

### 2.6.3 Optimising the interface between PEDOT:PSS and Si

Interfacial engineering between n-Si and PEDOT:PSS is of tremendous importance since a high-quality interlayer is critical to allow photogenerated carriers to pass through the heterojunction interface effectively. The most common procedure in the literature is to use an ultrathin native SiO<sub>2</sub> or an H-terminated Si surface. It is worth noting that several publications claim to have an H-terminated surface after an HF etch followed by subsequent rinsing in water, and in some cases also some time in ambient before further fabrication. After Morita *et al.* [27], we expect a monolayer of SiO<sub>2</sub> to grow on the bare Si almost immediately when submerging the wafer in water. It thus seems likely that some (or all) of the literature claiming to use an H-terminated surface actually has a very thin SiO<sub>2</sub> layer. This may explain the controversy where several authors show that the insertion of SiO<sub>2</sub> greatly enhances solar cell performance compared to a similar cell with an H-terminated Si surface [91], [92] while others show that H-terminated Si surface could also lead to decent performance [93], [94].

Nevertheless, the majority makes use of a native oxide made from 1 to 3 h growth in ambient conditions after etching [12], [45], [64] and there is a consensus that a poor interface, e.g. with misaligned energy bands or severe microvoids is detrimental to the performance.

Several other interlayers have also been tested. Yoon *et al.* [72], [90], [95] added an ultrathin (<0.5 nm) siloxane layer and further optimised the interface by thinning the insulating PSS with methanol washing. This resulted in the best, reported cell to date.

He *et al.* [71] utilised a bilayer of PEDOT:PSS films; a high-conductivity top layer formed by doping PEDOT:PSS with 1-ethyl-3-methylimidazolium tricyanomethanide, and a high-adhesion bottom layer formed by doping PEDOT:PSS with (3-glycidoxypropyl)trimethoxysilane.

Nam *et al.* [96] and Ling *et al.* [97] used a thin  $\text{Al}_2\text{O}_3$  layer at the interface. Nam *et al.* determined the optimal thickness to be 2.3 nm and found the hydrophilicity of  $\text{Al}_2\text{O}_3$  to improve the coating of PEDOT:PSS. Ling *et al.* found that the hole-selectivity was enhanced compared to  $\text{SiO}_2$ /PEDOT:PSS.

Other reported interfaces include 1,1-bis[(di-4-tolylamino)phenyl]cyclohexane [73], tungsten oxide [52], P3HT [85], polyethylenimine and methyl-terminated Si [98].

### 2.6.4 Optimising the contacts and contact interfaces

The importance of passivating the rear Si surface and optimising the contacts have also been pointed out by several authors. Liu *et al.* [99] tested both [6,6]-Phenyl-C61-butyric acid methyl ester and conjugated polymer poly{[N,N'-bis(2-octyl dodecyl)-naphthalene-1,4,5,8-bis(dicarboximide)-2,6-diy]-alt-5,5'-(2,2'-bithiophene)} (N2200) between Si and the Al back contact to act as a hole blocking layer and make an ohmic contact. Of the two, N2200 led to slightly better performance.

Zhang *et al.* [67] inserted a caesium carbonate ( $\text{Cs}_2\text{CO}_3$ ) layer between Si and Al, creating a better ohmic contact and a BSF. He *et al.* [71] used a solution-processed C60 pyrrolidine tris-acid which also reduced the barrier and thus improved the n-Si/Al back contact.

Improved rear surface passivation and rear contact has also been realised by an ultra-thin layer of lithium fluoride [68], traditional phosphorous diffusion [10], [100], a stack of amorphous silicon [a-Si:H(i/n)] [101] and siloxane [72], [95].

While PEDOT:PSS is a good hole transport layer, Mu *et al.* [52] found a thin interlayer of  $\text{WO}_3$  between PEDOT:PSS film and Ag front electrodes to further enhance device performance. Apart from this, no reports were found on the enhancement of the front contacts.

### 2.6.5 Suggested optimised process

Based on these advances, the following steps are suggested for an optimised solar cell:

Regarding absorption enhancement, anisotropic etching combined with isotropic etching for the bottom of the pyramids seems to have the combined advantage of improving the absorption of light without compromising the contact between PEDOT:PSS and Si, and simultaneously remaining a low-cost option.

The PEDOT:PSS dispersion should contain either 5% DMSO or 7% EG and somewhere between 1-2% Triton X-100. Additionally, post-deposition washing of methanol could enhance performance. However, care should be taken with respect to the amounts used. Excess methanol could remove too much PSS and result in detrimental passivation.

Besides utilising the native oxide, both an ultrathin siloxane layer and a bilayer of PEDOT:PSS films appears to elegantly provide low-cost, optimised interfaces. Either siloxane on both Si interfaces or a bilayer of PEDOT:PSS films on the front interface and siloxane on the rear interface should be very promising.

With siloxane on the rear Si interface, suggested back contacts include Ti/Ag, In/Ga, Ag and Al. The best contact needs to be determined experimentally. Alternatively, inserting  $\text{Cs}_2\text{CO}_3$  or N2200 between Si and Al also appears promising. Whether these can be used in addition to siloxane, however, will also need testing.

Due to limited time and resources, and a desire to gain a more fundamental understanding of the basic operation, most of these steps for an optimised solar cell were not conducted in this work. It should rather be seen as inspiration for further work which should be possible after the fundamental knowledge this thesis provides. However, as will be disclosed in more detail later, an optimised PEDOT:PSS blend containing 5% DMSO and 1% Triton X-100 was used.

# 3

## Methods and experimental

The following chapter deals with the specific methods used in this thesis for sample processing and characterisation. The experiments were conducted at The IFE Solar Cell Laboratory unless stated otherwise. Succeeding this, the experimental design and preliminary testing are described, including details regarding the different interfacial layers used.

### 3.1 Methods for sample processing

#### 3.1.1 Spin coating

Spin coating (SC) is a well-used, simple technique for applying thin films to substrates. It is a solution-based process which can be used to deposit materials such as polymers, inorganic films and crystalline chalcogenides. In a typical procedure, a solution containing the desired material is dispensed on a substrate surface which is then spun at high speed. The centrifugal force of the rotation makes the liquid spread uniformly and coat the surface. The rotation speed, together with the viscosity and surface tension of the solution, determines the thickness of the film. Depending on whether the solution is deposited before or after the substrate begins spinning, the process is termed static or dynamic, respectively. A variety of dynamic modes were used for the experimental work in this thesis due to reduced uniformity of the coverage across the relatively large substrates used when spin-coating with a static mode. A post-deposition baking is typically done to allow added solvents or resins to evaporate, and to stabilise and dry the film. Figure 3.1 shows the process as executed in this work.

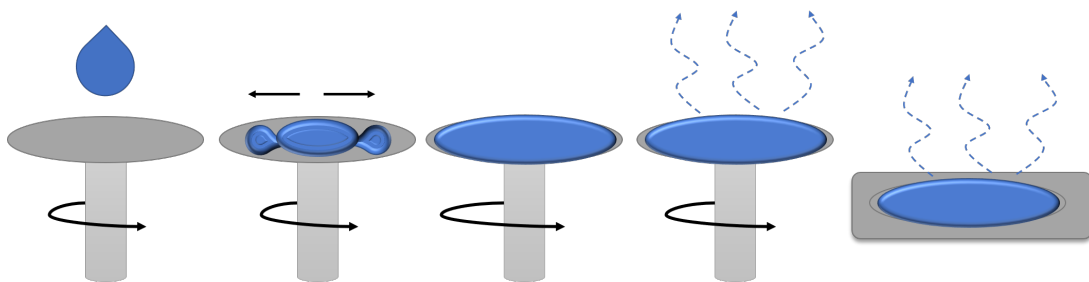


*Figure 3.1: The spin coating process. In the dynamic mode, the solution is deposited on a spinning substrate. The centrifugal force causes the solution to spread uniformly before the film is dried.*

In order to get a high quality and consistent film when using a dynamic spin coating mode, the substrate should reach the desired rotational speed before solution is dispensed and the solution should be deposited as close to the substrate centre as possible in one quick and smooth motion.

The wetting of the solution onto the substrate is an important parameter that affects the quality of the final film. Wetting is generally characterised by the contact angle of the liquid onto the surface, where a low contact angle (hydrophilic surface,  $< 90^\circ$ ) gives good wettability. In contrast, a high contact angle (hydrophobic surface,  $> 90^\circ$ ) yields poor wettability. As a result, both the viscosity of the solution and the hydrophilicity of the substrate is crucial to the film coating.

### 3.1.2 Contacting

Good contacts are required for extracting the charges generated in the solar cell without major resistive losses. Generally, Ohmic contacts are preferred to allow majority carriers to flow easily from the semiconductor into the metal. In order to obtain an ohmic contact on "p-type" PEDOT:PSS, the metal work function needs to be higher than the Fermi level of the p-type layer, causing accumulation of holes. Typical front contacts used in the literature include Ag, Au and a Ti/Pd/Ag stack.

For the back contact on n-type Si, an Ohmic contact is obtained by having a low work function compared to the Fermi level. However, metals tend to have work functions higher than the Fermi level of n-type Si, making this challenging. As a result, a transport barrier is unavoidable when forming a back contact on n-Si with Al or Ag directly on the n-Si surface [20], hindering effective extraction of electrons. Aluminium has the lowest work function of the metals available at IFE. Al acts as a p-type dopant in Si and could thus create a new junction at the backside if the device is subjected to a heat treatment. Furthermore, a large number of recombination centres exist at the un-passivated interface, causing photogenerated EHPs to be trapped and readily recombined [71]. An effective approach to avoid this transport barrier would be to insert a thin cathode interlayer functioning as a BSF, such as metal oxides or some organic materials, as described in section 2.6. Another possibility is to use a passivating layer and local contacts. Typical back contacts found in the literature include Ag, Al, Ti/Ag and In/Ga, often in conjunction with a BSF.

### 3.1.3 Thermal evaporation

Thermal evaporation is a physical vapour deposition method commonly used to deposit metals of relatively low melting points, such as Ag, Al and Au. During thermal evaporation, metal is melted in a crucible or boat made of Tungsten, through which a high current is run, causing the boat or crucible to heat up to the point where the metal within melts and starts to evaporate. The sample is placed above the heating element within a vacuum chamber which is held at high vacuum ( $\sim 10^{-7}$  Torr). The low pressure causes the metal to evaporate gradually, and the evaporated metal atoms to have a long mean

free path within the chamber. This results in the formation of a metal film on the full interior of the chamber, including on the sample surface [30]. The substrate holder can be slowly rotated to increase the homogeneity of the film and a quartz crystal microbalance is used to monitor the evaporation rate and deposited thickness.

## 3.2 Methods for characterisation

### 3.2.1 Current-voltage

Current-voltage (IV) measurements are central to solar cell characterisation. In this work, both light and dark IV measurements have been performed on diodes and grids to evaluate the solar cell performance. Moreover, a program to fit IV curves (IVFIT, version 2.12, ©A.R. Burgers), as described in [102], has been used to fit the obtained IV curves and extract relevant parameters.

#### Dark IV

Dark IV characteristics are excellent for examining diode properties without getting noise from small fluctuations in light intensity which typically appears when the diode is under illumination. We can get valuable information about the resistance, both due to contacting and internal factors, as well as evaluating the ideality of the diode. In order to easily compare different IV-curves, it is common to use current density,  $J_{sc}$ . All the relevant equations, including the ideal diode equation (2.1) and the two-diode model (2.7) were described in section 2.1.1.

#### IV curves for information about Series and Shunt Resistance

The slope of the IV curve as it crosses zero voltage indicates the shunt resistance. Qualitatively, if the IV curve is flat near  $J_{sc}$  the device does not have significant shunting. The extent to which series resistance affects the device performance can be determined by comparison of the illuminated IV curve and the dark IV curve shifted by  $J_{sc}$  or to its illuminated open circuit voltage curve. When illuminated, the photogenerated current flows out of the solar cell, incurring a voltage drop equivalent to the current times the resistance. When measured without illumination, the current flows into the cell, causing the measured voltage to be higher than the cell's internal voltage.

### 3.2.2 Sheet resistance

The resistivity or conductivity of a material represents the material's ability to conduct electric currents in three dimensions. The sheet resistance, being the resistivity averaged over the film thickness [20], is hence a measure of the lateral conduction. When it comes to evaluating the performance of PEDOT:PSS/Si solar cells in terms of resistance, the

two-dimensional sheet resistance is the most suitable quantity since the lateral carrier conduction is of primary importance in such devices [90], [95].

### Transfer length method

In order to determine the sheet resistance of a layer, it is common to apply the four-point probe or van der Pauw. Here, four contacts are employed to determine the sheet resistance of a layer without getting major effects from contact resistance. In solar cells and other electronic devices, the contacts are an important part of the device, and it is thus useful to know both the sheet resistance and contact resistance for our solar cells. Additionally, it is difficult to extract a value for the sheet resistance without influence from the contacts.

In transfer length method (TLM) measurements, resistors of several different lengths are constructed while keeping all other parameters constant. By measuring the total resistance between these contacts and plotting it against the contact spacing  $d$ , the contact resistance can be extrapolated from the graph. Furthermore, the sheet resistance of the semiconductor is given by the slope. Figure 3.2 shows the test structure and how the data should be plotted to extract sheet resistance  $R_{sh}$ , contact resistance  $R_c$  and transfer length  $L_T$ . Further, the specific contact resistivity  $\rho_c$  can be determined from

$$\rho_c = L_T^2 R_{sh} \quad (3.1)$$

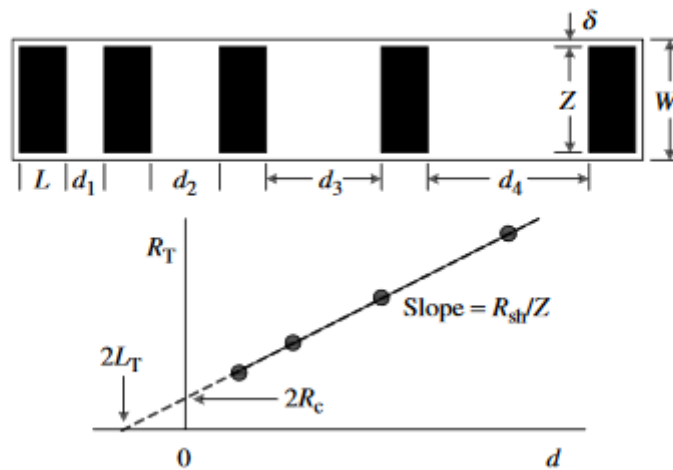


Figure 3.2: TLM test structure and a plot of total resistance as a function of contact spacing  $d$  with the possible extracted parameters. From [20].

### 3.2.3 Capacitance-voltage

Capacitance-voltage (CV) is also a great tool where information about doping concentration and built-in voltage can be deduced from a simple scan. Due to the  $p^+-n$  approxi-

mation, the junction capacitance and the depletion region can be expressed as

$$C = \frac{\varepsilon_{Si} A}{W} \quad (3.2)$$

$$W = \sqrt{\frac{2\varepsilon_{Si}(V_{bi} - V)}{qN_d}} \quad (3.3)$$

where  $\varepsilon_{Si}$  is the dielectric constant of Si,  $W$  is the width of the SCR,  $V_{bi}$  is the built-in voltage,  $V$  is the applied bias,  $N_d$  is the donor concentration and  $A$  is the area of the diode.

From equations 3.2 and 3.3 we can get a relationship between the capacitance and the voltage

$$\frac{1}{C^2} = \frac{2(V_{bi} - V)}{\varepsilon_{r,Si}\varepsilon_0 q A^2 N_d} \quad (3.4)$$

A linear regression of said plot yields  $V_{bi}$  at the x-axis interception and the possibility of finding the doping concentration,  $N_d$  from the slope:

$$N_d = -\frac{2}{\varepsilon_{r,Si}\varepsilon_0 q a A^2} \quad (3.5)$$

where  $a$  is the slope. A typical CV and corresponding  $1/C^2$  curve with extrapolated values for  $V_{bi}$  is shown in figure 3.3

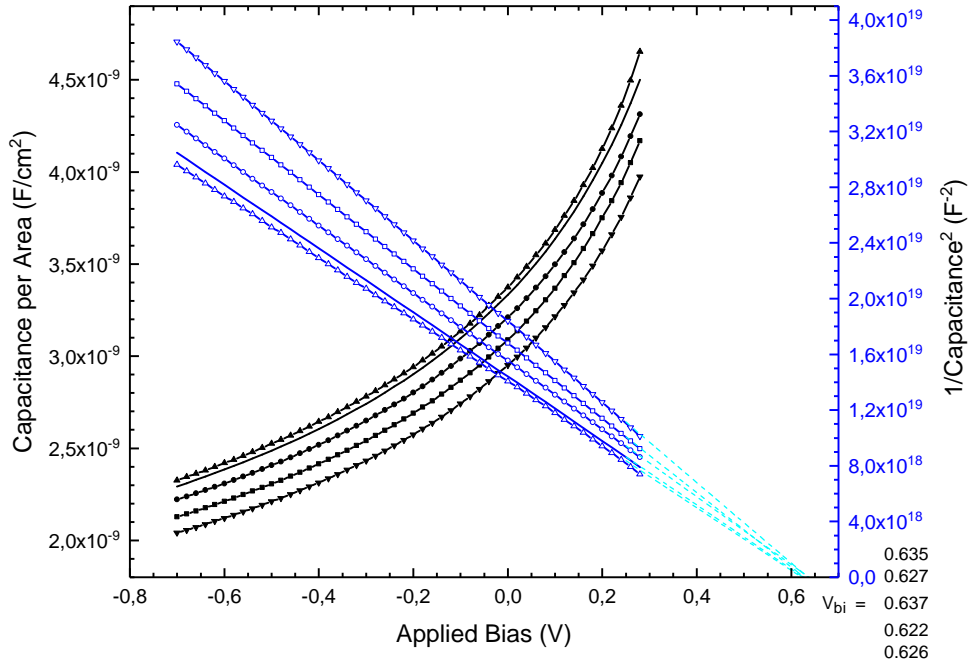


Figure 3.3: Capacitance per Area and  $1/C^2$  versus voltage measured on a PEDOT:PSS/n-Si structure at frequencies of 100 kHz and 1 MHz. The x-axis intercept for  $1/C^2$  gives the built-in voltage.

In a p-n junction,  $V_{bi}$  is defined as the potential difference across the junction. By using this definition for a hybrid system, molecular details and interfacial states are neglected. Nevertheless, it can be used as an approximation to the upper limit of the device  $V_{oc}$  [103], [104]. Note that  $V_{oc}$  never reaches  $V_{bi}$  in real cells due to recombination.

### 3.2.4 Quasi-steady state photoconductance

By measuring the conductivity of a sample under illumination, quasi-steady state photoconductance (QSSPC) is used to determine the excess carrier density in a sample. The use of a flash ensures that the excitation intensity varies over time, enabling the lifetime to be measured as a function of injection level, all in a single measurement [30]. The method was first proposed by Sinton *et al.* [105], and has since been widely adopted.

The time evolution of the minority carrier density, and our starting point to evaluate the carrier density is given by

$$\frac{d\Delta n(t)}{dt} = G(t) - U(t) + \frac{1}{q}\nabla J \quad (3.6)$$

where  $G(t)$  and  $U(t)$  are the generation and recombination rates. Due to the use of a long pass filter, the gradient in the current density  $\nabla J$  can to a good approximation be set to zero. Additionally, the steady state condition dictates that  $\frac{d\Delta n(t)}{dt} = 0$ , further simplifying our expression. By using equation 2.12 with the effective lifetime  $U = \frac{\Delta n}{\tau_{eff}}$ , the effective lifetime can be expressed as

$$\tau_{eff} = \frac{\Delta n(t)}{G(t)} \quad (3.7)$$

Thus, by measuring both the injection level and the generation rate as a function of time,  $\tau_{eff}$  may be determined. The generation rate can be measured from a small reference solar cell placed on the sample stage, and the injection level is concurrently determined from the measured excess conductivity,  $\Delta\sigma$ , as

$$\Delta n(t) = \frac{\Delta\sigma(t)}{q(\mu_n + \mu_p)W} \quad (3.8)$$

Here,  $\mu_n$  ( $\mu_p$ ) is the electron (hole) mobility and  $W$  is the wafer thickness. Now, the effective lifetime can be calculated at each injection level using equation 3.7.

### 3.2.5 Photoluminescence imaging

Photoluminescence imaging (PLI) is a valuable method for the characterisation of silicon samples and is being used across most parts of the silicon PV value chain. It is contactless, non-destructive and provides an efficient way of measuring the quality of silicon wafers with high spatial resolution [106]. Schematics of the PL setup with integrated QSSPC coil is shown in figure 3.4.

Photoluminescence is the process where excess carriers generated from the absorption of photons recombine and release the energy as photons. These photons can then be detected by a camera, and this information can be used to find the lifetime in the material and relative variations over the wafer [107].

For low-injection and moderately doped n-type material, the injection level  $\Delta n$  is proportional to the measured intensity  $I_{PL}$ :

$$\Delta n(x, y) = \left( \frac{1}{C_{cal} B_{rad} N_D} \right) \times I_{PL}(x, y), \quad (3.9)$$

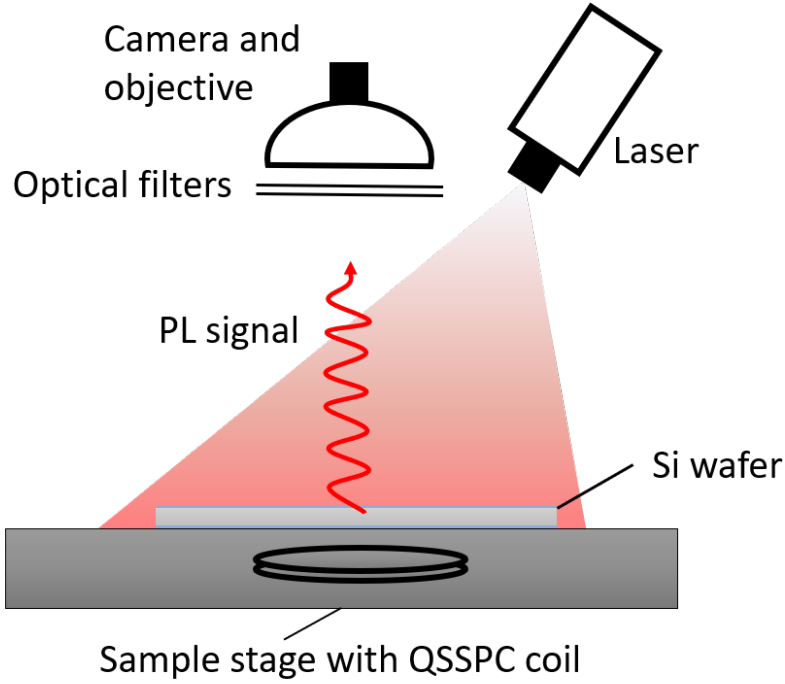


Figure 3.4: Illustration of the PLI equipment. Adapted from [30].

where  $C_{cal}$  is an instrument- and sample specific constant that describes the fraction of emitted light detected by the camera. The PL image is measured at steady state conditions. The effective lifetime can hence be obtained from the injection level and the generation rate  $G$  as

$$\tau_{eff}(x, y) = \frac{\Delta n(x, y)}{G} = \frac{\Delta n(x, y)W}{(1 - R_f)\Phi_{ph}} \quad (3.10)$$

$R_f$  is the front reflectance and  $\Phi_{ph}$  is the photon flux from the excitation source.

Without any means of determining  $C_{cal}$  the resulting PL images are in arbitrary units; still useful for investigation of relative variations over the wafer, but lacking an absolute measure of the lifetime in the material. By combining the PLI setup with a QSSPC setup, however, the lifetime at each point in the image can be calculated correspondingly to the actual lifetime values measured simultaneously by QSSPC. Correct quantification requires knowledge of the thickness of the sample, the front side reflectance at the excitation wavelength and the doping concentration of the sample.

Implied  $V_{oc}$  can be found from PL measurements in the energetic distance between the electron and hole quasi-Fermi levels, described by the following equation

$$V_{oc, implied} = \frac{kT}{q} \ln \left( \frac{\Delta n(\Delta n + N_D)}{n_i^2} \right) \quad (3.11)$$

This will give a measure of the theoretical maximum value for  $V_{oc}$  provided an identical passivation for the backside as the one provided from PEDOT on the front.

### 3.3 Experimental design

This section intends to give an overview of the general procedure and instrumentation used in this thesis.

#### 3.3.1 Materials

##### Chemicals

All chemicals were used without any further purification and stored as advised by the manufacturer. Table 3.1 shows the chemicals used in the PEDOT:PSS solution. Triton X-100 is henceforth referred to as Triton.

*Table 3.1: The chemicals used in the PEDOT:PSS solution.*

Chemical	Supplier	CAS	Lot #
PEDOT:PSS PH 1000	Ossila	1555090-83-8	N/A
Dimethyl sulfoxide	Sigma-Aldrich	67-68-5	STBG9203
Triton X-100	Alfa Aesar	9002-93-1	10217161

##### Wafers

The different silicon wafers used are listed in table 3.2.

*Table 3.2: Silicon wafers used.*

Name	Identification	Thickness	Resistivity
Siegert CZ p-type	L14233	$275 \pm 20 \mu\text{m}$	1 – 5 $\Omega\text{cm}$
Topsil FZ n-type	B35-1100-0280-001	$280 \pm 20 \mu\text{m}$	1 – 5 $\Omega\text{cm}$
Topsil FZ p-type	B85-1100-0280-001	$255 \sim 305 \mu\text{m}$	1 – 5 $\Omega\text{cm}$

The CZ p-type wafers were used for preliminary testing of spin speeds and training on the equipment and are not used for any of the results presented in this thesis. The FZ p-type wafers were used to affirm the p-type behaviour of PEDOT:PSS and explore differences in passivation for PEDOT:PSS on p-type and n-type Si, respectively. For the vast majority of this work, the n-type Topsil FZ wafers were used. All wafers were cut in four and either directly used for spin coating or exposed to different surface treatments as explained in section 3.4.3. The wafers that were measured with CV displayed resistivities in the range 1.9–3.2  $\Omega\text{cm}$  with an average value of 2.6  $\Omega\text{cm}$  from 10 wafers.

### 3.3.2 Sample preparation

A great deal of this work has been various characterisation of simplified solar cell structures, namely silicon with a native oxide layer and PEDOT:PSS deposited on one side.

PEDOT:PSS was filtered through a 0.45  $\mu\text{m}$  polyvinylidene fluoride (PVDF) membrane filter (Millex<sup>®</sup>). Then, 5 % DMSO and varying amounts of Triton, ranging from 0.1 % to 5 %, were added to the solution and subsequently stirred for a minimum of two hours. The mixed solution was stored in a fridge and always used within two weeks.

An aliquot (300  $\mu\text{L}$ ) of the PEDOT:PSS solution was spin-coated onto the Si substrate. Spin coating was primarily carried out at two different settings, one termed "fast" consisting of 30 seconds at 2000 rpm, followed by 50 s at 6000 rpm, and the other termed "slow" with 10 s at 1000 rpm followed by 30 s at 1500 rpm. All spin coating was carried out with a dynamic mode. After spin coating, the wafer was annealed at 120°C for 15 minutes.

Samples for lifetime measurements were spin-coated on both sides to obtain symmetrically passivated samples, with the second annealing only lasting 2 minutes to avoid any thermal degradation of the PEDOT:PSS. Samples for electrical characterisation were metallised on the front through a shadow mask and on the entire rear by thermal evaporation. Figure 3.5 shows the general process flow. Details regarding the different wafer treatments will be disclosed in section 3.4.3.

The process builds on previous work done at IFE. The original process established at IFE consisted of filtration, 5 % DMSO and 0.1 % Triton, minimum 2 h storage, fast spin coating and post-deposition annealing at 120°C for 15 minutes. This is also in good agreement with literature. The additions from this work in terms of sample preparation is thus a slower spin speed and the admixture of more Triton.

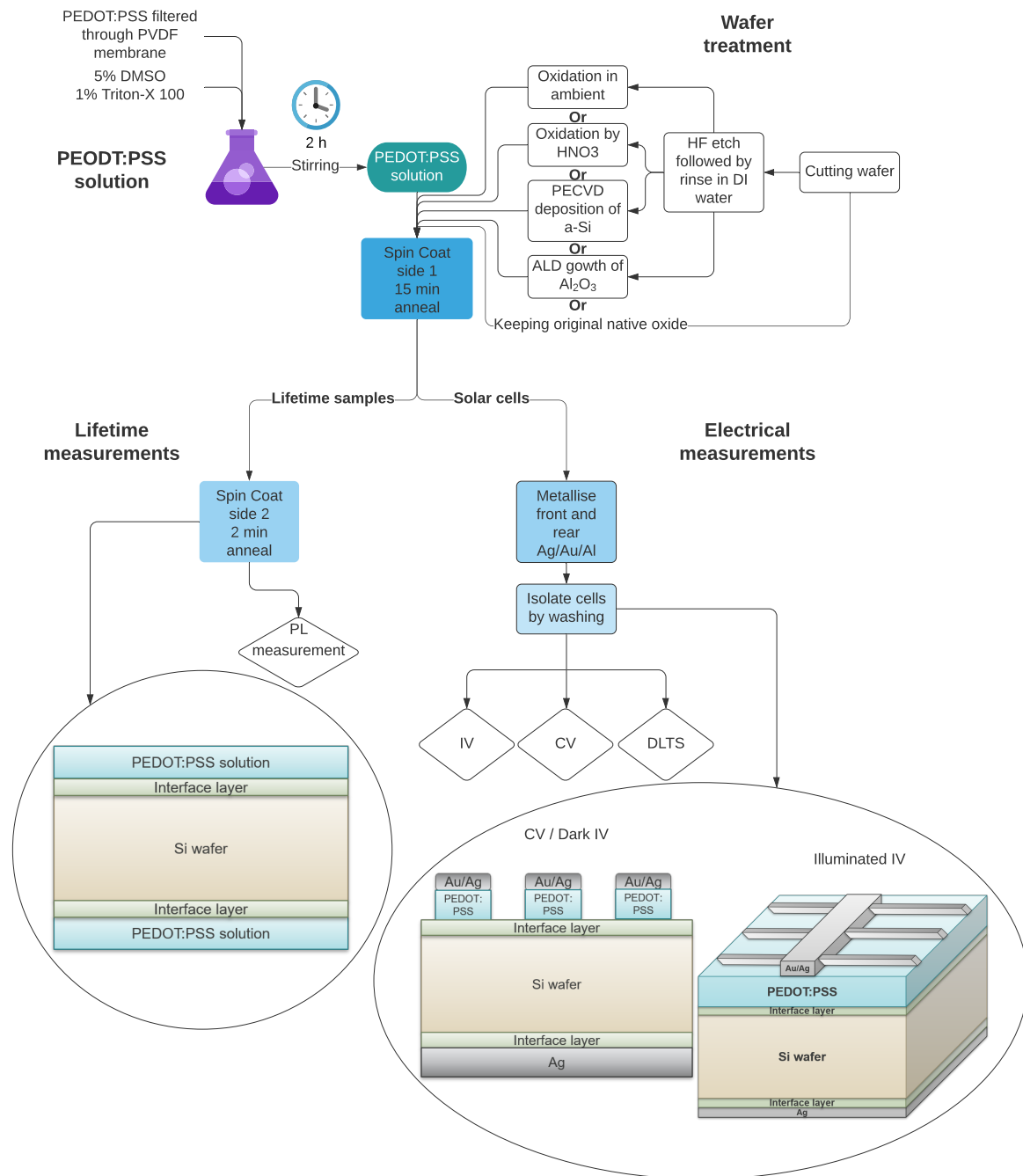


Figure 3.5: The process flow.

## 3.4 Preliminary testing

The following section covers the initial testing performed to obtain a reproducible, optimised process.

### 3.4.1 PEDOT:PSS sample preparation

#### Spin speed

Experiments were both conducted with fast spin coating (2000 rpm followed by 6000 rpm) consistent with previous work conducted at IFE and slow spin coating (1000 rpm followed by 1500 rpm) closer to what is reported by Schmidt *et al.* [10]. The slow spin resulted in a thicker film and slightly better lifetime, albeit at the expense of ease of wafer coverage. It became evident that the spin coating process, especially the spin speed and amount of surfactant, should be optimised for different surface treatments. Additionally, the lack of an automated process for the deposition of the PEDOT:PSS solution led to various results depending on the height of the pipette tip above the spinning substrate. These variations were naturally reduced as the process adhered to muscle memory.

Static spin and dynamic spin below 1000 rpm were also attempted. Both resulted in abysmal coverage of the wafer and were thus not used further.

Due to the slightly better lifetime, the slow spin speed was used for the majority of the results presented in this thesis.

#### Composition

Based on recommendations from the producer of the PEDOT:PSS blend, previous work conducted at IFE and literature, PEDOT:PSS was mixed with 5% DMSO to enhance the conductivity. Varying amounts of Triton-X100, ranging from 0.1% to 5% were also mixed in to act as a surfactant. The addition of 1% Triton-X seemed to yield the best trade-off between coverage on wafer and lifetime and was thus chosen for future experiments. Comparison of the relative lifetime and coverage for the different concentrations of Triton is shown in figure 3.6.

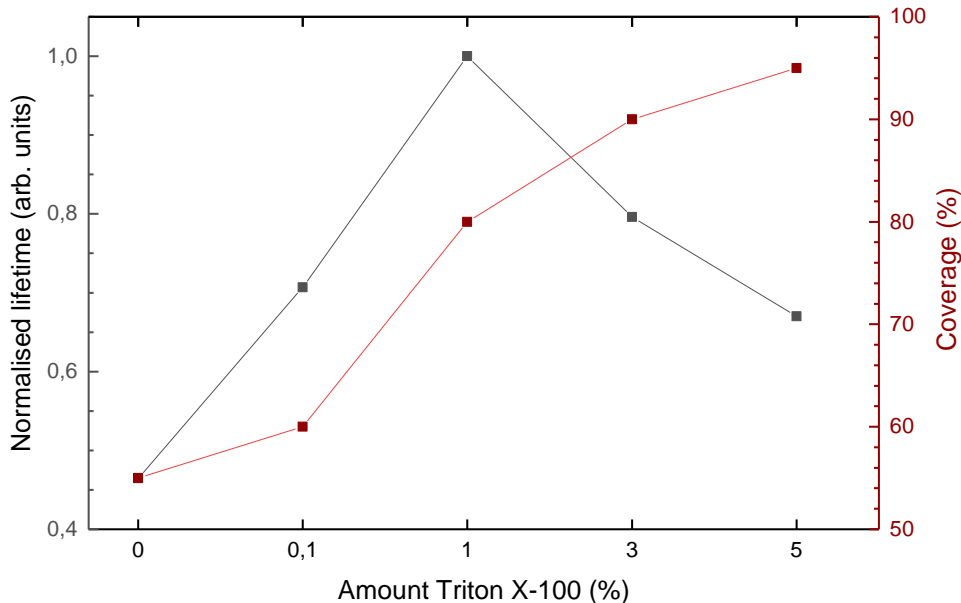


Figure 3.6: Measured normalised lifetime and approximate coverage on samples with varying amounts of Triton in the PEDOT:PSS solution. The best lifetime is obtained for 1% Triton while the coverage kept improving with more Triton. This is expected since it is a surfactant and should thus enhance the wetting on the substrate.

### 3.4.2 Fabrication of samples for electrical characterisation and solar cells

#### Isolation

The first wafers for electrical characterisation were metallised with diodes of various size, as shown in the inset in the upper left graph of figure 3.7. This was to validate the diode behaviour and get an idea of the homogeneity of the PEDOT:PSS.

A mapping of the diodes showed similar characteristics over the entire wafer. However, the lateral transport of electrical charge in PEDOT:PSS, combined with influence from neighbouring contacts, resulted in IV curves with severe shunt and series resistance. To alleviate this, separate contacts were isolated by removal of PEDOT:PSS around the contacts; this was simply done by washing with distilled water and cotton buds. Resulting IV curves from before and after isolation are seen in figure 3.7.

The IV curves before isolation were affected by low shunt resistance, as seen in the slope in reverse bias. Moreover, a high series resistance is evidenced by the slope in forward bias. After isolation, the loss through shunt resistance is eliminated since the curve is flat in reversed bias. In addition, there seems to be less series resistance due to the much more well-defined kink around 0.5 V and the steeper slope in forward bias.

This is also evidenced by the semi-logarithmic plots of the current. Isolation leads to a much more well-defined curve, negligible shunt resistance and a considerably lower saturation current density.

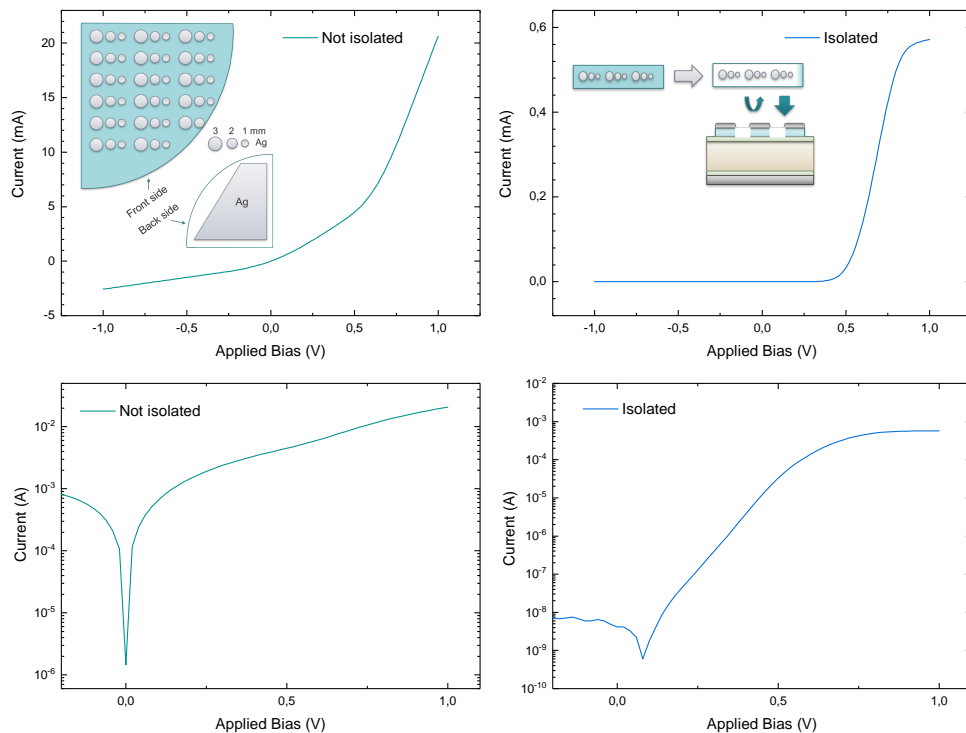


Figure 3.7: IV curves from diodes before and after isolation. Before isolation (left) severe losses through both shunt and series resistance were present, as evidenced by the slopes in both forward and reversed bias. After isolation (right), however, the shunt resistance is greatly enhanced and the series resistance is reduced.

### Choice of metal

The available metals at IFE for evaporation were Ag, Al and Au. Initial tests were conducted with both Ag and Al as front and back contacts. In theory, Al, with the lowest work function, is the best option as the back contact, with Ag as a second best. Comparison of diode performance in dark IV with different combinations of metal contacts is shown in figure 3.8. A representative set of measurements lie within the shaded areas. In general, it proved difficult to compare different metals based purely on dark IV performance of diodes. However, some conclusions could be drawn by considering the following criteria:

The obtained IV curves for each set of contacts should have little variation. Moreover, the kink should appear at high forward bias, indicating a lower  $J_0$  and the potential for a higher  $V_{oc}$  in the real solar cell. So far, these criteria rules out the Ag/Ag contact (orange) and the Ag/Al contact with PEDOT:PSS spun at a high spin speed (purple). Lastly, the slope in high forward bias should be relatively steep, indicating a sufficiently low  $R_s$ .

Based on these criteria, the best contacts were found to be Au/Ag stack as front contact and Ag as back contact. This is evidenced by the kink appearing at relatively high forward bias, a fairly good "squareness" of the IV curve and low variation in separate measurements. In addition, the semi-logarithmic IV curve displays well-defined regions and by far the lowest  $J_0$  (as seen by the slope around 0.2–0.5 V).

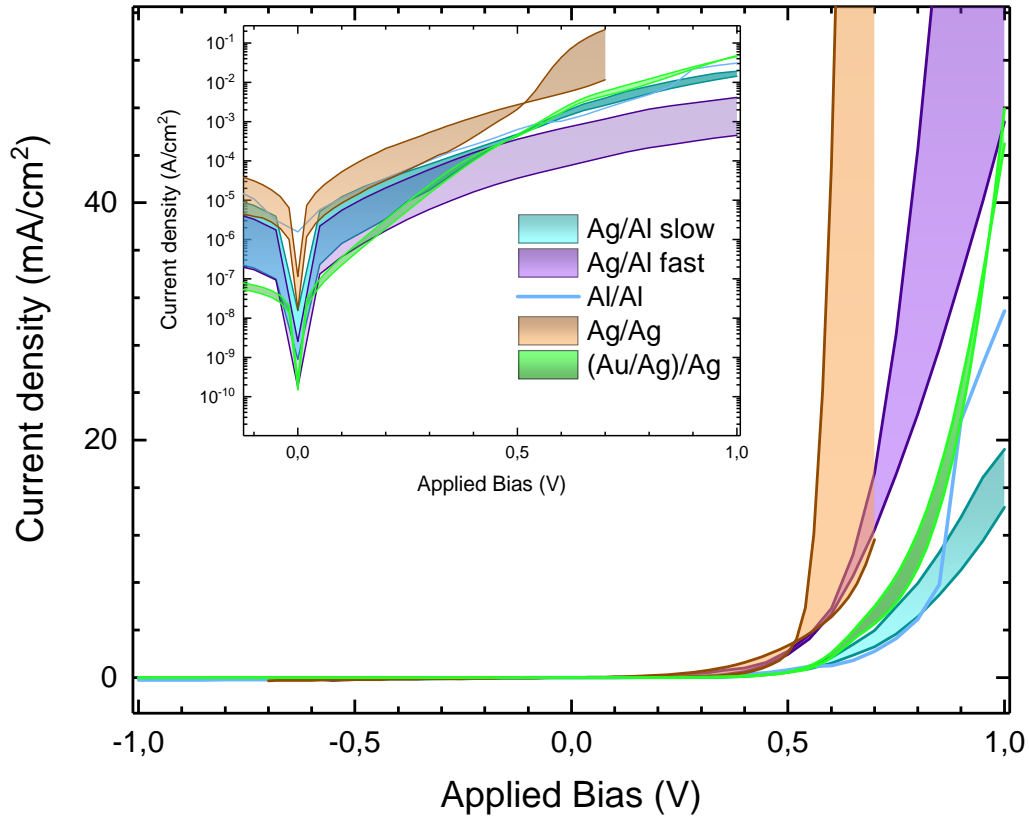


Figure 3.8: Comparison of different metals used for contacting. By considering the variation between measurements on the same wafer,  $J_0$  and series resistance, the (Au/Ag)/Ag contacts were found to be optimal.

### Solar cell

With the process optimised, solar cells for electrical characterisation were made as shown schematically in figure 3.9. Each wafer was fabricated with four grids of  $1 \times 1 \text{ cm}^2$  (28% shading) which were used for full IV measurements. In addition, diodes with a diameter of 1 and 2 mm were used for CV and DLTS measurements, and a TLM test structure used to measure sheet resistance. Since all the different components were isolated after contacting, each fabricated wafer consisted of four separate solar cells which could be measured without influence from the others.

10 nm Au and 250 nm Ag was evaporated through the shadow mask to make up the front contacts, while 250 nm Ag was evaporated on almost the entire rear (the edges were masked to avoid any metal on the sides which could lead to shunting). The shadow masks were cut from dummy wafers.

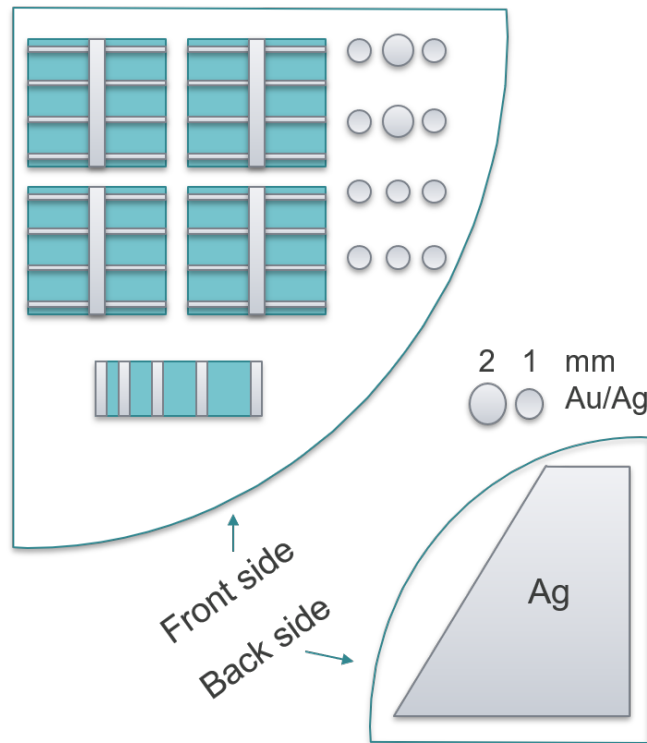


Figure 3.9: Structure of the simple solar cell devices, consisting of four grids ( $1 \times 1 \text{ cm}^2$ ), diodes with a diameter of 1 and 2 mm and a TLM test structure, all isolated after contacting.

### 3.4.3 Experiments on different interfacial layers

After optimising the PEDOT:PSS solution and approaching solar cell structures, the crucial role of the interface quickly became evident. The interface had a significant impact on the IV performance, but also the passivation, as will be thoroughly discussed in Chapter 4. Furthermore, the optimised PEDOT:PSS solution and device fabrication enabled the deposition of PEDOT:PSS on HF-treated samples and thereby enabled superior interface control than previous work at IFE.

Optimising the interface layer between PEDOT:PSS and Si is thus essential, both to find the optimal interface and possibly a trade-off between cost and performance. Following is a summary of the different interfaces used in this work.

#### Native oxide

The ultimate low-cost option for the PEDOT:PSS/Si interface is to merely use untreated Si wafers. The original native oxide that comes from the producer is expected to have a thickness between 1 and 2 nm. Wafers with the native oxide were simply cut into quarters and flushed with nitrogen ( $\text{N}_2$ ) before spin coating and metal evaporation.

#### New growth of native oxide

To grow a new native oxide, quarter wafers were dipped in 5% HF for 30 seconds, rinsed in DI water for 2 minutes and dried with  $\text{N}_2$  before left in ambient conditions for varying

amounts of time. Previous work at IFE had experienced difficulties with coating the Si surface after HF etch. This was, however, not an issue in this work, possibly due to the use of more Triton and slower spin speeds.

### **Chemically grown SiO<sub>2</sub>**

The oxidation of samples with HNO<sub>3</sub> was done both in room temperature and at 121°C according to the work by Kobayashi *et al.* as described in section 2.1.3. Quarter wafers were given the same pre-treatment as the native oxide growth before immersing in the nitric acid. First, two wafers were oxidised in 65 wt% HNO<sub>3</sub> at room temperature for 10 min and subsequently rinsed in water and dried. Then, the acid was heated up to 121°C and left to boil for 15 min to evaporate water and reach the azeotrope composition of 68 wt% HNO<sub>3</sub>. Finally, two new wafers were immersed in the boiling solution and oxidised for 10 min before rinsing and drying.

### **Al<sub>2</sub>O<sub>3</sub> deposited by ALD**

By courtesy of Eirik Koch Jubskås, Al<sub>2</sub>O<sub>3</sub> was deposited on H-terminated Si by Atomic Layer Deposition (ALD) at the Microsystems and Nanotechnology (MiNa) lab at the University of Oslo. This technique grows monolayers of the desired compound by sending different precursors into a chamber and therefore provides quite good thickness control by adjusting the number of cycles. A variety of different cycles were used, resulting in thicknesses in the range of 1.3–2.7 nm, measured by ellipsometry after deposition.

### **Amorphous silicon**

a-Si:H was deposited on H-terminated Si by courtesy of Halvard Haug by Plasma-Enhanced Chemical Vapour Deposition (PECVD). The use of plasma enables deposition at considerably lower substrate temperatures than that of standard Chemical Vapour Deposition. Two different thicknesses of a-Si:H were deposited by varying the time between ramping the effect up to the process setpoint and ramping down; one ramping down immediately and the other ramping down after a 15 s delay. The exact thicknesses were not known but expected to be a few nanometers.

# 4

## Results and Discussion

In this chapter, the experimentally obtained results will be presented and discussed. First, the passivation of PEDOT:PSS is presented. This is followed by a comprehensive study of the stability of the passivation with wafers subjected to different storage conditions. Subsequently, initial electrical characterisation is presented together with steps for an optimised process. Thereafter, the effect of different interface layers is studied, both with respect to initial performance and long-term stability. Ultimately, the best process is briefly reviewed and further improvements are discussed based on the results obtained in this work and literature.

### 4.1 Passivation by PEDOT:PSS

Our PEDOT:PSS provides excellent surface passivation on n-type silicon (FZ,  $\rho = 1 - 5 \Omega\text{cm}$ ), as can be seen in figure 4.1. Evidently, the spin coating provides good, homogeneous coverage of PEDOT:PSS over the wafer, as seen by the even lifetime distribution in the PL mapping across almost the entire substrate. Furthermore, an effective lifetime of  $300 \mu\text{s}$  points to quite an excellent passivation, at least initially. Assuming a bulk lifetime corresponding to an intrinsic lifetime of  $2.7 \times 10^{-2} \text{s}$  and a doping concentration of  $1.87 \times 10^{15} \text{cm}^{-3}$  ( $2.5 \Omega\text{cm}$ ), this corresponds to an SRV of  $46 \text{cm/s}$ . Herein, the intrinsic lifetime is determined according to the parametrisation by Richter *et al.* [108] at an injection level of  $1.5 \times 10^{15} \text{cm}^{-3}$  and the mentioned doping concentration. By assuming an infinite bulk lifetime, the SRV increases to  $47 \text{cm/s}$ .

This result is from the PEDOT:PSS solution spun directly on an untreated Si wafer. While the passivation was improved further by adapting optimised surface treatments to the wafer, this shows how easily PEDOT:PSS can be utilised to supply a surface passivation which effectively reduces any power loss arising from front surface recombination, at least for the present structure. This will be further discussed in section 4.5.1.

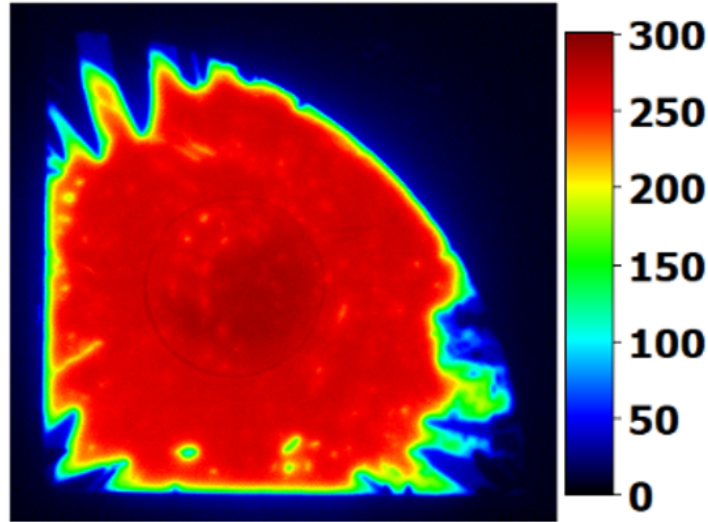


Figure 4.1: Photoluminescence image of a quarter 4-inch n-type FZ Si wafer with  $\rho = 1 - 5 \Omega\text{cm}$  and the original native oxide. Mapping of the effective carrier lifetime measured in  $\mu\text{s}$ . The wafer is showing a good coverage with lifetime around  $300 \mu\text{s}$ , corresponding to an SRV of  $46 \text{ cm/s}$ . This is considered as sufficient surface passivation for high efficiency solar cells.

In conclusion, PEDOT:PSS provides good surface passivation on Si with excellent homogeneity from very uncomplicated, low-cost fabrication methods.

## 4.2 Stability

Several research groups have recently shown record-high efficiencies of PEDOT:PSS/Si hybrid solar cells, with ISFH at the helm reporting an efficiency of 20.6% with their BackPEDOT concept [12]. This shows that, at least in terms of efficiencies, these hybrid solar cells can be a viable low-cost alternative to silicon solar cells. One inherent elephant in the room, however, is the stability of these cells. Schmidt *et al.* have touched upon the issue [10], but otherwise, reports have been scarce. Organic material tends to degrade when exposed to humidity and light, and especially the ability to be exposed to light is crucial for an operational solar cell. Figure 4.2 shows the evolution in carrier lifetime for a sample similar to the one shown in figure 4.1 stored in the dark under ambient conditions between measurements. The initially high lifetime is clearly not stable; after only ten days, the lifetime has decreased by roughly 20%, and after more than 30 days the lifetime seems to approach half of the initial value. In this section, we will take a systematic approach to determine the stability of these wafers as well as understand the factors influencing the stability.

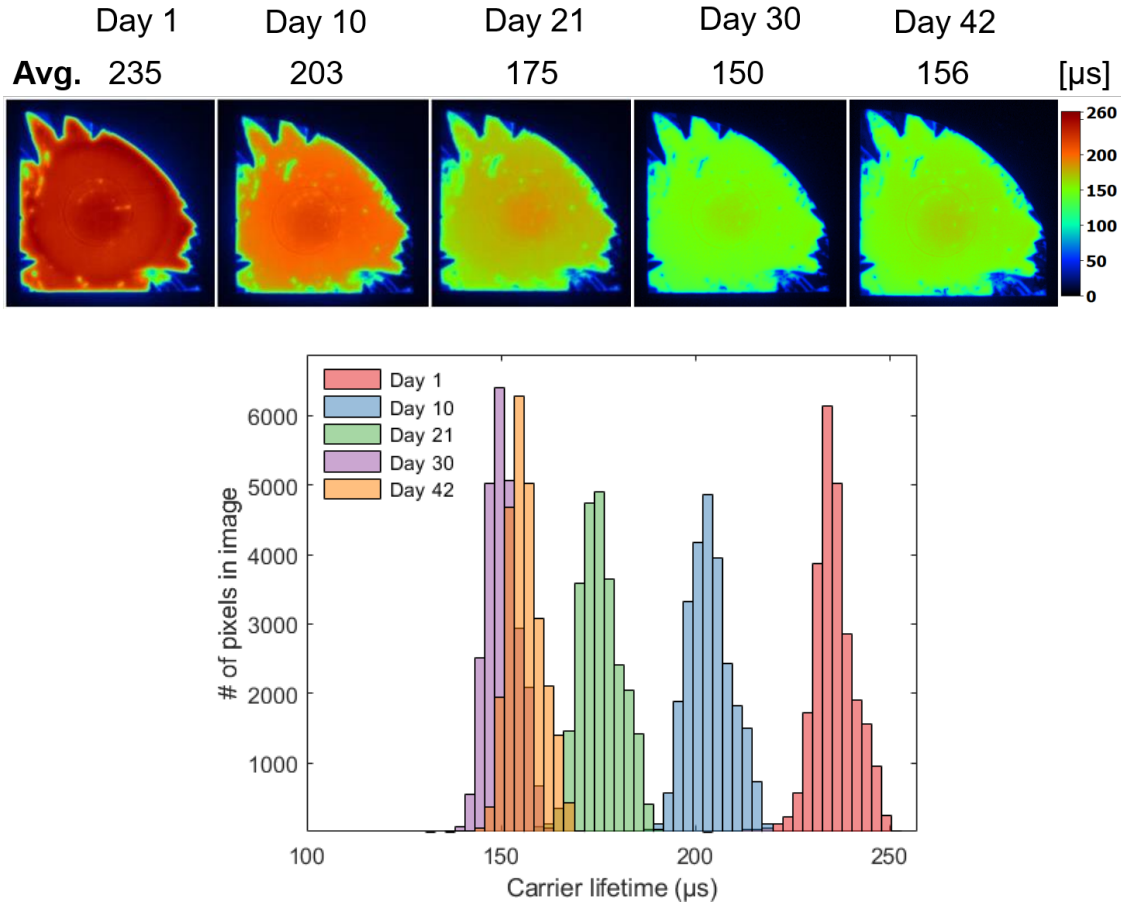


Figure 4.2: PL image of the same n-type Si wafer passivated with PEDOT:PSS taken over a span of 42 days (top) and histograms of the same wafers taken from a  $\sim 4\text{ cm}^2$  square on the middle of each wafer (bottom). There is an even decrease in the carrier lifetime over the entire wafer.

### 4.2.1 Degradation

Since the lifetime of the minority carriers is the main measure of the quality of the passivation, it is also a natural starting point to measure degradation over time. In figure 4.3, the carrier lifetime measured at an injection level of  $1 \times 10^{15} \text{ cm}^{-3}$  by QSSPC for the same sample as in figure 4.2, as well as a similarly produced p-type wafer, is displayed. The wafers were measured at regular intervals for more than a year and clearly shows considerable degradation. An initially high lifetime of  $300 \mu\text{s}$  decreases to half of its initial value after 50 days and continues to decrease until it reaches a little below  $1/3$  of the initial value somewhere between 100 and 150 days. After this, however, the lifetime seems to stabilise. It is worth noting that this is still considerable passivation. For comparison, an unpassivated Si wafer would be expected to have a carrier lifetime of  $\sim 1\text{--}2 \mu\text{s}$ .

A similar trend is observed for the p-type wafer, only shifted to lower lifetimes. This can be explained by the passivation mechanism by PSS as discussed in section 2.5.1; the junction formed between PEDOT:PSS and p-type Si will not promote transport of holes to the interface as opposed to the junction between PEDOT:PSS and n-type Si. Thus, the PSS will not be able to form as many bonds with Si, and the passivation will be poorer.

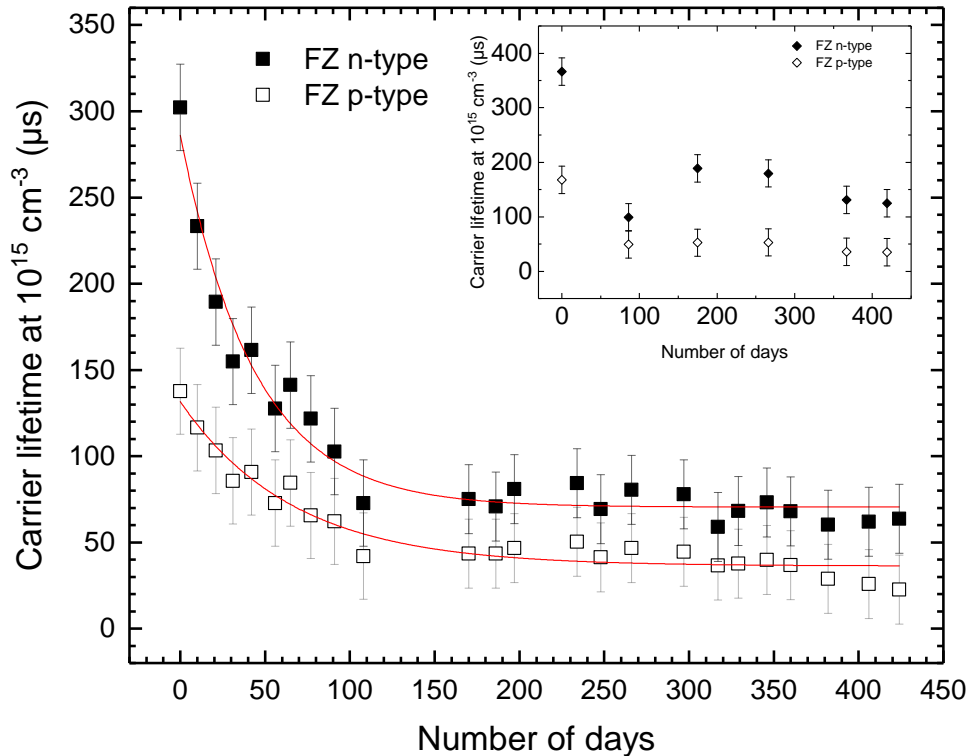


Figure 4.3: Measured carrier lifetime at an injection level of  $1 \times 10^{15} \text{ cm}^{-3}$  for FZ n- and p-type Si wafers passivated with PEDOT:PSS on both sides. A clear decrease in carrier lifetime is observed, with the lifetime reaching half of its initial value after around 50 days and seemingly approaching a steady value of around 30% of initial value after  $\sim 150$  days of storage. The lines are exponential fits to the measured decay. The inset shows similar samples with longer intervals between measurements and display similar degradation.

These wafers have been stored in plastic containers inside a dark cupboard when not being measured. It is thus safe to assume that the wafers have been exposed to ambient conditions, such as a relative humidity around 20% and approximately  $25^\circ \text{C}$ , but not any excessive light.

In order to check whether the act of measuring the wafer had a significant impact on the lifetime, and at the same time replicate the experiment, similar wafers were produced and stored in the exact same way, but with longer intervals between each measurement.

A similar degradation is visible in the inset in figure 4.3. A high initial carrier lifetime of  $365 \mu\text{s}$  and  $168 \mu\text{s}$  for n- and p-type, respectively, drops down significantly after 86 days of storage. The carrier lifetime seems to stabilise at  $180\text{-}190 \mu\text{s}$  for n-type Si and  $50 \mu\text{s}$  for p-type Si between 200 and 270 days. However, a further drop towards  $130$  and  $30 \mu\text{s}$ , respectively, occurs after one year in storage.

The outlier at day 86 for the n-type Si may be due to the placement of the wafer on the QSSPC-coil in the PL setup or some other measurement error. It seems unlikely that the carrier lifetime would drop and later increase again without any external influence.

Another reason for this outlier could be the weather. Interestingly, all the samples appear to have an outlier around the 100th measuring day. These were all measured on

a hot day right before the summer holidays. It is possible that the outdoor temperature influenced the measurements and is thus responsible for the lower measured value.

### A note on measurement errors

The exact position of the QSSPC coil relative to the wafer will naturally vary a little between each measurement. In addition, the temperature and humidity in the room show some variation with the season and the activity with, for instance, lamps for light soaking. A joint effort of these variations is suspected as the culprit for the measurement points deviating from the trends.

In order to get a reasonable estimate for the errors originating from varying placements of the sample when doing measurements, two wafers were fabricated and measured several times on the same day. The samples were removed and placed anew between each measurement, mimicking the effect when measuring degradation in samples. Figure 4.4 shows the measured carrier lifetimes and the resulting confidence intervals.

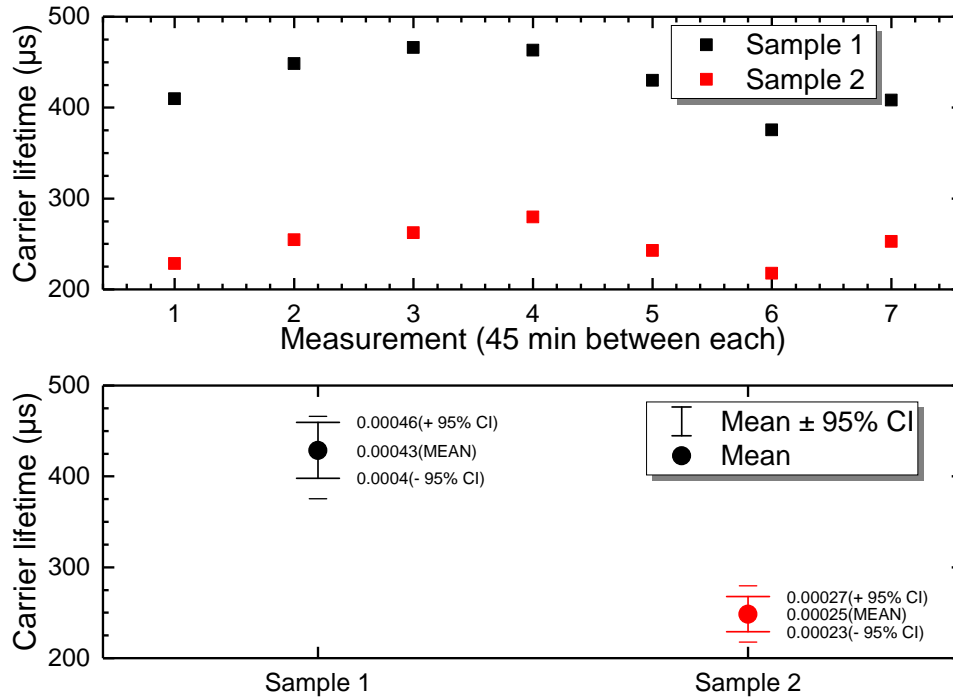


Figure 4.4: Measurements to obtain a qualitative understanding of the errors when measuring degradation in lifetime. Two samples were measured with slight differences in placement throughout one day. There is clearly some variations with the relative placement and an error bar of  $\pm 25 \mu\text{s}$  was deemed appropriate to account for these errors.

These results clearly show that alteration of the wafer placement results in variations in the measured carrier lifetimes. For the two samples, reasonable values seem to be  $430 \pm 30 \mu\text{s}$  and  $250 \pm 20 \mu\text{s}$ , respectively. An error bar of  $\pm 25 \mu\text{s}$  was deemed appropriate to account for these errors in the degradation studies.

### 4.2.2 Storing at different conditions

Due to this severe degradation in carrier lifetime, several wafers were produced with slight differences and stored at different conditions to determine the optimal storage conditions. For the first set of experiments, wafers were produced with: (1) Fast spin and 1% Triton mixed in the PEDOT:PSS solution, (2) Slow spin and 0.1% Triton and (3) Fast spin and 0.1% Triton. These wafers were subsequently stored in: (a) a fridge keeping 4°C, (b) a dark cupboard and (c) an illuminated fume hood. With the exception of two samples, the wafers were stored in closed wafer trays. The measured carrier lifetimes at intervals of approximately 60 days are displayed in figure 4.5.

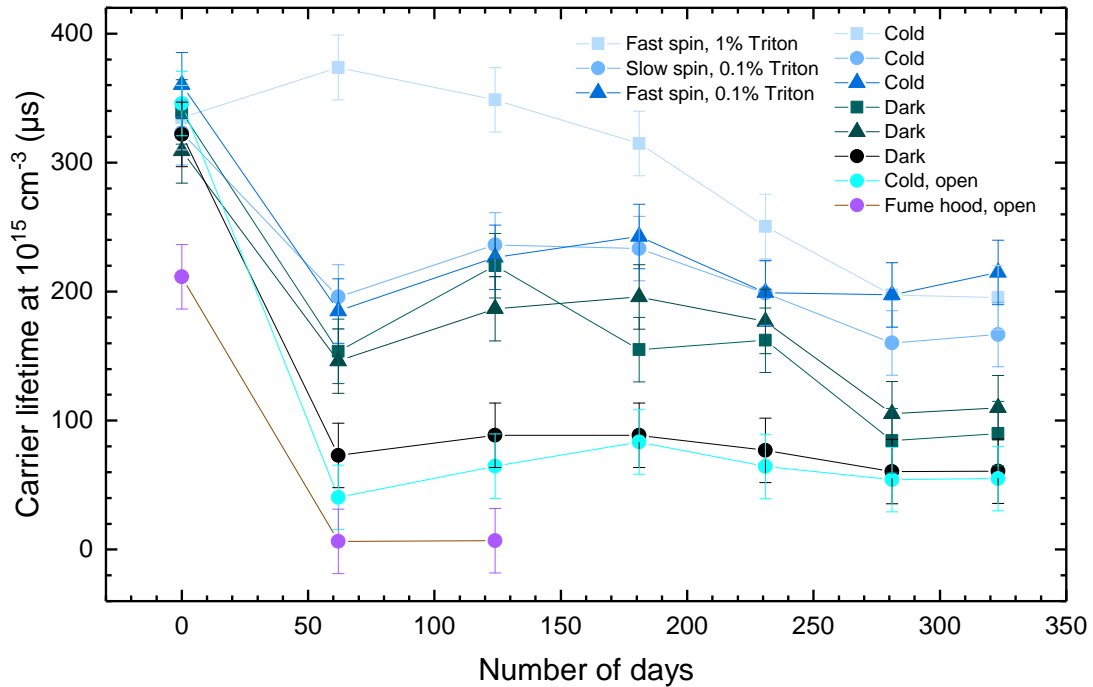


Figure 4.5: Measured carrier lifetime at an injection level of  $1 \times 10^{15} \text{ cm}^{-3}$  for FZ n-type Si wafers passivated with PEDOT:PSS on both sides. The wafers have been fabricated slightly different and stored at different conditions; in a fridge (cold), in a dark cupboard (dark) and exposed in a fume hood. It appears that storing the wafers cold provides the best stability, especially in combination with 1% Triton in the PEDOT:PSS solution.

To start with the bad news; storing the wafer in an open container is clearly bad for the stability, especially in the fume hood where the wafer is exposed to light and could be contaminated from other chemicals also present in the fume hood. The minority carrier lifetime of this wafer dropped to  $\sim 6 \mu\text{s}$  after 62 days and showed the same lifetime after 124 days, and thus not measured further. This underlines the crucial need for encapsulating the finished solar cells.

The wafer stored open in the fridge also shows considerable degradation. This indicates that the closed wafer tray offers some protection against humidity and contaminants since the other three wafers stored in the fridge display considerably less degradation.

After 62 days, there was a clear champion in the wafer with 1% Triton stored cold (blue square), with several wafers lying around  $200 \mu\text{s}$ . After 231 days, however, this gap

seems to be closing, with the majority of the wafers approaching a steady lifetime around 200  $\mu\text{s}$ . Still, the wafers stored cold in a closed tray performs best over the entire range.

Approaching 300 days, the wafers stored in dark ambient shows a further decrease to 100  $\mu\text{s}$ , reaching similar values as seen in figure 4.3. Meanwhile, the wafers stored cold proceed to show the overall best lifetimes, indicating that low temperatures have a beneficial effect on the stability. This seems to stabilise, with the wafers stored cold having lifetimes of roughly 200  $\mu\text{s}$  approaching one year of storage.

Regarding the different spin speeds and compositions, there appears to be little or no effect on initial lifetime or stability. The apparent superior performance of the wafer with 1% Triton and cold storage could originate from a more conformal coating due to enhanced wetting from Triton. This is, however, not represented in the wafer stored in dark ambient conditions.

There is no apparent reason for the excessive degradation of the wafer with a slow spin and 0.1% Triton stored in the dark (represented by black circles), which has similar lifetimes to the wafer stored open in the cold. One could think the slow spin, and therefore a thicker PEDOT:PSS film, is the culprit. However, considering how the wafer with similar fabrication stored cold performs very similar to the others, this appears unlikely. Another possibility is merely experimental errors during preparation. The slow spin was not optimised at this point, causing poor coverage over the wafers represented by circles. This, together with a deviation in the annealing or a wafer tray not fully closed, could explain the observed behaviour.

### Desiccator

Due to the hygroscopic nature of PEDOT:PSS, a natural next step was to store the wafers in an environment with low humidity, as provided by a desiccator. Figure 4.6 shows the change in carrier lifetime for wafers produced identically and stored in a desiccator and dark ambient, respectively. The results are also plotted together with the first degradation test, as shown in figure 4.3. These wafers started with lifetimes a bit lower than the majority of the previously made, typically ranging between 280 and 350  $\mu\text{s}$ . The PEDOT:PSS dispersion was starting to get old at the time of fabrication, and this is probably the reason for the somewhat lower initial lifetime. For the ensuing experiments, a new PEDOT:PSS dispersion was used. Nonetheless, despite the lower initial value, these results give valuable indications on the suspected effect of humidity on degradation.

After 25 days of storage, a gap was starting to form between the two samples stored in the absence of water and the sample stored in ambient. By comparison with the previously found trend, we see how the wafer stored in ambient (green dots) follows the trend quite meticulously while the wafers stored in a desiccator (triangles) deviates from the trend after 25 days and show considerably better stability.

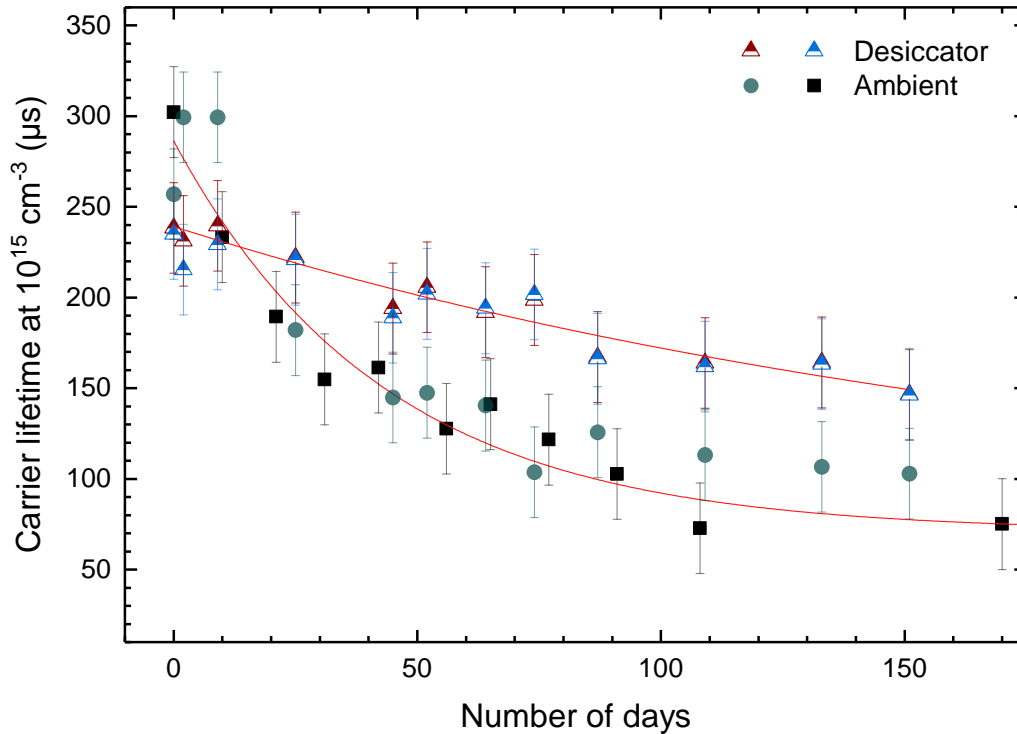


Figure 4.6: Measured carrier lifetime at an injection level of  $1 \times 10^{15} \text{ cm}^{-3}$  for FZ n-type Si wafers passivated with PEDOT:PSS on both sides. Two wafers were stored in a desiccator and one were stored in dark ambient conditions. The wafer stored in ambient follows the exponential decay seen in previous wafers. The wafers stored in desiccator, on the other hand, shows a significantly slower decrease in carrier lifetime.

Unfortunately, these wafers still show degradation in lifetime, just not as severe as the others. This is, therefore, something that needs to be explored further. As discussed in section 2.5.1, Chen *et al.* reported that oxygen is good for the passivation mechanism provided by PSS, while water has a negative impact since a surplus of oxygen to the interface promotes bonding between PSS and Si, while a surplus of water causes the breaking of these bonds and swelling of the polymer [53]. While this is in good agreement with our findings, it also supports the notion that it should be possible to create an encapsulant for these solar cells, which reduces stability issues to a minimum.

It should also be noted that despite the wafers being stored in the desiccator between measurements, the PEDOT:PSS probably absorbs some water when the desiccator is opened to take out wafers and especially when measuring the wafers. Moreover, while the desiccant (silica gel) used in the desiccator definitely reduced the water content, it may not have absorbed everything.

It is theorised that if these wafers were stored and measured in an environment completely free of water, there would be close to no degradation at all. Note that this still is without exposure to excessive UV light or elevated temperatures as these will influence the PEDOT:PSS through other mechanisms.

### 4.2.3 Light-induced enhancement

An enhancement in minority carrier lifetime was observed when performing several consecutive PLI and QSSPC measurements. This appears to be an effect which builds up to a certain point with exposure to high-intensity light and lingers for some time before the effect is subdued. This effect, termed light-induced enhancement (LIE), has been credited to the reduced density of interface states under light soaking [109] and is in excellent agreement with the passivation mechanism described in section 2.5.1.

Figure 4.7 shows the variations in carrier lifetime after exposure to various light soaking and storage conditions.

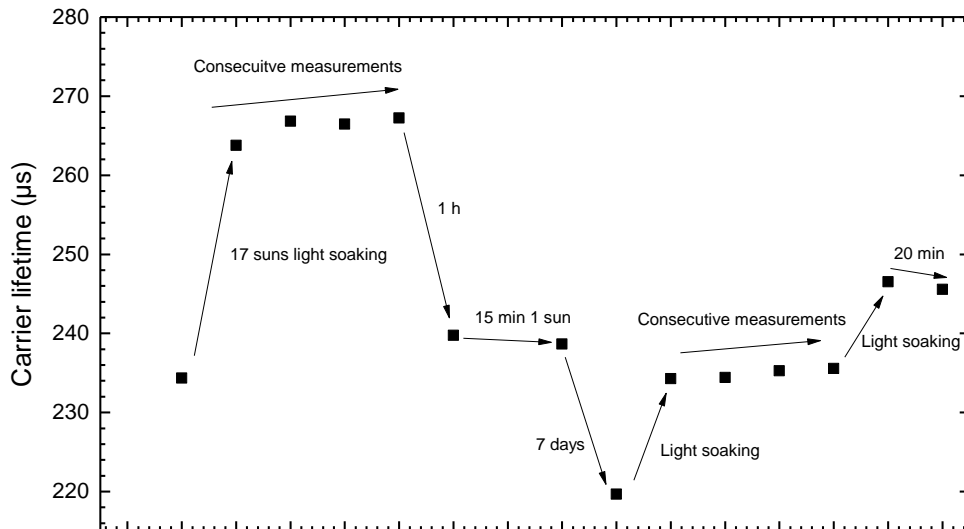


Figure 4.7: Variations in carrier lifetime after exposure to high-intensity light soaking. There is a clear light-induced enhancement after light soaking which subdues some time after exposure. Interestingly, the effect is not seen after prolonged exposure to one sun.

The figure shows how the carrier lifetime increases after high-intensity light soaking, shows a slight further increase with consecutive measurements and recedes back close to the initial value after one hour unperturbed.

15 min under one-sun illumination did, surprisingly, not have any enhancement effect. Hence, it appears as though the reported LIE requires a higher intensity than one sun and may thus not be of much value for real cells. This contradicts the results by Chen *et al.* [109], where an enhancement effect was shown also with one-sun illumination. Further experiments with real cells are required to draw any conclusions.

After seven days in dark storage, the carrier lifetime decreased further. After LS, however, the value surpassed the original value, albeit it did not reach the maximum again. This shows that it might be possible to reduce the severe effect of degradation by occasionally exposing the solar cell to high-intensity light. Again, further experiments with real cells are required to fully understand this effect and its potential benefits.

In conclusion, the LIE effect was evident after exposure to high-intensity LS. It was, however, not evident after exposure to one sun which indicates that this effect, unless

it can be enhanced substantially, is more of a curiosity than an effect which will further enhance the passivation of cells under operation, as claimed by Chen *et al.* [109].

### Summary

*PEDOT:PSS provides excellent passivation on Si, especially n-type due to the nature of the PSS passivation. The passivation degrades over time, mainly credited to absorption of water resulting in swelling of the PSS species and possibly further oxidation of the Si surface. As a result, the degradation is less severe in the absence of water, as made clear by storage in a desiccator. Good encapsulation of the solar cells is thus a requisite for realising PEDOT:PSS/Si solar cells as low-cost, high-efficiency solar cells. Moreover; while challenging to realise for an operational solar cell, the passivation also seems to be more stable if the wafers are stored cold. Lastly, high-intensity light has an enhancement effect on the passivation. Whether this effect will be present for real cells under operation is, however, not known and will need further experiments.*

## 4.3 Electrical characterisation

In this section, the initial electrical characterisation is presented. First, the sheet resistance is compared to the literature. Then, initial IV curves are shown, displaying severely limited performance due to extraction barriers. Finally, the barriers are overcome through an optimised process.

### 4.3.1 Sheet Resistance

Values obtained from TLM measurements of PEDOT:PSS on high-resistivity silicon wafers are presented in table 4.1. The use of a high-resistivity substrate ensures that the obtained values are purely from the PEDOT:PSS layer and front contact, the front contact here being Ag.

*Table 4.1: Values obtained by TLM measurements of PEDOT:PSS on high-resistivity wafers. The sheet resistance is in excellent agreement with reported values. Furthermore, both contact resistance and resistivity are sufficiently low to avoid any severe losses in performance.*

	Sheet resistance	Contact resistance	Contact resistivity
<b>Sample 1</b>	161 $\Omega/\square$	0.98 $\Omega$	$1.0 \times 10^{-3} \Omega\text{cm}^2$
<b>Sample 2</b>	134 $\Omega/\square$	1.18 $\Omega$	$1.7 \times 10^{-3} \Omega\text{cm}^2$

The PEDOT:PSS layer has a sheet resistance around 134–161  $\Omega/\square$  and the front contact has a contact resistivity on the order of  $10^{-3} \Omega\text{cm}^2$ . This is sufficiently low to avoid big losses in  $\eta$  and the sheet resistance of PEDOT:PSS is in good agreement with values

reported in the literature. Thomas and Leung reported  $R_{sh} = 212\text{--}260\ \Omega/\square$  [65] and later  $R_{sh} = 128\text{--}254\ \Omega/\square$  [37]. Zielke *et al.* reported a value of  $100\ \Omega/\square$ .

Mu *et al.* [52] reported an initial contact resistance of  $2.32\ \Omega$  for Ag/PEDOT:PSS which dropped to  $1.64\ \Omega$  by inserting a thin  $\text{WO}_3$  interlayer between Ag and PEDOT:PSS. Moreover, Yang *et al.* [101] simulated the effect of contact resistance on FF and  $\eta$ , going from 5 to  $0.1\ \Omega$ . They found a huge increase in both parameters going from 5 to  $1\ \Omega$ . From 1 to  $0.1\ \Omega$ , however, only a slight further increase was observed. Our contact resistances around  $1\ \Omega$  without any additional interlayer is thus considered to be satisfactory. However, to fully realise the high efficiency potential, contact resistances should ideally drop below  $0.5\ \Omega$  and contact resistivities should approach  $10^{-6}\ \Omega\text{cm}^2$  [110].

### 4.3.2 Current-voltage

In order to make the fabrication process as simple and low-cost as possible, the initial aim was to fabricate simple solar cell architectures without any pre-treatment to the n-type FZ Si wafers and therefore keeping the native oxide formed at production as the interface between PEDOT:PSS and n-Si. The resulting IV curves are presented in figure 4.8. These are from a  $6.25\ \text{cm}^2$  solar cell with silver as both front and back contact.

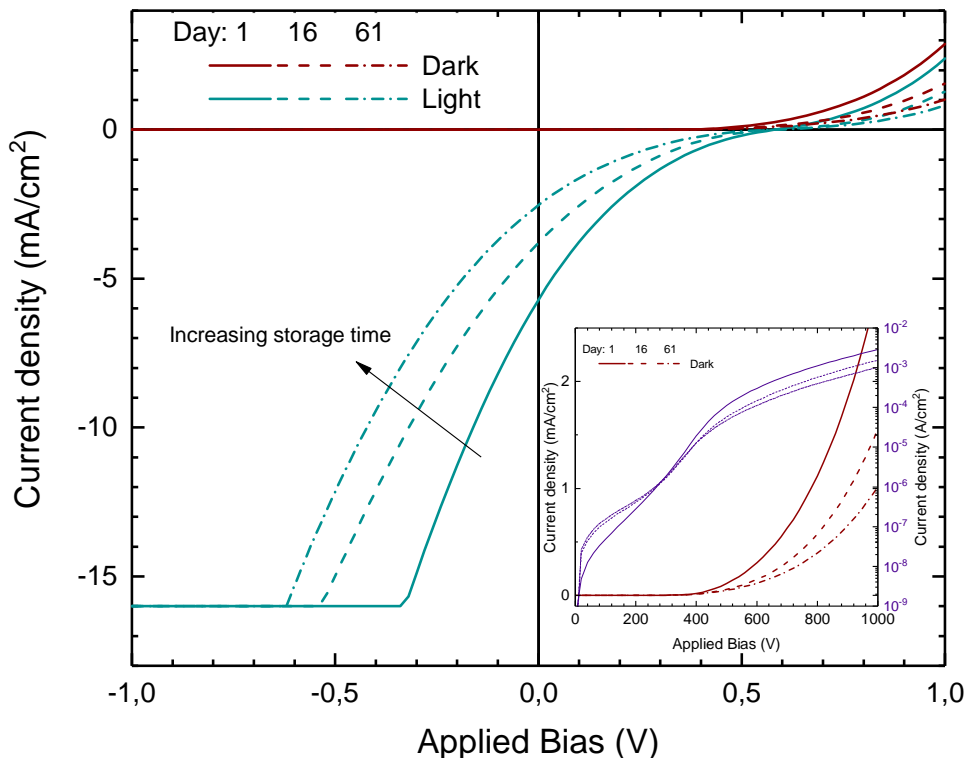


Figure 4.8: IV curves from a PEDOT:PSS/n-Si solar cell with the original native oxide at the interface. An s-shape is clearly present drastically limiting the FF of the cell. In addition, the already poor performance shows a clear degradation after 16 and 61 days.

The solar cell clearly exhibits some light response, since the curve shifts down to a negative current when measuring under illumination. However, instead of the ideal case where the illuminated curve is similar to the dark curve only shifted to some negative current, the illuminated curve takes the form of an s-shape. This shape, as discussed in section 2.1.2, has a severe effect on both the short-circuit current and the fill factor, resulting in a much lower efficiency than if this s-shape was to disappear. (Note that the saturation of the current at large reverse bias is due to the instrument cut-off. Due to this, new shadow masks of  $1\text{ cm}^2$  were fabricated and used to make cells of this dimension for subsequent experiments.)

### Stability

The solar cell was stored in dark ambient and measured again after 16 and 61 days, as shown by the dashed lines in figure 4.8. As expected, the IV curves show some stability issues with a severe degradation in both short-circuit current and fill factor. Interestingly, the degradation in power seems to have about the same magnitude as the degradation in carrier lifetime from figure 4.3. This could imply a close relationship between the carrier lifetime and the power output of the device. The degradation is also visible in the dark IV curves as shown in the inset in figure 4.8. The semi-logarithmic plot shows the transition to a less ideal diode with more SCR recombination dominating at low bias after storage.

### Au/Ag front contact

Since the observed s-shape is likely to stem from a charge transport barrier at either the front contact (on PEDOT:PSS) or the interface between PEDOT:PSS and Si, these should be modified. In order to check the effect of another metal contact and hopefully increase the charge extraction, the Ag front contact was replaced by a stack of 10 nm Au and 250 nm Ag. Since Au has a higher work function than both Ag and PEDOT:PSS, this should provide better ohmic contact [110]. The resulting IV curve from a  $1\text{ cm}^2$  cell with an original native oxide and Au/Ag stack as the front contact is shown together with the previously seen Ag-only curve in figure 4.9.

It appears as though the modified front contact improves the performance - the S seems to start later and is less pronounced. While the S presumably starts far into the reverse bias regime for the Ag-only curve, the S-shape does not appear until around  $-0.25\text{ V}$  with the Au/Ag stack. As a result, the effect on the short-circuit current is not as severe. However, the fill factor is still heavily reduced. It now seemed prudent to turn the gaze to the interface between PEDOT:PSS and Si due to a suspicion that the original native oxide was too thick, resulting in a barrier for charge transport.

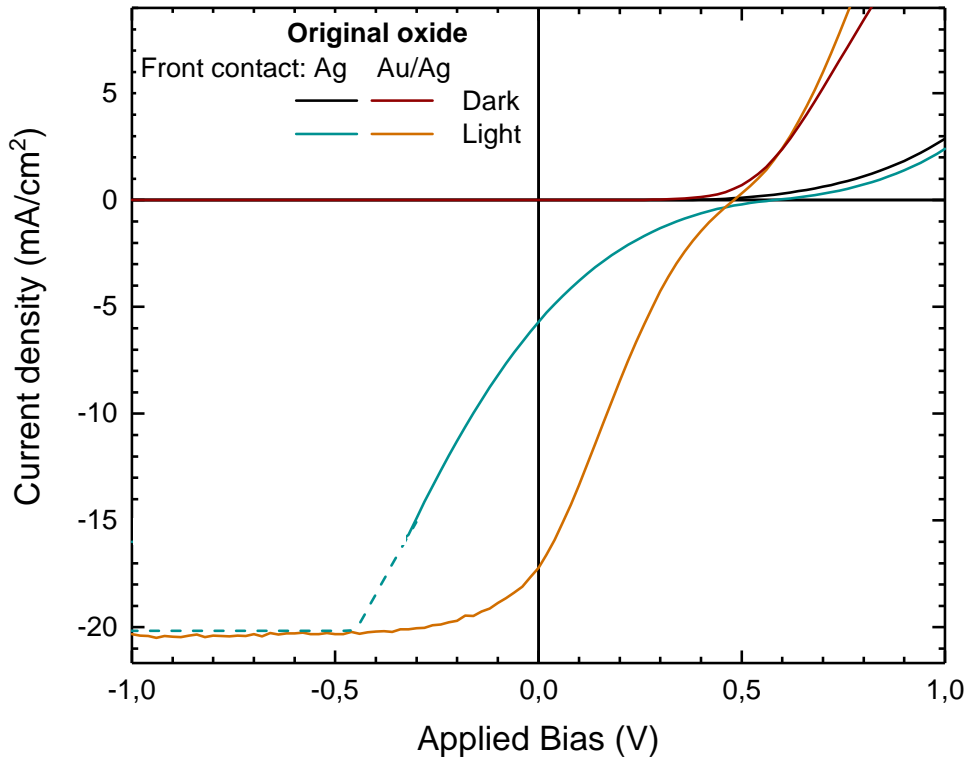


Figure 4.9: Comparison of different front contacts. The Au/Ag stack has a positive effect on the S-shape by making it less pronounced, but does not make it disappear. Thus, further optimising is needed. The dashed line is the predicted behaviour without the instrument cut-off.

### 4.3.3 Growing a native oxide

Previous work conducted at IFE had experienced difficulty with spin-coating PEDOT:PSS after HF treatment of the Si wafer, credited to the hydrophobicity of the resulting H-terminated surface. This was, however, not a problem this time around, possibly due to the lower spin speed or the admixture of more Triton. With the aim of producing cells with a freshly grown native oxide of various thickness, the wafers were left for various times in ambient conditions before spin-coating PEDOT:PSS, metallising and measuring the samples. IV curves of these samples are displayed in figure 4.10. The resulting IV curves are briefly discussed here and will be analysed in more detail in section 4.4.1

For the entire series with freshly grown native oxides, the S-shapes are no longer present, giving a reason to believe that the original interfacial oxide indeed was too thick. Moreover, the HF treatment is known to introduce hydrogen in the near-surface region of Si. Since oxygen species break Si-Si bonds to form  $\text{SiO}_2$  as discussed in-depth by Morita *et al.* [27], the fresh  $\text{SiO}_2$  surface will be passivated by hydrogen. This may, in turn, provide a better interface to PEDOT:PSS compared to the untreated wafers. Alternatively, there could be some chemical residue or contaminants present on the untreated wafer. This does, however, seem unlikely.

Compared to values from the literature ([10], [12], [54], [111]), both the short-circuit currents and the open-circuit voltages are a bit low. The fill factor, on the other hand, is comparable to the best found in the literature for PEDOT:PSS/Si solar cells.

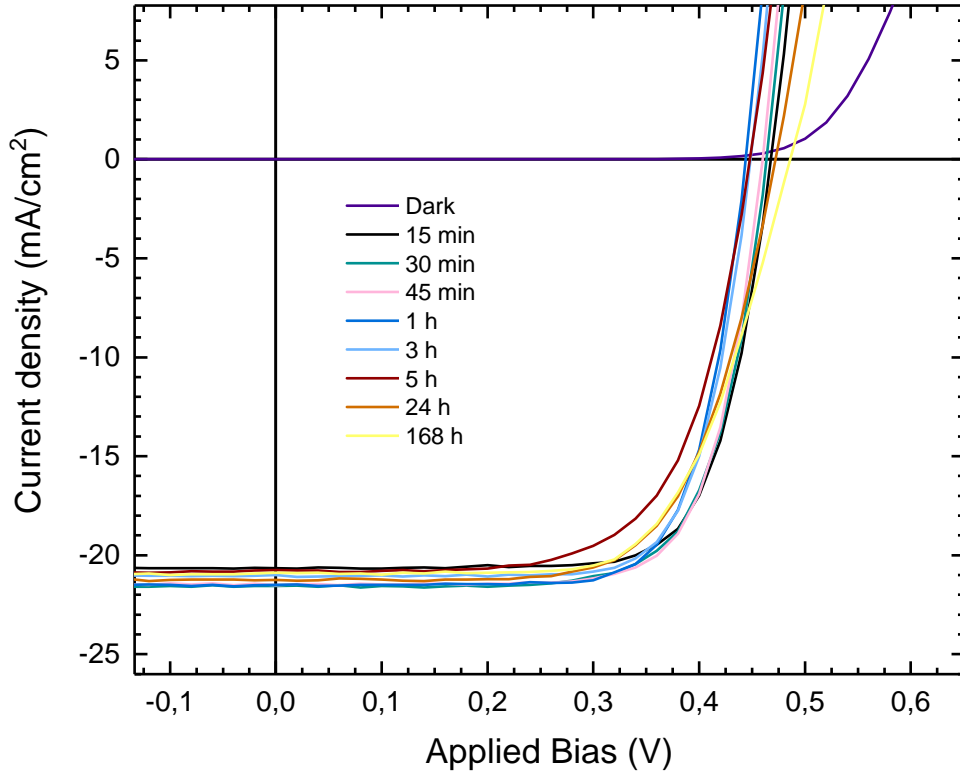


Figure 4.10: IV curves from PEDOT:PSS/SiO<sub>2</sub>/n-Si solar cells with a freshly grown native oxide and Au/Ag front contact. The growth of a new oxide resulted in the complete removal of s-shapes and the entire range of oxide growth shows good initial performance with suitable rectifying properties.

The low  $J_{sc}$  is mostly due to shading from the metal grid and a lack of texturing. In addition, the illumination setup used was found to provide illumination varying between 0.9 and 1 sun. This was corrected for when plotting the data by using a correction factor found from control measurements with the exact intensity known. Nevertheless, an error of  $\pm 1$  mA/cm<sup>2</sup> could originate from this correction. A lower intensity will naturally have a severe effect on  $J_{sc}$ , but also a small effect on  $V_{oc}$ .

A  $V_{oc}$  around 470 mV is quite low compared to values of 645 mV and 688 mV quoted as the champion cells by Pietsch *et al.* [36] and Gogolin *et al.* [111], respectively. It is worth noting that the 645 mV from Pietsch was with a high donor doping of  $2.6 \times 10^{16}$  cm<sup>-3</sup>. Their best  $V_{oc}$  for a donor doping of  $2.0 \times 10^{15}$  cm<sup>-3</sup>, which is comparable to our wafers being in the range  $9.1 \times 10^{14}$  -  $4.9 \times 10^{15}$  cm<sup>-3</sup>, was 569 mV. The effect of donor doping on  $V_{oc}$  will be further discussed in section 4.5.1.

The all-time high value of 688 mV from Gogolin *et al.* comes from their backPEDOT concept, where PEDOT:PSS is placed on the entire rear of a p-type Si wafer, and the front is passivated by a-Si:H and indium tin oxide (ITO). ITO improves the lateral conductivity and ensures good contact without the need for excessive metal or doping. While this is an interesting concept, these cells are not fully comparable to the once made in this thesis. Moreover, these cells are not really low-cost. Nonetheless, it shows the great potential of a PEDOT:PSS/Si-based solar cell.

The low  $V_{oc}$  is suspected to mostly arise from the lack of any back-surface passivation since  $V_{oc}$  is known to show a strong dependence on rear surface passivation,  $S_{rear}$  [51]. This will also be discussed in more detail in section 4.5.1. Besides, the back contact of Ag used here is not ideal for making an ohmic contact on n-type Si due to the large difference in work function of Ag and n-type Si.

*In conclusion, growing a new native oxide eliminated the s-shape and therefore drastically increased the FF, leading to suitable rectifying properties. However, further optimisation of the interface could probably further increase the efficiency, particularly by increasing the open-circuit voltage.*

The IV curves shown in figure 4.10 are the champion cells for each differently grown oxide. Since four grids were fabricated and isolated on each wafer, every sample yielded four replicates and thus a span of IV curves. Figure 4.11 shows such a span of IV curves for the sample with a native oxide grown for 24 hours in ambient.

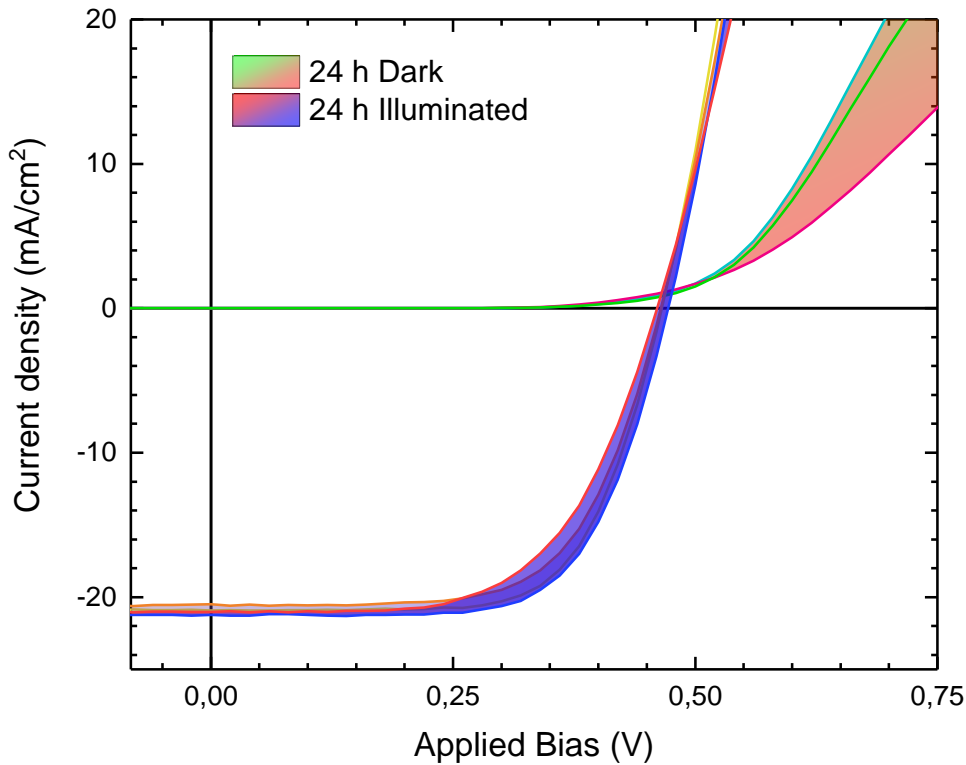


*Figure 4.11: The span of IV curves for the four isolated PEDOT:PSS/SiO<sub>2</sub>/n-Si solar cells with the SiO<sub>2</sub> layer grown for 24 hours at ambient conditions. Slight differences are observed, mainly credited to variations in the PEDOT:PSS film and the isolation by washing.*

From the illuminated IV curves, it seems evident that the solar cells behave very similarly. There are slight differences, most notably in FF, but also in  $J_{sc}$  and  $V_{oc}$ . This is probably a result of subtle differences in the PEDOT:PSS film after spin coating and isolation of the cells by washing.

Another interesting aspect is the shift in IV curves going from dark to illuminated. This deviation, where the illuminated curves are shifted by roughly 0.1 V to lower applied bias, could be due to series resistance. This may originate from some unfavourable band alignment still present at the interface (even though the S-shapes are gone, the band alignment at the interface might not be fully optimised), the lack of surface passivation on the back surface and the back contact.

A natural next step would be to apply back-side passivation, for instance, through a traditional phosphorous diffusion or siloxane oligomers as done by Yoon *et al.* [72]. This is, however, outside the scope of this work.

### 4.3.4 Summary

*Through adapting a more suitable front contact and growing a new native oxide, superior solar cell performance for PEDOT:PSS/n-Si solar cells is achieved compared to previous results at IFE. The entire range of growth conditions for SiO<sub>2</sub> (15 min - 7 days) resulted in solar cells with good initial performance. Moreover, PEDOT:PSS has been shown to have sufficiently low sheet resistance for high-efficiency solar cells. Further advances should be achieved by applying a suitable back-side passivation and optimising the back contact.*

## 4.4 The effect of different interfacial layers

This section first provides a thorough comparison of the solar cells with varying native oxide growth, both in terms of initial performance and long-term stability. Following this, three different interlayers are investigated: Aluminum oxide grown by ALD, a-Si deposited by PECVD and a chemically grown SiO<sub>2</sub>.

In order to get a good flow and easily relate solar cell characteristics to carrier lifetime, both results from electrical characterisation and lifetime measurements are shown together for each interlayer.

### 4.4.1 Native SiO<sub>2</sub> grown in ambient

Focusing on the interface, a systematic series of varying oxide growth time was conducted. With the aim of studying the change in the solar cell parameters ( $V_{oc}$ ,  $J_{sc}$ ,  $FF$  and  $\eta$ ) and the carrier lifetime, wafers were left to oxidise for varying amounts of time in ambient. Figure 4.12 shows the performance of the solar cells as a function of oxide growth time. Each of the four isolated cells on each wafer with different treatment were measured and fitted. The average value and standard deviation from the four solar cells are shown together with the value for the champion cell of each wafer. Corrected average values considering a shading of only 5% are also shown. The error bars represent the standard deviations of each parameter on the four solar cells and can thus be considered as a measure of the reliability of the results.

### Calculating corrected values

Due to a lack of time, the contact pattern was not optimised to give minimal resistive losses in the busbar and shading losses. This should, however, be easy to optimise at a later point. To give an idea of the obtainable values with reduced shading, the values were corrected according to the following considerations:

The fabricated cells had a shading of 28% due to the front grid, leaving 72% of the cell exposed to the incoming light. With only 5% shading, 95% of the incoming light would be transmitted to the cell. To find our correction factor,  $f$ , we find the relation between the transmittance into the cell with the real and the expected shading:

$$f = \frac{1 - 0.05}{1 - 0.28} = \frac{0.95}{0.72} = 1.32 \quad (4.1)$$

The reduced effective area is expected to affect primarily the  $J_{sc}$ , but also  $V_{oc}$ .  $J_{sc}$  scales linearly with the area. Thus, by multiplying the correction factor with the measured  $J_{sc}$ , we get the corrected short-circuit current  $J'_{sc}$ :

$$J'_{sc} = f \times J_{sc} \quad (4.2)$$

and by inserting the same relation to the expression for the  $V_{oc}$ , the corrected open-circuit voltage  $V'_{oc}$  becomes

$$\begin{aligned} V'_{oc} &= \frac{nk_B T}{q} \ln \left( \frac{f \times J_{sc}}{J_0} + 1 \right) \\ &= \frac{nk_B T}{q} \ln(f) + \frac{nk_B T}{q} \ln \left( \frac{J_{sc}}{J_0} + 1 \right) \\ &= \frac{nk_B T}{q} \ln(f) + V_{oc} \end{aligned} \quad (4.3)$$

Finally, the corrected efficiency is given by

$$\eta' = \frac{J'_{sc} V'_{oc} FF}{P_s} \quad (4.4)$$

We have here assumed that the fill factor will remain unaffected with an optimised front grid reducing the shading to 5%. In practice, there is an important trade-off between  $J_{sc}$  and  $FF$ . Reducing the width and spacing of the grid increases  $J_{sc}$  by enabling absorption of more light. However, it simultaneously increases resistive losses and may thereby reduce the  $FF$ . Nevertheless, shading of 5% should be possible with an optimised contact structure without compromising the fill factor significantly.

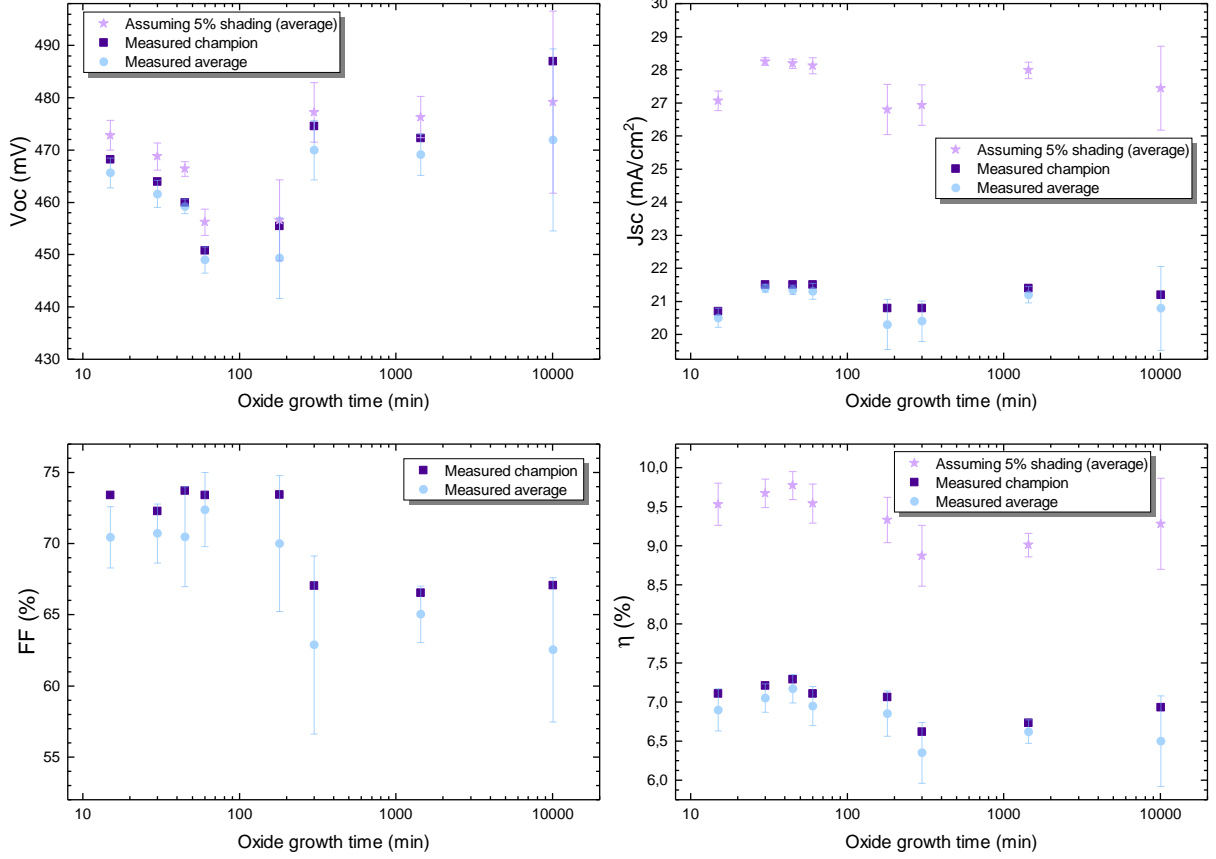


Figure 4.12: IV parameters as a function of oxide growth time, both average values as-measured and corrected for shading, and measured values for each champion cell.  $V_{oc}$  (top left),  $J_{sc}$  (top right), FF (bottom left) and  $\eta$  (bottom right). The error bars represent the standard deviation of each value for the four isolated cells.

There is no clear trend for the open-circuit voltage. The highest value of 486 mV is obtained for the longest oxide growth time (168 hours) and therefore, the thickest oxide. The lowest  $V_{oc}$  is obtained for the sample with one-hour oxide growth. While this could look like the  $V_{oc}$  starts off bad and increases with longer oxide growth, the sample with only 15 min growth has the 4th best  $V_{oc}$  of 468 mV. It is therefore thought that the observed variations in  $V_{oc}$  are mostly due to some other effect, such as variations in morphology and thickness of the PEDOT:PSS layer of the active area or slight differences in contact properties. Moreover,  $V_{oc}$  depends strongly on the passivation of the samples and the ambient temperature, both of which may have varied a little between the samples. Additionally, the uncertainties regarding the thickest oxides are significant, particularly for FF and  $V_{oc}$ . This could stem from variations in the contact between PEDOT:PSS and SiO<sub>2</sub> or poor contact between the measuring probe and contact.

The short-circuit current density is clearly independent of the oxide growth. This is rather expected since  $J_{sc}$  is heavily dependent on the transmission of the cell and the absorption of light in the cell. None of these should be much affected by slight differences in the thickness of the interface layer. This is also supported by the small uncertainties.

The fill factor, on the other hand, shows an interesting trend. The highest FF of 73.7% is obtained for the 45 min growth, with all the samples with 15-180 min growth times exhibiting excellent fill factors. With longer oxide growth, however, a drop in FF is observed. This is credited to more resistive losses as the tunnelling oxide becomes larger. Although there are significant uncertainties, especially related to 180, 300 and 10800 min growth, the trend appears plausible.

Mostly credited to the FF trend, the highest efficiency is obtained for the solar cell with an oxide layer grown for 45 min, closely followed by the entire range of 15-180 min growth times. From there, a slight decrease in efficiency is observed, but, due to the increased  $V_{oc}$  for the longest growth times, the reduced FF is not detrimental to  $\eta$ . Nonetheless, the trends show that the thin interfacial oxide provided by 45 min growth in ambient conditions provides the best solar cell with an efficiency approaching 10% by assuming only 5% shading. Furthermore, the trend does not seem likely to differ within the uncertainties. The efficiencies for the champion cells are summarised in table 4.2.

Table 4.2: Table of measured and assumed values of efficiency for the champion solar cells with varying native oxide growth.

Oxide growth time [min]	15	30	45	60	180	300	1440	10080
Measured $\eta$ [%]	7.11	7.21	7.29	7.11	7.06	6.62	6.73	6.93
$\eta$ assuming 5% shading [%]	9.53	9.67	9.77	9.54	9.33	8.87	9.01	9.28

Considering the lack of back surface passivation, these values are comparable to efficiencies quoted in the literature [44], [87], [98], [112]. However, to reach the record values of 17.3% (PEDOT frontside, [72]) and 20.6% (PEDOT backside, [12]), further advances are needed, in particular through back surface passivation and texturing.

### Passivation

The carrier lifetimes for the same series of oxide growth times are shown in figure 4.13. Values for the lifetime obtained by both QSSPC and calibrated PLI are shown, together with calculated SRV values based on the values from QSSPC. The reported PL values are the mean values from a square of  $\sim 2 \text{ cm}^2$  in the middle of the wafer. The reason for the low value and significant uncertainty in the QSSPC value of the most prolonged oxide growth (10080 min) is poor coverage of PEDOT:PSS on the wafer. As a result, the active part of the wafer did not fully cover the QSSPC coil. Thus, the measured value is much lower than the real value. This should, however, not affect the calibrated PL value.

Overall, all the samples exhibit excellent carrier lifetimes in the range 400–600  $\mu\text{s}$ , corresponding to SRVs of 23–35 cm/s. This is even better passivation than for the untreated wafers seen in section 4.1 and shows that the growth of a new oxide also benefits the passivation.

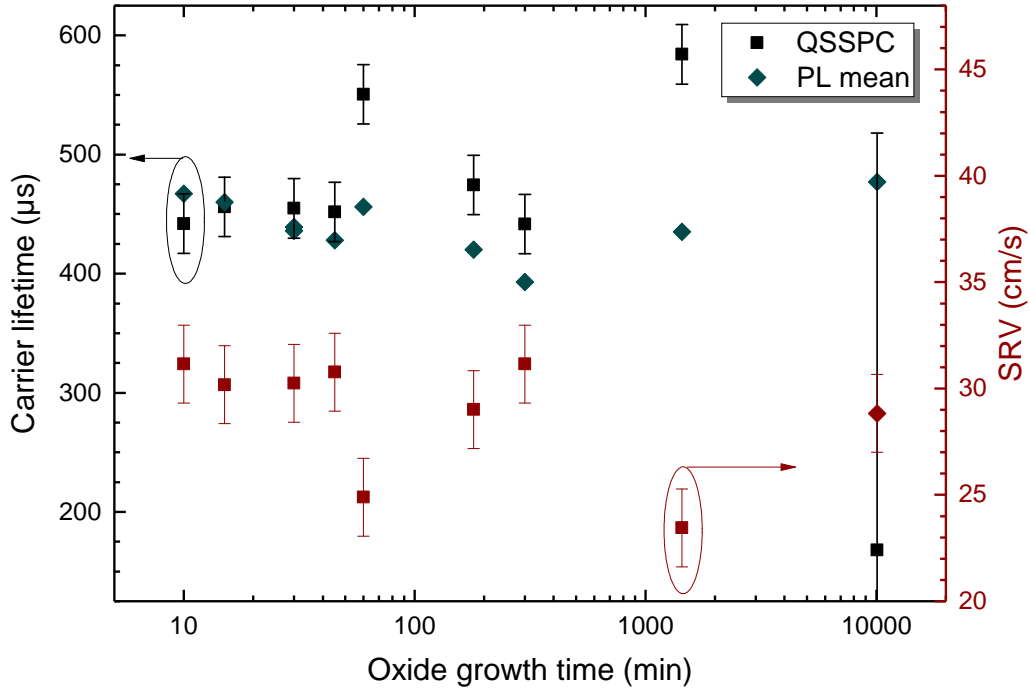


Figure 4.13: The carrier lifetime as a function of oxide growth, both measured QSSPC values and mean PL lifetime measured at the middle of each sample. Large uncertainty in the QSSPC value for 10080 min (7 days) growth due to poor coverage of PEDOT:PSS on the wafer. The SRV values are also shown, calculated from the QSSPC values, except for the longest oxide growth which is calculated from the mean PL value.

## Stability

Both carrier lifetime and IV were measured at regular intervals after fabrication to explore the stability of the samples. All the samples from 15 min to 24 h oxide growth time were stored in a desiccator, and we thus expect the samples to be relatively stable. Due to a lack of space, the wafer with 168 h oxide growth time was not stored in the desiccator. Figures 4.14 and 4.16 show the evolution of efficiency and fill factor, and carrier lifetime, respectively, for the different solar cells.

Firstly, there is a close relationship between the decrease in  $\eta$  and  $FF$ . There is close to no change in  $V_{oc}$  and  $J_{sc}$  (not shown), so the degradation occurs almost purely in the decrease of the fill factor. This points to some resistive losses being introduced from the degradation; probably increased resistivity in PEDOT:PSS due to swelling of the grains and reduced passivation, possibly in combination with further oxide growth at the interface.

Secondly, the degradation is more severe with a longer oxide growth and thus a thicker oxide layer. As seen from both the change in  $FF$  and  $\eta$ , there is almost no degradation for the thinnest oxides (15 - 45 min), slightly more degradation for the middle oxides (1-5 h) and considerably more for the thickest oxides (24-168 h). The excessive degradation in the cell with the thickest oxide (168 h) is expected to be partly due to the higher relative humidity in ambient conditions. However, by also looking at the degradation for

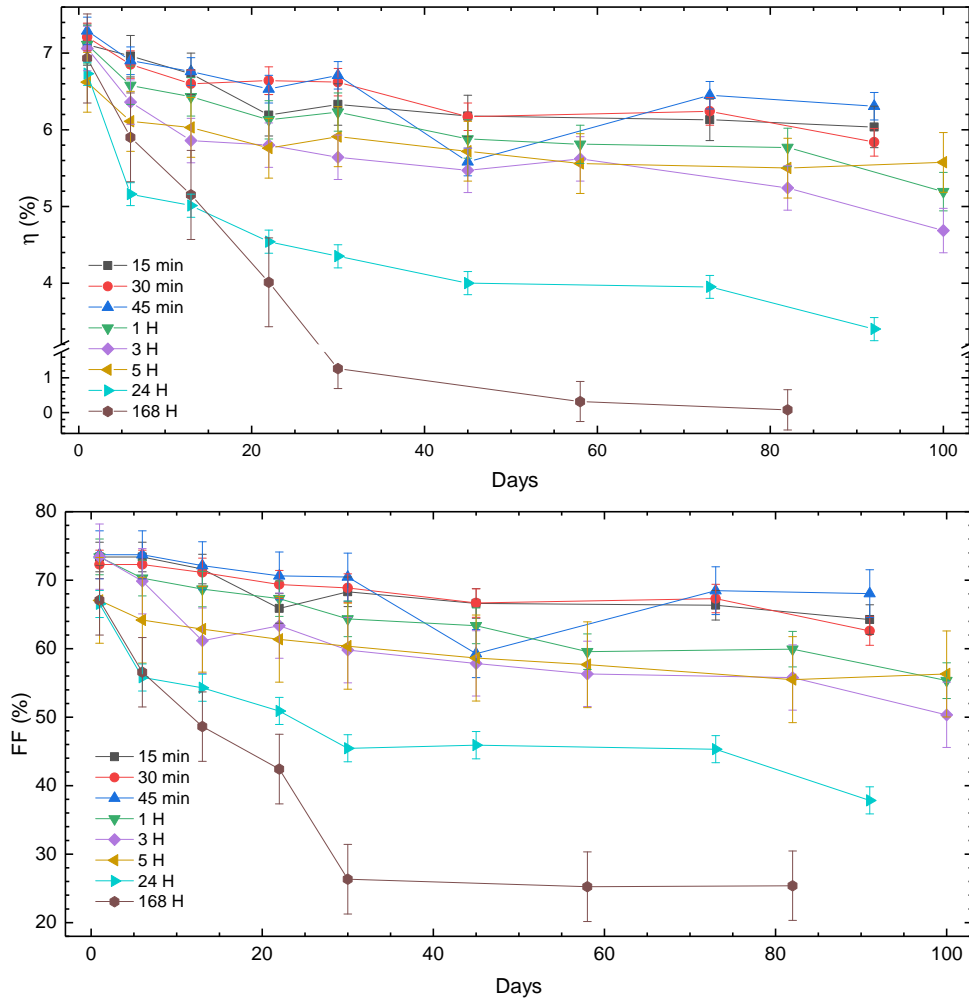


Figure 4.14: Degradation in efficiency (top) and fill factor (bottom) for the solar cells with different native oxide growth times. There is close to no degradation for the thinnest oxides (15 - 45 min), slightly more for the middle range (1 - 5 h) and considerable degradation for the thickest oxides (24 - 168 h). This strongly points to a correlation between oxide thickness and stability. The fluctuation seen for the blue lines (45 min) at day 45 probably stems from a change in temperature or light intensity, or slightly bad contact between the sample and measuring probes.

the cell with 24 h growth time, it becomes evident that the oxide thickness influences the degradation.

One possible reason for this behaviour is that oxygen diffuses to the  $\text{SiO}_2/\text{Si}$  surface and further oxidise the Si surface, resulting in a larger barrier for the minority carriers. This would naturally be the case for all the samples, but the effect could be more pronounced with the thicker oxides considering that there is a trade-off between a sufficiently thick oxide for surface passivation and a sufficiently thin oxide for the transport of minority carriers. It seems likely that the thickest oxides in this series are closer to the upper end of the possible thickness.

To further explore this, figure 4.15 displays the measured IV curves for the solar cells with the longest oxide growth times (24 and 168 h). As the storage time increases, there is an apparent increase in series resistance for both the samples. For the cell with thickest

oxide and storage in ambient there is also the onset of s-shapes, with several kinks present, after 36 days of storage. The severe degradation of cell efficiency, with 4% at day 21, 1.3% at day 36, 0.3% at day 60 and 0.1 % at day 78 is clearly due to reduced FF,  $V_{oc}$  and, for day 36 and onwards, also  $J_{sc}$ .

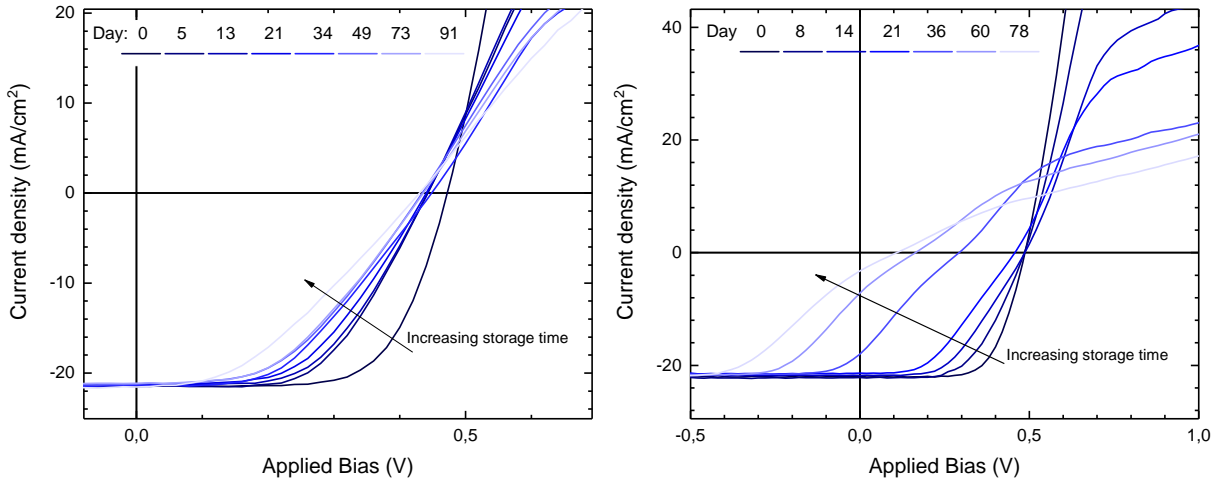


Figure 4.15: The effect of storage on IV performance for the solar cell with the two thickest native oxides, 24 h growth (left) and 168 h growth (right). There is a severe degradation in cell performance promoted by series resistance for both solar cells, and additionally the occurrence of kinks, or s-shapes, for the thickest oxide growth which was stored in ambient.

The difference between the storage conditions of these cells is merely the relative humidity under storage. As a result, there should be no differences in the degradation mechanisms themselves, only the rate at which the degradation proceeds. This re-emergence of severe s-shapes is credited to interfacial extraction barriers. Considering that the only difference between these solar cells is the oxide thickness and relative humidity under storage, it seems very likely that the oxide continues to grow under storage, at least to a certain extent. This is supporting predictions made by Jäckle *et al.* [39], [46], [54].

Moreover, this oxide growth eventually leads to the onset of s-shapes which are detrimental to the solar cell performance, particularly if not stored in a dehumidified environment. Consequently, the emergence of s-shapes as seen for the cell with the thickest oxide is expected to ultimately occur for all solar cells with a native oxide at the interface unless sufficient encapsulation is provided.

Lastly, looking at the evolution in carrier lifetime, the initially high lifetimes of 400–600  $\mu\text{s}$  quickly degrades to 200–350  $\mu\text{s}$  and seems to stabilise at 175–250  $\mu\text{s}$ , corresponding to SRVs of 55.5–79.5 cm/s. Albeit considerably lower than the initial values, this is still more than sufficient, as again seen by the stable efficiencies (at least for the thinner oxides). Provided superior back-surface passivation, the need for lower SRVs may arise. This should, however, be possible by good encapsulation, retaining the high initial carrier lifetimes. Additionally, the use of a bilayer of PEDOT:PSS or siloxane oligomers, as discussed in section 2.6 have the potential to further reduce the front surface recombination if needed.

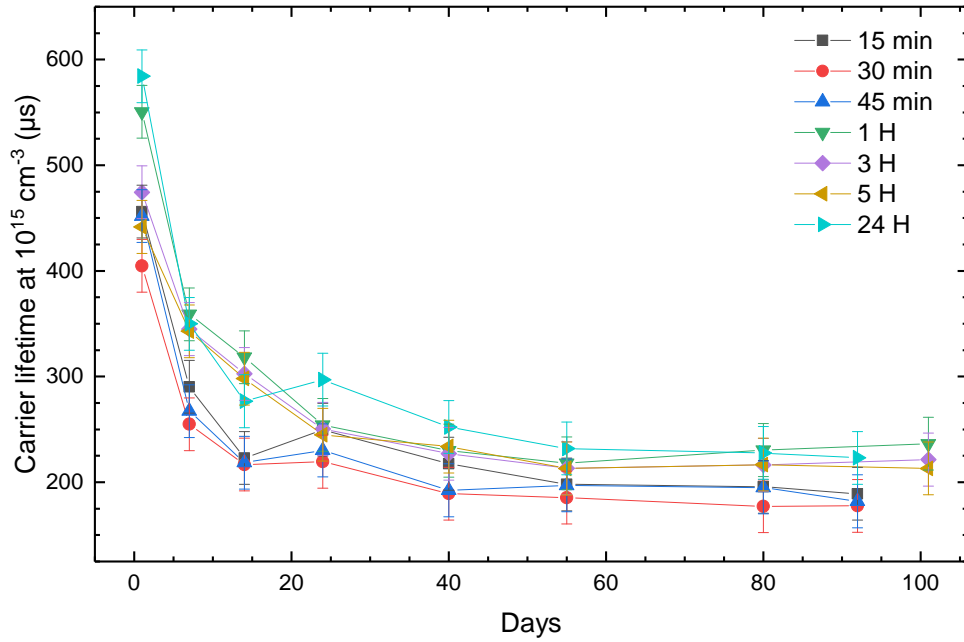


Figure 4.16: Degradation in carrier lifetime for solar cells with different native oxide growth times measured by QSSPC. The initially very high lifetime of 400–600  $\mu\text{s}$  degrades quite severely, but seems to stabilise at 175–250  $\mu\text{s}$ , corresponding to SRVs of 55.5–79.5  $\text{cm/s}$ .

Due to the significant uncertainties in the carrier lifetime of the thickest oxide, it is difficult to compare the change in  $\eta$  and  $FF$  to the carrier lifetime for the thickest oxide. Based on the 24 hour growth, however, the degradation in carrier lifetime alone is not sufficient to explain the degradation in  $\eta$  and  $FF$ . This supports the notion of at least two different degradation mechanisms as already discussed, namely both swelling of PEDOT:PSS and further oxidation of the Si surface.

### Built-in voltage

Figure 4.17 shows the extrapolated values for the built-in voltage,  $V_{bi}$ , obtained from several CV curves for each different oxide growth time. The error bars show the standard deviation in the extrapolated values for each growth time. Although there are some variations, the  $V_{bi}$  seems to lay quite steady around 670 mV. As mentioned in section 3.2.3,  $V_{bi}$  can be used as an approximation to the upper limit of the device  $V_{oc}$ , which again supports the potential of high open-circuit voltage provided sufficient backside passivation.

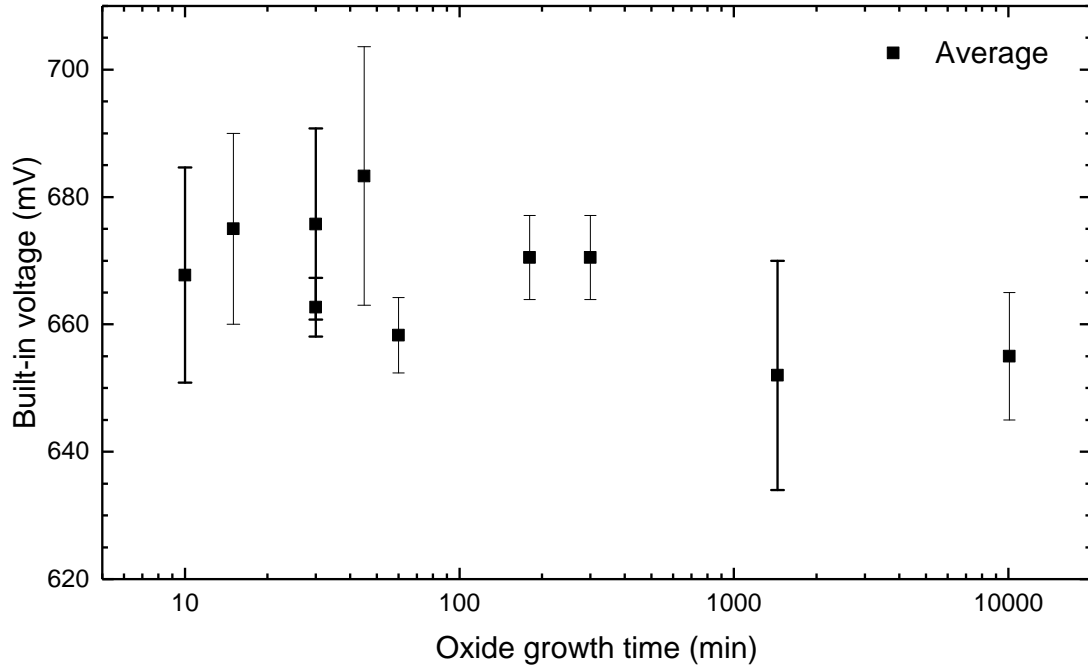


Figure 4.17: Built-in voltages extrapolated from CV measurements showing a  $V_{bi}$  around 670 mV. Error bars show the standard deviation in set of extrapolated values.

## Summary

Further study of the solar cells with regrown native oxides have shown excellent performance, with efficiencies approaching 10% for a theoretical shading of only 5% and superior passivation shown by SRVs around 30 cm/s. Moreover, we can conclude that there is a strong correlation between oxide thickness and degradation, with excellent stability for the thinnest oxides and worse stability for the thickest oxides, credited to further growth of  $\text{SiO}_2$  in addition to increased resistivity of PEDOT:PSS. The passivation also degrades, apparently independent of the oxide thickness, but retains SRVs below 80 cm/s even after 100 days of storage. This is probably due to swelling of PEDOT:PSS due to some humidity still present in the desiccator. The solar cells are also shown to have built-in voltages of  $\sim 670$  mV. This supports the potential for high  $V_{oc}$  if recombination can be limited through better passivation, particularly on the backside.

### 4.4.2 Aluminium Oxide

In order to study the effect of using a different interface oxide, ALD was used to grow  $\text{Al}_2\text{O}_3$  on n-Si. The wafers with  $\text{Al}_2\text{O}_3$  were annealed for 10 min at 400°C before spin-coating PEDOT:PSS on top. Figure 4.18 shows the IV curves and the carrier lifetime measured for PEDOT:PSS/ $\text{Al}_2\text{O}_3$ /n-Si samples with different thicknesses of  $\text{Al}_2\text{O}_3$  as the interface oxide. The carrier lifetime is also compared to the values obtained with  $\text{Al}_2\text{O}_3$  on Si, as-deposited and after annealing.

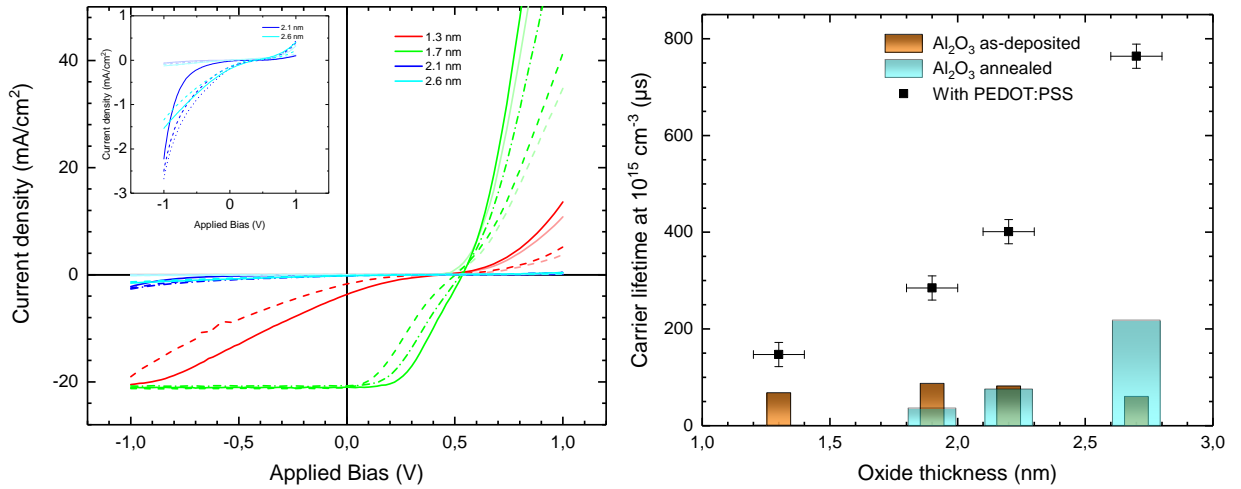


Figure 4.18: IV curves of solar cells with an interface  $\text{Al}_2\text{O}_3$  of different thicknesses (left) and minority carrier lifetime measured at an injection level of  $10^{15} \text{ cm}^{-3}$  (right). The dashed IV curves show the span in measured performance from the different isolated cells. The best performance is obtained with an oxide thickness of 1.7 nm while superior carrier lifetime is obtained for the thickest oxide.

Evidently, the sample with an  $\text{Al}_2\text{O}_3$  thickness of 1.7 nm displays quite good IV characteristics matched with an initial lifetime approaching 300  $\mu\text{s}$ . For a thicker oxide, the lifetime improves drastically, but there is close to no light response. The vast increase in carrier lifetime is probably due to an additional field-effect passivation which arises when the  $\text{Al}_2\text{O}_3$  is thick enough. Alas, the interface oxide is now thought to be too thick for tunnelling and is hence acting as a barrier, hindering the carrier flow across the junction.

Interestingly, the thinnest oxide of 1.3 nm is behaving worse than expected, with a severe s-shape causing reductions in  $V_{oc}$ ,  $J_{sc}$  and  $FF$ . Considering the excellent characteristics of cells with a thin native  $\text{SiO}_2$  as seen in figure 4.12, the thinnest  $\text{Al}_2\text{O}_3$  layer was expected to perform best. The somewhat lower lifetime ( $\sim 200 \mu\text{s}$ ) could have an influence on the observed performance. However, the lifetime is not so low as to have a detrimental effect on the performance. Another possibility is that some impurities may have been introduced somewhere in the process, leading to pin-holes in the PEDOT:PSS film or some other effect.

An important change that can be credited to the new interface is a higher  $V_{oc}$  of 535 mV for the champion cell at 1.7 nm oxide, probably arising from better passivation. Visual inspection during spin coating showed improved surface wettability with  $\text{Al}_2\text{O}_3$  compared to  $\text{SiO}_2$ . This could lead to a reduced number of surface defects, leading to better passivation and explaining the improved  $V_{oc}$ . However, the carrier lifetime for the  $\sim 1.7$  nm oxide is not better than the samples with native  $\text{SiO}_2$ . On the contrary, it is lower by at least 100  $\mu\text{s}$ . Thus, this improved  $V_{oc}$  is not directly linked to better passivation, but could still be a result of fewer defects at the interface.

Another effect which may be present is fixed charges in the oxide. This is an effect which could promote the passivation, and with it the carrier lifetime, and simultaneously present a barrier for charge extraction. Additionally, it would be more present in a

thicker oxide and could explain the changes in carrier lifetime after annealing of  $\text{Al}_2\text{O}_3$ . The mechanisms are, however, complicated and further experiments are needed in order to say anything conclusive.

Nam *et al.* [96] reported excellent IV characteristics with PEDOT:PSS/ $\text{Al}_2\text{O}_3$ /n-Si/n<sup>+</sup>BSF solar cells for  $\text{Al}_2\text{O}_3$  thicknesses of 1.73 and 2.3 nm, and curves of slight s-shapes with 2.88 nm. While the result with an oxide thickness of 1.7 nm supports our findings, the results with the two thicker oxides are in contrast to our results from both 2.1 and 2.6 nm.

Since the s-shape is credited to barriers at the PEDOT:PSS/n-Si interface, and mostly due to an oxide thickness that is too thick, this deviation could be due to uncertainties in the reported thicknesses, both our results and the results reported by Nam *et al.* However, there could also be differences in the density of the  $\text{Al}_2\text{O}_3$  due to slight variations in deposition parameters. Another possibility is that the BSF influences the onset of s-shapes, resulting in the larger span of possible oxide thicknesses reported by Nam *et al.*

A natural next step would be to fabricate new samples with  $\text{Al}_2\text{O}_3$  thicknesses in the range 1.3–2.0 nm and apply backside passivation, both to validate these results, obtain an optimised  $\text{Al}_2\text{O}_3$  thickness and explore the effect of backside passivation on s-shapes.

### Stability

The degradation in cell performance and carrier lifetime is shown in figure 4.19. For the two thinnest oxides, a steady degradation is observed with increasing storage time. Similarly to the previously seen samples, degradation is mostly affecting the fill factor. After 29 days for the 1.7 nm thick oxide, however, a more pronounced s-shape occurs (yellow curves) which causes a decrease in  $J_{sc}$  as well. Note that the s-shape is more pronounced for the measurement after 29 days than the following measurements at day 44, 68 and 86. This is probably due to some deviation in ambient temperature or probe contact, as it seems unlikely that the s-shape should get less pronounced again.

Due to a lack of space, these samples were not stored in the desiccator. If they were, the degradation would most likely be less severe and proceed at a slower pace.

There is also a substantial degradation in carrier lifetime with values below 100  $\mu\text{s}$  for all but the thickest oxide after 69 days of storage. This is rather expected since the wafers were stored in ambient conditions. The thickest oxide seems to retain a higher lifetime of  $\sim 250 \mu\text{s}$ .

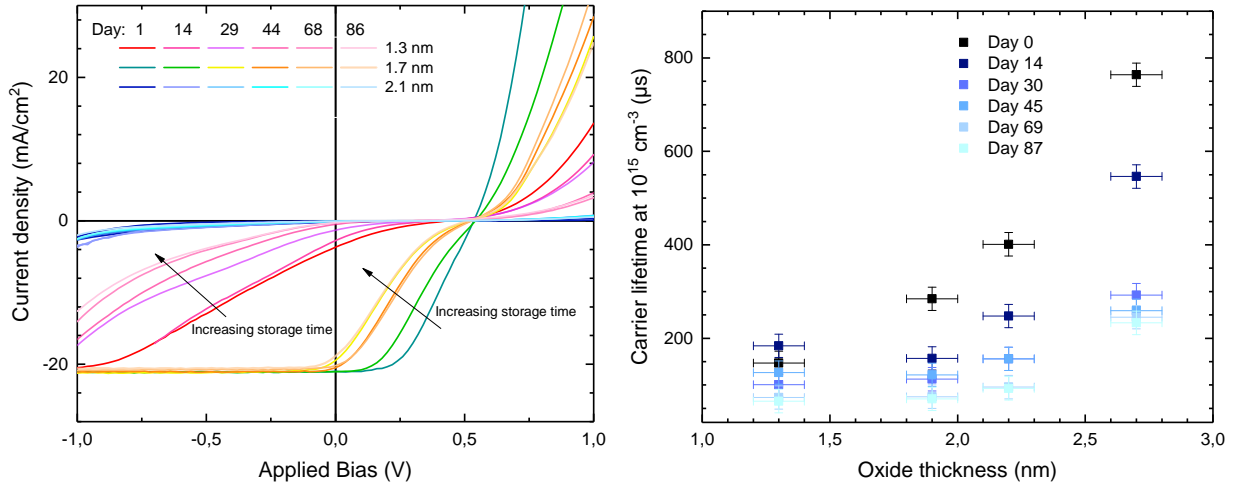


Figure 4.19: IV curves showing degradation (left) and degradation in carrier lifetime (right) for PEDOT:PSS/ $\text{Al}_2\text{O}_3$ / $n$ -Si solar cells. There is quite a severe degradation in both solar cell performance and carrier lifetime. This is not very surprising as the wafers were stored in ambient conditions. The IV curves also show the onset of more severe s-shapes.

Compared to the samples with a thin regrown native oxide described in section 4.4.1, the degradation appears similar for the different interfaces. This seems reasonable considering that the ultra-thin interface oxide in the range of 0.26–2 nm is unlikely to have a major effect on the degradation.

The reason for an increased s-shape for 1.7 nm after 29 days and onwards may be due to some diffusion of oxygen or water through  $\text{Al}_2\text{O}_3$ , enabling the formation of a thin  $\text{SiO}_2$  between Si and  $\text{Al}_2\text{O}_3$ . This would lead to a slightly thicker tunnelling barrier and a possibly negative effect between  $\text{SiO}_2$  and  $\text{Al}_2\text{O}_3$ . Additionally, the aforementioned absorption of water in the PEDOT:PSS layer is also likely to occur, causing swelling of PSS species and resulting separation of conductive PEDOT grains leading to higher series resistance.

As apparent from the severe change in performance from 1.7 to 2.1 nm, there is a fine line between an appropriately thick tunnelling barrier (1.7 nm) and a barrier that is too thick to enable tunnelling (2.1 nm). Therefore, it seems likely that the optimal oxide thickness is somewhere in the range 1.3–2.0 nm.

## Summary

Aluminium oxide is also an excellent candidate for the interface between PEDOT:PSS and Si. While further work is required to determine the optimal thickness and study the degradation at reduced humidity, the improved  $V_{oc}$  shows good potential for PEDOT:PSS/ $\text{Al}_2\text{O}_3$ / $n$ -Si solar cells. Regarding cost efficiency, however,  $\text{Al}_2\text{O}_3$  is not a better option than native  $\text{SiO}_2$ . Moreover, the results here clearly shows the important trade-off between good passivation (thick oxide) and sufficiently low tunnelling barrier for reduced series resistance (thin oxide).

### 4.4.3 Amorphous silicon

Another interface known for excellent chemical passivation of the Si surface is amorphous silicon. An interface of a-Si:H defies the purpose of keeping these cells as low-cost as possible due to the need for the vacuum process PECVD, but is still an interesting case study. The exact thicknesses of the two different a-Si:H layers are not known, but both are expected to be on the order of a few nm. Regardless of the actual thickness, the layer formed by ramp + 15 s is definitely slightly thicker than the layer formed by only ramp. "Ramp" here refers to the ramp-up where the wafers are introduced to the reaction zone, and the effect is increased rapidly to the process setpoint. While most of the deposition occurs after ramp-up, some a-Si:H is expected to be deposited during this process. The resulting IV curves are shown in figure 4.20.

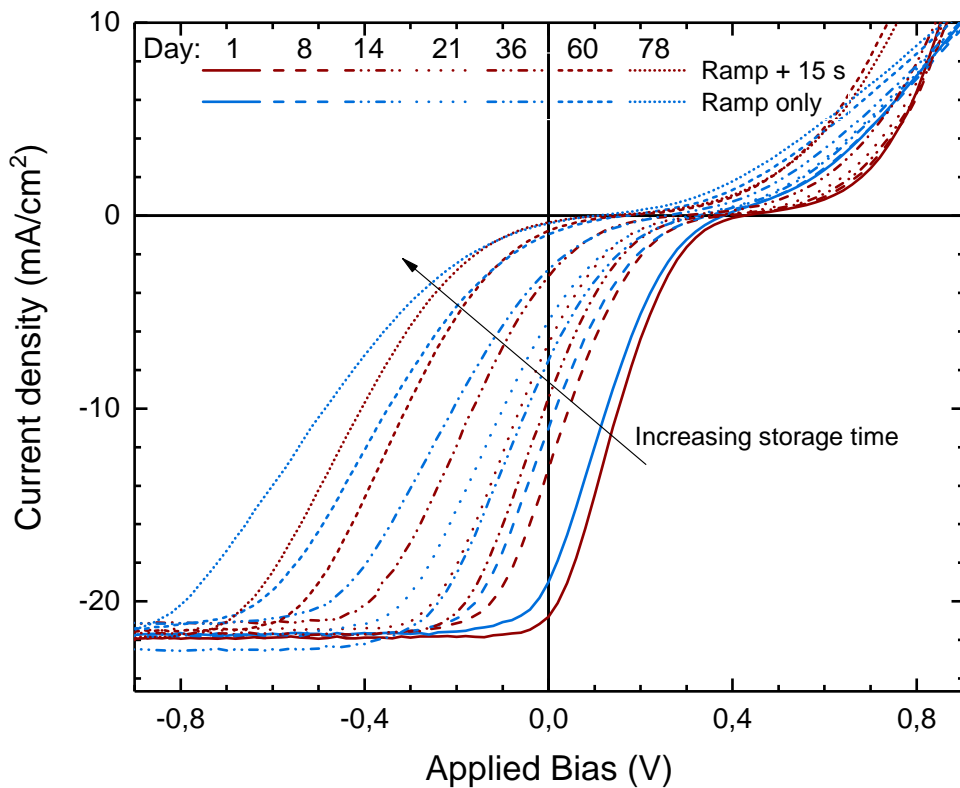


Figure 4.20: IV curves showing the performance of PEDOT:PSS/a-Si:H/n-Si solar cells, both initially and after storage. There is a severe s-shape limiting the performance, with slightly better values for the thicker a-Si layer. There is also severe degradation with increasing storage time, shifting the onset of the s-shapes to higher reverse bias.

The original curves exhibit s-shaped behaviour, has quite good  $J_{sc}$  of 19 and 20 mA, slightly hindered by the s-shape, and poor  $V_{oc}$  of 380 and 425 mV. The top of the s-shape is more pronounced than seen for previous samples and is almost flattened out between 400 and 550 mV. As a consequence, the  $V_{oc}$  may be severely affected by the s-shape.

From the results with native  $\text{SiO}_2$  and  $\text{Al}_2\text{O}_3$ , the s-shape is mostly credited to an interface barrier caused by an interface oxide that is too thick. If this applies to these a-Si:H samples as well, we could reason that the a-Si:H layers are too thick, and a decrease

in their thickness could remove the s-behaviour and give a cell with better performance. Comparing the two different thicknesses, however, the cell with the thickest layer (ramp + 15 s, red curve) exhibits the best performance and seems to have a slightly less pronounced s-shape. This contradicts the assumption of the a-Si:H layer being too thick and instead suggests that a thicker layer could remove the s-shape and provide a better solar cell.

Regardless of the origin of the s-shape, it is apparent that the s-shapes become even more pronounced and "takes off" at a higher and higher reverse bias with increased storage time, resulting in a continuous decrease in performance.

The corresponding lifetimes of these cells are shown in figure 4.21 and shows a surprising trend. Note that the lifetime samples were fabricated one day before the solar cells, and the degradation data is obtained after 9, 15 and 22 days, and so forth. Nevertheless, the data should be comparable.

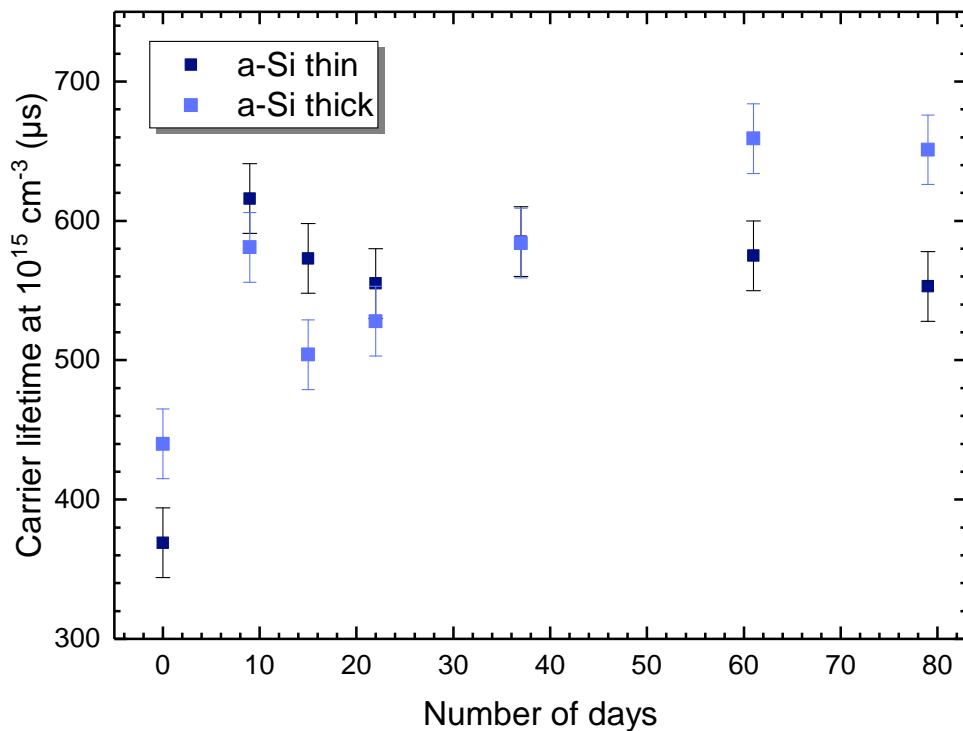


Figure 4.21: Carrier lifetime for the two samples with a-Si:H at the interface between PEDOT:PSS and n-Si. There is an increase in carrier lifetime after storage, followed by little to no degradation. Contrary to all the other samples, the passivation does not display any severe degradation, even after storing in ambient conditions.

Interestingly, an initially high lifetime around 400  $\mu\text{s}$  increases after nine days to  $\sim 600 \mu\text{s}$  and shows little to no degradation. Particularly the sample with the thickest a-Si layer appears to have a continuous increase in passivation after storage, in stark contrast to the other samples.

This could be due to an additional passivation by the amorphous silicon, possibly with PEDOT:PSS acting as a stabilising capping layer. Thence, the lifetime may remain at high values despite degradation of PEDOT:PSS. Unfortunately, this increase in carrier lifetime is not reflected in the IV curves. It would, however, be interesting to see how a

solar cell with an even thicker a-Si layer performs.

One possible reason for this increase in passivation is oxidation of the amorphous silicon. a-Si:H is known to contain a high concentration of hydrogen. Oxidation of amorphous silicon may thus lead to a structure where Si is randomly passivated by both oxygen and hydrogen, leading to a superior and stable passivation, but simultaneously an increasing barrier for tunnelling.

## Summary

*Amorphous silicon leads to excellent and stable passivation, which is, unfortunately, not reflected in solar cell performance. S-shaped IV curves show a detrimental effect on both  $V_{oc}$ ,  $J_{sc}$  and  $FF$ , particularly with increased storage in ambient. Experiments with an even thicker a-Si layer and humidity-free storage could be interesting for further work.*

### 4.4.4 Chemically grown silicon dioxide

Nitric acid oxidation of Si has been shown by Kobayashi *et al.* to provide an ultrathin, highly reproducible  $\text{SiO}_2$  layer of 0.7 and 1.4 nm for 10 min oxidation at room temperature and 121°C, respectively [29]. Figure 4.22 shows the resulting IV curves and measured carrier lifetime from samples with interface oxides produced in the same manner.

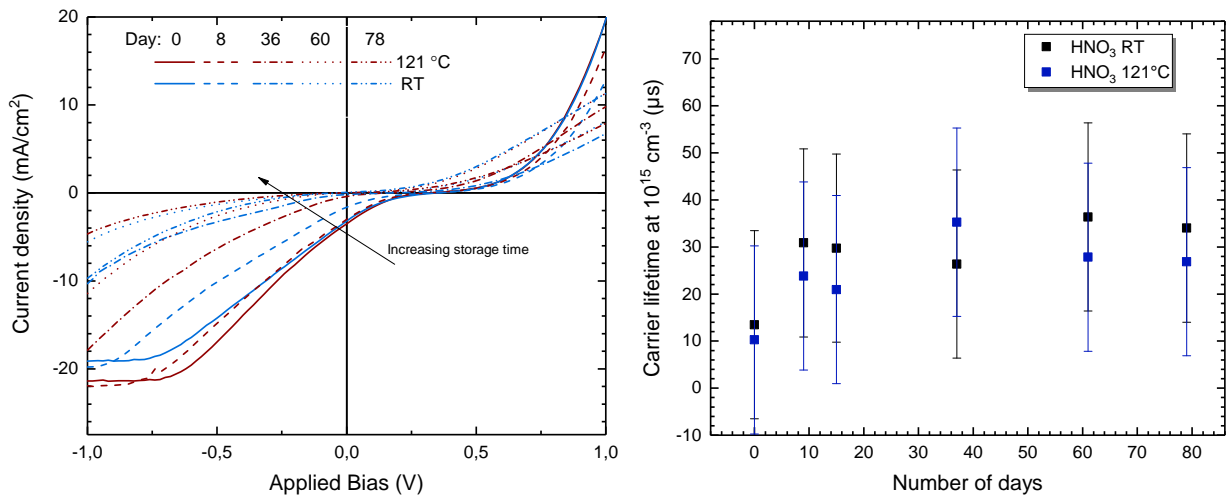


Figure 4.22: IV curves (left) and minority carrier lifetime (right) showing initial performance and stability of PEDOT:PSS/ $\text{SiO}_2$ /n-Si solar cells with  $\text{SiO}_2$  chemically grown by  $\text{HNO}_3$ . All the curves display broad s-shapes and severe degradation. The carrier lifetimes are inferior with values of 10–35  $\mu\text{s}$  both initially and after storage.

These curves display broad s-shapes, resulting in abysmal performance. This is a little surprising, especially for the sample oxidised at room temperature, since this is expected to have an oxide thickness  $\sim 0.7$  nm. This is similar to what is expected for the native oxide grown for seven days ( $\sim 0.67$  nm after Morita *et al.* [27]) with good initial performance as seen in figure 4.12. This suggests one of the following:

Either, the oxide thicknesses differ from the ones reported by Kobayashi and Morita. This could originate from differences in room temperature and relative humidity or some experimental errors. To the best of the author's knowledge, the procedures and conditions used in this work were highly comparable to the referenced ones, including the temperature and relative humidity in the lab, the resistivity of the wafers and chemicals used. A large deviation in oxide thicknesses therefore seems unlikely.

Conversely, the quality of the different oxide layers may differ. Due to the different oxidising conditions, the  $\text{SiO}_2$  layer formed by  $\text{HNO}_3$  may be denser than the one formed by  $\text{O}_2$  at ambient conditions, making it harder for carriers to tunnel through the former. The oxidising process may also lead to the formation of more defects at the interface.

As also seen by figure 4.22, the lifetimes of these samples were very poor, with values  $\sim 10\text{--}35\ \mu\text{s}$  for both samples. This supports the notion of a worse interface between PEDOT:PSS and Si, possibly due to the formation of defects during or after the oxidation.

### Summary

*Chemically grown  $\text{SiO}_2$  at the interface resulted in inferior solar cell performance and carrier lifetimes. The culprit is suspected to be the formation of a denser oxide layer, the formation of more defects at the interface, or a combination of both.*

#### 4.4.5 Summary of the various interface layers

The overall best interface in this study is clearly a freshly grown native  $\text{SiO}_2$ . The solar cells with this interface have shown superior performance, excellent surface passivation and relatively good stability. Moreover, the use of a native oxide retains the low-cost aspect.

The other promising interface in this work is  $\text{Al}_2\text{O}_3$ . The optimised oxide thickness is believed to be somewhere between 1.3–2.0 nm, and may ultimately provide better  $V_{oc}$  than  $\text{SiO}_2$ . However, further work is required with an optimised oxide thickness, ideally together with back-surface passivation and encapsulation.

Original native oxide, chemically grown  $\text{SiO}_2$  and a-Si:H all provide challenges regarding limited performance due to s-shapes. Of these, a-Si:H may show major improvements with an optimised a-Si:H thickness and back-surface passivation if pursued further.

## 4.5 The PEDOT:PSS/Si solar cell

Overall, the best cell was obtained with a freshly grown native  $\text{SiO}_2$  for 45 min, closely followed by the other oxides with growth times in the range 15–60 min. The solar cell characteristics for the champion cell are summarised in table 4.3.

Compared to previous work done at IFE, this advance is credited to the optimised process of composition and spin coating, enabling fabrication on HF-etched samples. This has, in turn, led to a more favourable interface as evidenced by the removal of any s-shape in the IV curve and even better front-side passivation.

Table 4.3: Values obtained for the champion solar cell of PEDOT:PSS/SiO<sub>2</sub>/n-Si with an oxide growth time of 45 min. Both measured and theoretical values with 5% shading are shown. Front-side SRV obtained from the symmetrically passivated sample by QSSPC is also shown.

	$J_{sc}$ [mA/cm <sup>2</sup> ]	$V_{oc}$ [mV]	FF [%]	$\eta$ [%]	$S_{front}$ [cm/s]
Measured	21.5	460.0	73.7	7.3	30.8
Theoretical with 5% shading	28.4	467.2	73.7	9.8	-

The obtained  $J_{sc}$ ,  $V_{oc}$  and resulting  $\eta$  are low compared to the best values reported in the literature, mostly credited to recombination at the rear surface, series resistance and low absorption. However, by implementing a few additional steps to the procedure from this work, our solar cells should be able to approach the best reported values.

#### 4.5.1 Realising the full potential

The low  $V_{oc}$  is considered as a bottleneck for further improvements in cell performance, and major advances could be made by employing sufficient surface passivation on the backside and simultaneously obtaining a better back contact. This is supported by simulations performed by He *et al.* [51] showing the effect on  $V_{oc}$  by  $S_{rear}$  and  $S_{front}$ , shown in figure 4.23.

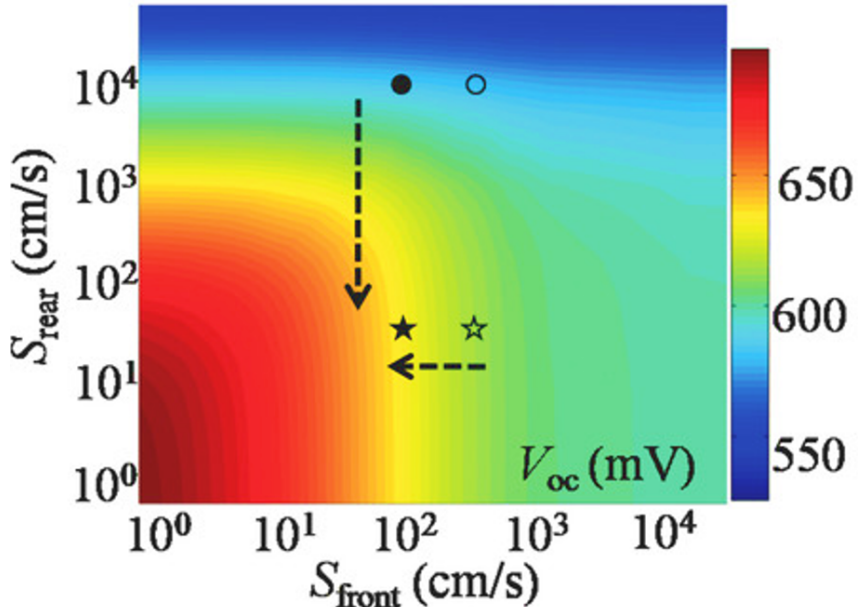


Figure 4.23: Simulated effect of both front- and rear SRVs on  $V_{oc}$ . The crucial need for sufficient passivation on both sides is evident. From [51].

Our unpassivated backside is expected to have  $S_{rear} > 10^4$  cm/s which severely limits the open-circuit voltage. With  $S_{front}$  of  $\sim 30$ – $80$  cm/s, even after 100 days of storage, the front-side passivation is evidently sufficient for excellent  $V_{oc}$  values. However, a reduction

in  $S_{rear}$  is crucial to increase  $V_{oc}$ . Furthermore, an increased  $S_{rear}$  will lead to improved  $J_{sc}$  as demonstrated by Yang *et al.* [101].

The doping of the n-Si substrate is also affecting the open-circuit voltage since higher doping would result in a higher Fermi level which in turn affects the built-in voltage with PEDOT:PSS and gives rise to higher  $V_{oc}$ . A majority of the high efficiencies mentioned in section 2.6 were obtained with wafers with  $\rho = 0.005 - 0.1 \Omega\text{cm}$  ( $8 \times 10^{16} - 1 \times 10^{19} \text{ cm}^{-3}$ ). While there is an important trade-off between recombination (for highly doped wafers) and  $V_{oc}$ , slightly higher doped wafers than the ones used in this work are expected to yield better performance.

The potential of high  $V_{oc}$  of our PEDOT:PSS/n-Si solar cells is further supported by looking at the implied  $V_{oc}$  from excess carrier density, as described in section 3.2.5. Table 4.4 shows the implied  $V_{oc}$  for the symmetrically passivated PEDOT:PSS/SiO<sub>2</sub>/n-Si samples with different oxide growth times. Note that this would be an upper limit for the ideal case with equally good passivation of the backside as on the front.

Table 4.4: Implied  $V_{oc}$  calculated from excess carrier density measured by PLI. This represents an upper limit for the  $V_{oc}$  with equally good passivation on the backside as currently on the front.

Oxide growth time [min]	15	30	45	60	180	300	1440	10080
Implied $V_{oc}$ [mV]	685	683	682	685	682	678	683	686

While these results show that the PEDOT:PSS/n-Si solar cells have the potential for high  $V_{oc}$  and further that the  $V_{oc}$  is expected to increase by reducing the rear-side surface recombination, it does not explain values as low as 460 mV as obtained by our champion cell. Based on figure 4.23, values approaching 550 mV should still be possible with poor  $S_{rear}$ .

According to Erickson *et al.* [113] and He *et al.* [14] Fermi level pinning may occur due to a high density of interfacial states and result in  $V_{oc}$  of only 0.4–0.5 V. Fermi level pinning should, however, also limit the  $V_{bi}$  to approximately  $E_g/2$  which would be 0.56 V. This contradicts our measured built-in voltages of  $\sim 0.67$  V as shown in figure 4.17. Thus, the poor  $V_{oc}$  may simply be a result of lacking surface passivation and an unfavourable back contact, both of which can be drastically improved by applying suitable back-surface passivation, for instance, an n<sup>+</sup> diffusion or siloxane oligomers, as shown by Yoon *et al.* [72].

Another possible reason for the low  $V_{oc}$  is fixed charges in the oxide, as briefly discussed for the solar cells with Al<sub>2</sub>O<sub>3</sub> at the interface in section 4.4.2. This could lead to a Coulomb barrier which in turn restricts  $V_{oc}$ . This effect should, however, increase with a thicker oxide layer since the amount of fixed charges should increase with oxide thickness. Since the three solar cells with thickest oxides appear to have the highest open-circuit voltages, this effect alone is not sufficient to explain both the low  $V_{oc}$  and the trend. Nevertheless, it may be a contribution to the overall low  $V_{oc}$ .

Further experiments with similar interface treatments and the addition of a suitable back-surface passivation will give invaluable insight to these mechanisms and is thus highly recommended.

Another procedure which should be implemented is texturing of the surface in order to increase the absorption of light and thus increase  $J_{sc}$ . As discussed in section 2.6, a wide range of nanostructures have been tested by several authors. However, the lack of conformal coating between PEDOT:PSS and Si have mostly resulted in inadequate performance. There are, however, several promising advances. The combination of anisotropic etching to create a pyramidal surface and isotropic etching to further curve the valleys is reported to work very well, enabling conformal contact due to the additional isotropic etch [72], [74].

Alternatively, the use of a capping layer, such as DEP provides a means to mechanically aid the contact between PEDOT:PSS and textured Si without the need for an isotropic etch [82]. DEP, being a water-insoluble phthalic acid ester, may also prove useful in reducing the humidity reaching PEDOT:PSS and the interface and thereby increase the stability.

Adopting one of these procedures will also provide room for further improvement through the incorporation of nanostructures at the surface or in the PEDOT:PSS solution. However, care should be taken not to drastically increase the cost, complexity, or both.

# Concluding remarks

## 5.1 Summary

This work has resulted in a procedure for consistently making PEDOT:PSS/n-Si solar cells with efficiencies approaching 10 % and front-side SRVs around 30 cm/s at The Solar Cell Laboratory at IFE.

PEDOT:PSS has shown excellent passivating properties on n-Si, particularly with a thin regrown interfacial SiO<sub>2</sub> or a thin a-Si:H between PEDOT:PSS and Si. The solution-based nature of PEDOT:PSS enables homogeneity over the wafer after spin coating, provided optimised spin speeds and amount of surfactant in the solution. This was found to be 1000 rpm followed by 1500 rpm and 1% Triton X-100, respectively.

The crucial role of a suitable interfacial layer is thoroughly documented. A SiO<sub>2</sub> layer regrown for 45 minutes provided the highest performing solar cell in this study, with a measured efficiency of 7.3% (9.8% by assuming only 5 % shading). Moreover, the entire range of native oxide growth times resulted in solar cells with similar efficiencies, and superior long-term stability for the thinnest oxides. The critical trade-off between tunnelling and passivation is evidenced with Al<sub>2</sub>O<sub>3</sub> at the interface; here, a thin layer is lacking good passivation and a thick layer results in a tunnelling barrier which is too high. The optimal Al<sub>2</sub>O<sub>3</sub> thickness is predicted to be between 1.3 and 2.0 nm.

Superior passivation with ensuing stability is observed for samples with a thin amorphous silicon layer at the interface. This is, however, not reflected in the solar cell performance. Moreover, the adverse performance of chemically grown SiO<sub>2</sub> has shown the need for controlling both the thickness and density of the interfacial layer.

There are some challenges regarding the stability. By exposure to ambient conditions, both the passivation and electrical solar cell performance degrades drastically within weeks, credited to swelling of the polymer and further oxidation of the silicon surface, both leading to higher series resistance. However, this work has shown that the reduction of ambient humidity alleviates the degradation and shows significant improvements on the long-term stability. Furthermore, the total absence of water is predicted to remove the stability issues regarding swelling and further oxidation altogether. Storing below room temperature has also proven to enhance the stability.

To conclude, this work has further developed both the process for fabrication and the understanding of the crucial PEDOT:PSS/n-Si interface. Furthermore, the great potential of these cells as low cost, high-efficiency solar cells is demonstrated.

## 5.2 Further work

Several highly interesting and pivotal aspects for further work arise from this work.

As discussed in section 4.5.1, sufficient back-surface passivation needs to be implemented. As an immediate next step, a simple phosphorous diffusion should be implemented to validate the effect. However, this requires high temperatures and adds substantial cost to the process. Thus, to fully embrace the low-cost aspect, work should be conducted to test siloxane oligomers, as shown by Yoon *et al.* [72], or other solution-based low-cost processes. The potential of siloxane oligomers to work as both front- and back-side passivation is very interesting as it could reduce the complexity of fabrication and should be explored further.

Another step in increasing the efficiency of these solar cells is absorption enhancement through texturing. Here, the combination of anisotropic etching to make a pyramidal structure and subsequent isotropic etching to curve the valleys stands out as a very promising approach.

The PEDOT:PSS/Al<sub>2</sub>O<sub>3</sub>/n-Si solar cell should also be explored further. By fabricating more cells with several different oxide thicknesses between 1.3 and 2.0 nm, the optimal thickness can be determined and the cell might show superior performance to the PEDOT:PSS/SiO<sub>2</sub>/n-Si solar cell.

It would also be interesting to check the effect of a thicker a-Si:H layer at the interface. Due to the cost, however, this would be more of a scientific curiosity than a potential replacement for SiO<sub>2</sub> at the interface.

Finding a suitable encapsulant for PEDOT:PSS/Si cells is also crucial. This work has shown the critical need for keeping the PEDOT:PSS/Si solar cell in a humid-free environment and further shown that the stability is highly enhanced by storage in a low-humid environment as provided by a desiccator. It is thus important to both find a suitable encapsulant and perform similar stability tests as done in this thesis, only with the solar cell exposed to real operating conditions.

Lastly, quantum efficiency measurement could provide valuable insight into the optical losses, especially after applying a sufficient back-surface passivation, and help pave the way for even higher efficiencies.

# Bibliography

- [1] United Nations, Department of Economic and Social Affairs, and Population Division, *World population prospects Highlights, 2019 revision*. 2019.
- [2] International Energy Agency, “World Energy Outlook 2019,” *World Energy Outlook*, 2019, OECD Publishing, Paris.
- [3] K. Haustein, M. R. Allen, P. M. Forster, F. E. L. Otto, D. M. Mitchell, H. D. Matthews, and D. J. Frame, “A real-time Global Warming Index,” *Scientific Reports*, vol. 7, no. 1, Dec. 2017.
- [4] “Transforming Our World: The 2030 Agenda for Sustainable Development,” in *A New Era in Global Health*, W. Rosa, Ed., New York, NY: Springer Publishing Company, Jun. 2017.
- [5] Fraunhofer ISE, “Photovoltaics Report,” Nov. 2019.
- [6] S. Avasthi, S. Lee, Y.-L. Loo, and J. C. Sturm, “Role of Majority and Minority Carrier Barriers Silicon/Organic Hybrid Heterojunction Solar Cells,” en, *Advanced Materials*, vol. 23, no. 48, pp. 5762–5766, Dec. 2011.
- [7] Y. H. Kim, C. Sachse, M. L. Machala, C. May, L. Müller-Meskamp, and K. Leo, “Highly Conductive PEDOT:PSS Electrode with Optimized Solvent and Thermal Post-Treatment for ITO-Free Organic Solar Cells,” en, *Advanced Functional Materials*, vol. 21, no. 6, pp. 1076–1081, Feb. 2011.
- [8] L. He, C. Jiang, H. Wang, D. Lai, and Rusli, “High efficiency planar Si/organic heterojunction hybrid solar cells,” en, *Applied Physics Letters*, vol. 100, no. 7, p. 073 503, Feb. 2012.
- [9] Y. Liu, J. Zhao, Z. Li, C. Mu, W. Ma, H. Hu, K. Jiang, H. Lin, H. Ade, and H. Yan, “Aggregation and morphology control enables multiple cases of high-efficiency polymer solar cells,” en, *Nature Communications*, vol. 5, no. 1, p. 5293, Dec. 2014.
- [10] J. Schmidt, V. Titova, and D. Zielke, “Organic-silicon heterojunction solar cells: Open-circuit voltage potential and stability,” en, *Applied Physics Letters*, vol. 103, no. 18, p. 183 901, Oct. 2013.
- [11] D. Zielke, A. Pazidis, F. Werner, and J. Schmidt, “Organic-silicon heterojunction solar cells on n-type silicon wafers: The BackPEDOT concept,” en, *Solar Energy Materials and Solar Cells*, vol. 131, pp. 110–116, Dec. 2014.
- [12] D. Zielke, C. Niehaves, W. Lövenich, A. Elschner, M. Hörteis, and J. Schmidt, “Organic-silicon Solar Cells Exceeding 20% Efficiency,” en, *Energy Procedia*, vol. 77, pp. 331–339, Aug. 2015.

- [13] A. Kumar, M. Bieri, T. Reindl, and A. G. Aberle, “Economic Viability Analysis of Silicon Solar Cell Manufacturing: Al-BSF versus PERC,” en, *Energy Procedia*, vol. 130, pp. 43–49, Sep. 2017.
- [14] W. W. He, K. J. Wu, K. Wang, T. F. Shi, L. Wu, S. X. Li, D. Y. Teng, and C. H. Ye, “Towards stable silicon nanoarray hybrid solar cells,” en, *Scientific Reports*, vol. 4, no. 1, p. 3715, May 2015.
- [15] S.-S. Yoon and D.-Y. Khang, “Ag nanowire/PEDOT:PSS bilayer transparent electrode for high performance Si-PEDOT:PSS hybrid solar cells,” en, *Journal of Physics and Chemistry of Solids*, vol. 129, pp. 128–132, Jun. 2019.
- [16] A. Reinders, P. Verlinden, W. v. Sark, and A. Freundlich, Eds., *Photovoltaic solar energy: from fundamentals to applications*. Chichester, West Sussex, United Kingdom; Hoboken, NJ: John Wiley & Sons Ltd, 2017.
- [17] J. Nelson, *The physics of solar cells*. London: River Edge, NJ: Imperial College Press; Distributed by World Scientific Pub. Co, 2003.
- [18] A. Smets, K. Jäger, O. Isabella, R. Swaaij, van, and M. Zeman, *Solar energy: the physics and engineering of photovoltaic conversion technologies and systems*, English. UIT, 2016.
- [19] B. G. Streetman and S. K. Banerjee, *Solid state electronic devices*, eng, 7. ed., Global ed, ser. Always learning. Boston, Mass.: Pearson, 2016.
- [20] D. K. Schroder, *Semiconductor Material and Device Characterization*, 3rd ed. 2006.
- [21] R. Saive, “S-Shaped Current–Voltage Characteristics in Solar Cells: A Review,” *IEEE Journal of Photovoltaics*, vol. 9, no. 6, pp. 1477–1484, Nov. 2019.
- [22] W. Tress, A. Petrich, M. Hummert, M. Hein, K. Leo, and M. Riede, “Imbalanced mobilities causing S-shaped IV curves in planar heterojunction organic solar cells,” en, *Applied Physics Letters*, vol. 98, no. 6, p. 063301, Feb. 2011.
- [23] J. Wagner, M. Gruber, A. Wilke, Y. Tanaka, K. Topczak, A. Steindamm, U. Hörmann, A. Opitz, Y. Nakayama, H. Ishii, J. Pflaum, N. Koch, and W. Brütting, “Identification of different origins for s-shaped current voltage characteristics in planar heterojunction organic solar cells,” en, *Journal of Applied Physics*, vol. 111, no. 5, p. 054509, Mar. 2012, ISSN: 0021-8979, 1089-7550.
- [24] A. Kumar, S. Sista, and Y. Yang, “Dipole induced anomalous S-shape I-V curves in polymer solar cells,” en, *Journal of Applied Physics*, vol. 105, no. 9, p. 094512, May 2009.
- [25] W. Tress and O. Inganäs, “Simple experimental test to distinguish extraction and injection barriers at the electrodes of (organic) solar cells with S-shaped current–voltage characteristics,” en, *Solar Energy Materials and Solar Cells*, vol. 117, pp. 599–603, Oct. 2013.

- [26] S. A. Campbell, *Fabrication engineering at the micro- and nanoscale*, Fourth edition, ser. The Oxford series in electrical and computer engineering. New York: Oxford University Press, 2013.
- [27] M. Morita, T. Ohmi, E. Hasegawa, M. Kawakami, and M. Ohwada, “Growth of native oxide on a silicon surface,” en, *Journal of Applied Physics*, vol. 68, no. 3, pp. 1272–1281, Aug. 1990.
- [28] S. I. Raider, “Oxide Growth on Etched Silicon in Air at Room Temperature,” en, *Journal of The Electrochemical Society*, vol. 122, no. 3, p. 413, 1975.
- [29] H. Kobayashi Asuha, O. Maida, M. Takahashi, and H. Iwasa, “Nitric acid oxidation of Si to form ultrathin silicon dioxide layers with a low leakage current density,” en, *Journal of Applied Physics*, vol. 94, no. 11, pp. 7328–7335, Dec. 2003.
- [30] H. Haug, “New methods for investigation of surface passivation layers for crystalline silicon solar cells,” PhD thesis, UiO, 2014.
- [31] W. Shockley and W. T. Read, “Statistics of the Recombinations of Holes and Electrons,” en, *Physical Review*, vol. 87, no. 5, pp. 835–842, Sep. 1952.
- [32] R. N. Hall, “Electron-Hole Recombination in Germanium,” en, *Physical Review*, vol. 87, no. 2, pp. 387–387, Jul. 1952.
- [33] W. Tress, *Organic solar cells: theory, experiment, and device simulation*, eng, ser. Springer series in materials science volume 208. Springer, 2014.
- [34] K. Leo, Ed., *Elementary processes in organic photovoltaics*, eng, ser. Advances in polymer science 272. Cham: Springer International Publishing, 2017.
- [35] X. Fan, M. Zhang, X. Wang, F. Yang, and X. Meng, “Recent progress in organic-inorganic hybrid solar cells,” en, *Journal of Materials Chemistry A*, vol. 1, no. 31, p. 8694, 2013.
- [36] M. Pietsch, S. Jäckle, and S. Christiansen, “Interface investigation of planar hybrid n-Si/PEDOT:PSS solar cells with open circuit voltages up to 645 mV and efficiencies of 12.6 %,” en, *Applied Physics A*, vol. 115, no. 4, pp. 1109–1113, Jun. 2014.
- [37] J. P. Thomas and K. T. Leung, “Mixed co-solvent engineering of PEDOT:PSS to enhance its conductivity and hybrid solar cell properties,” en, *Journal of Materials Chemistry A*, vol. 4, no. 44, pp. 17 537–17 542, 2016.
- [38] C. K. Chiang, C. R. Fincher, Y. W. Park, A. J. Heeger, H. Shirakawa, E. J. Louis, S. C. Gau, and A. G. MacDiarmid, “Electrical Conductivity in Doped Polyacetylene,” en, *Physical Review Letters*, vol. 39, no. 17, pp. 1098–1101, Oct. 1977.
- [39] S. Jäckle, M. Mattiza, M. Liebhaber, G. Brönstrup, M. Rommel, K. Lips, and S. Christiansen, “Junction formation and current transport mechanisms in hybrid n-Si/PEDOT:PSS solar cells,” en, *Scientific Reports*, vol. 5, no. 1, p. 13 008, Oct. 2015.

- [40] E. L. Williams, G. E. Jabbour, Q. Wang, S. E. Shaheen, D. S. Ginley, and E. A. Schiff, "Conducting polymer and hydrogenated amorphous silicon hybrid solar cells," en, *Applied Physics Letters*, vol. 87, no. 22, p. 223 504, Nov. 2005.
- [41] K.-Y. Ho, C.-K. Li, H.-J. Syu, Y. Lai, C.-F. Lin, and Y.-R. Wu, "Analysis of the PEDOT:PSS/Si nanowire hybrid solar cell with a tail state model," en, *Journal of Applied Physics*, vol. 120, no. 21, p. 215 501, Dec. 2016.
- [42] E. Vitoratos, S. Sakkopoulos, E. Dalas, N. Paliatsas, D. Karageorgopoulos, F. Petraki, S. Kennou, and S. Choulis, "Thermal degradation mechanisms of PEDOT:PSS," en, *Organic Electronics*, vol. 10, no. 1, pp. 61–66, Feb. 2009.
- [43] A. Elschner, "The spectral sensitivity of PEDOT:PSS films," en, *Solar Energy Materials and Solar Cells*, vol. 95, no. 5, pp. 1333–1338, May 2011.
- [44] D. Wang, J. Zhu, L. Ding, P. Gao, X. Pan, J. Sheng, and J. Ye, "Interface electric properties of Si/organic hybrid solar cells using impedance spectroscopy analysis," en, *Japanese Journal of Applied Physics*, vol. 55, no. 5, p. 056 601, May 2016.
- [45] J. P. Thomas, L. Zhao, M. Abd-Ellah, N. F. Heinig, and K. T. Leung, "Interfacial Micropore Defect Formation in PEDOT:PSS-Si Hybrid Solar Cells Probed by TOF-SIMS 3d Chemical Imaging," en, *Analytical Chemistry*, vol. 85, no. 14, pp. 6840–6845, Jul. 2013.
- [46] S. Jäckle, M. Liebhaber, J. Niederhausen, M. Büchele, R. Félix, R. G. Wilks, M. Bär, K. Lips, and S. Christiansen, "Unveiling the Hybrid n-Si/PEDOT:PSS Interface," en, *ACS Applied Materials & Interfaces*, vol. 8, no. 13, pp. 8841–8848, Apr. 2016.
- [47] L. Zhang, Z. Wang, H. Lin, W. Wang, J. Wang, H. Zhang, J. Sheng, S. Wu, P. Gao, J. Ye, and T. Yu, "Thickness-modulated passivation properties of PEDOT:PSS layers over crystalline silicon wafers in back junction organic/silicon solar cells," en, *Nanotechnology*, vol. 30, no. 19, p. 195 401, May 2019.
- [48] S. Maldonado, K. E. Plass, D. Knapp, and N. S. Lewis, "Electrical Properties of Junctions between Hg and Si(111) Surfaces Functionalized with Short-Chain Alkyls," en, *The Journal of Physical Chemistry C*, vol. 111, no. 48, pp. 17 690–17 699, Dec. 2007.
- [49] R. Hunger, R. Fritsche, B. Jaeckel, W. Jaegermann, L. J. Webb, and N. S. Lewis, "Chemical and electronic characterization of methyl-terminated Si(111) surfaces by high-resolution synchrotron photoelectron spectroscopy," *Physical Review B*, vol. 72, no. 4, p. 045 317, Jul. 2005, Publisher: American Physical Society.
- [50] F. Zhang, B. Sun, T. Song, X. Zhu, and S. Lee, "Air Stable, Efficient Hybrid Photovoltaic Devices Based on Poly(3-hexylthiophene) and Silicon Nanostructures," en, *Chemistry of Materials*, vol. 23, no. 8, pp. 2084–2090, Apr. 2011.

- [51] J. He, P. Gao, Z. Yang, J. Yu, W. Yu, Y. Zhang, J. Sheng, J. Ye, J. C. Amine, and Y. Cui, "Silicon/Organic Hybrid Solar Cells with 16.2% Efficiency and Improved Stability by Formation of Conformal Heterojunction Coating and Moisture-Resistant Capping Layer," en, *Advanced Materials*, vol. 29, no. 15, p. 1606321, Apr. 2017.
- [52] X. Mu, X. Yu, D. Xu, X. Shen, Z. Xia, H. He, H. Zhu, J. Xie, B. Sun, and D. Yang, "High efficiency organic/silicon hybrid solar cells with doping-free selective emitter structure induced by a WO<sub>3</sub> thin interlayer," en, *Nano Energy*, vol. 16, pp. 54–61, Sep. 2015.
- [53] J. Chen, Y. Shen, J. Guo, B. Chen, J. Fan, F. Li, B. Liu, H. Liu, Y. Xu, and Y. Mai, "Electrochemical grafting passivation of silicon via electron transfer at polymer/silicon hybrid interface," en, *Electrochimica Acta*, vol. 247, pp. 826–834, Sep. 2017.
- [54] S. Jäckle, M. Liebhaber, C. Gersmann, M. Mews, K. Jäger, S. Christiansen, and K. Lips, "Potential of PEDOT:PSS as a hole selective front contact for silicon heterojunction solar cells," En, *Scientific Reports*, vol. 7, no. 1, p. 2170, May 2017.
- [55] Z. Yang, Z. Fang, J. Sheng, Z. Ling, Z. Liu, J. Zhu, P. Gao, and J. Ye, "Optoelectronic Evaluation and Loss Analysis of PEDOT:PSS/Si Hybrid Heterojunction Solar Cells," en, *Nanoscale Research Letters*, vol. 12, no. 1, p. 26, Dec. 2017.
- [56] D. Chapin, C. Fuller, and G. Pearson, "A New Silicon P-N Junction Photocell for Converting Solar Radiation into Electrical Power," *Journal of Applied Physics*, vol. 25, pp. 676–677, 1954.
- [57] D. L. Morel, A. K. Ghosh, T. Feng, E. L. Stogryn, P. E. Purwin, R. F. Shaw, and C. Fishman, "High-efficiency organic solar cells," en, *Applied Physics Letters*, vol. 32, no. 8, pp. 495–497, Apr. 1978.
- [58] R. O. Loutfy, J. H. Sharp, C. K. Hsiao, and R. Ho, "Phthalocyanine organic solar cells: Indium/  $x$  -metal free phthalocyanine Schottky barriers," en, *Journal of Applied Physics*, vol. 52, no. 8, pp. 5218–5230, Aug. 1981.
- [59] C. W. Tang, "Two-layer organic photovoltaic cell," en, *Applied Physics Letters*, vol. 48, no. 2, pp. 183–185, Jan. 1986.
- [60] M. A. Green, E. D. Dunlop, J. Hohl-Ebinger, M. Yoshita, N. Kopidakis, and A. W. Ho-Baillie, "Solar cell efficiency tables (Version 55)," en, *Progress in Photovoltaics: Research and Applications*, vol. 28, no. 1, pp. 3–15, Jan. 2020.
- [61] M. J. Sailor, E. J. Ginsburg, C. B. Gorman, A. Kumar, R. H. Grubbs, and N. S. Lewis, "Thin Films of n-Si/Poly-(CH<sub>3</sub>)<sub>3</sub>Si-Cyclooctatetraene: Conducting-Polymer Solar Cells and Layered Structures," en, *Science*, vol. 249, no. 4973, pp. 1146–1149, Sep. 1990.
- [62] C. H. Chen and I. Shih, "Hybrid organic on inorganic semiconductor heterojunction," en, *Journal of Materials Science: Materials in Electronics*, vol. 17, no. 12, pp. 1047–1053, Oct. 2006.

- [63] D. Zielke, R. Gogolin, M.-U. Halbich, C. Marquardt, W. Lövenich, R. Sauer, and J. Schmidt, “Large-Area PEDOT:PSS/*c*-Si Heterojunction Solar Cells With Screen-Printed Metal Contacts,” en, *Solar RRL*, vol. 2, no. 3, p. 1700191, Mar. 2018.
- [64] J. P. Thomas, L. Zhao, D. McGillivray, and K. T. Leung, “High-efficiency hybrid solar cells by nanostructural modification in PEDOT:PSS with co-solvent addition,” en, *Journal of Materials Chemistry A*, vol. 2, no. 7, p. 2383, 2014.
- [65] J. P. Thomas and K. T. Leung, “Defect-Minimized PEDOT:PSS/Planar-Si Solar Cell with Very High Efficiency,” en, *Advanced Functional Materials*, vol. 24, no. 31, pp. 4978–4985, Aug. 2014.
- [66] Q. Liu, T. Imamura, T. Hiata, I. Khatri, Z. Tang, R. Ishikawa, K. Ueno, and H. Shirai, “Optical anisotropy in solvent-modified poly(3,4-ethylenedioxythiophene):poly(styrenesulfonic acid) and its effect on the photovoltaic performance of crystalline silicon/organic heterojunction solar cells,” en, *Applied Physics Letters*, vol. 102, no. 24, p. 243902, Jun. 2013.
- [67] Y. Zhang, W. Cui, Y. Zhu, F. Zu, L. Liao, S.-T. Lee, and B. Sun, “High efficiency hybrid PEDOT:PSS/nanostructured silicon Schottky junction solar cells by doping-free rear contact,” en, *Energy & Environmental Science*, vol. 8, no. 1, pp. 297–302, 2015.
- [68] Y. Zhang, R. Liu, S.-T. Lee, and B. Sun, “The role of a LiF layer on the performance of poly(3,4-ethylenedioxythiophene):poly(styrenesulfonate)/Si organic-inorganic hybrid solar cells,” en, *Applied Physics Letters*, vol. 104, no. 8, p. 083514, Feb. 2014.
- [69] R. Gogolin, D. Zielke, W. Lövenich, R. Sauer, and J. Schmidt, “Silicon Heterojunction Solar Cells Combining an a-Si:H (n) Electron-collector with a PEDOT:PSS Hole-collector,” en, *Energy Procedia*, vol. 92, pp. 638–643, Aug. 2016.
- [70] Q. Liu, R. Ishikawa, S. Funada, T. Ohki, K. Ueno, and H. Shirai, “Highly Efficient Solution-Processed Poly(3,4-ethylenedioxythiophene):Poly(styrenesulfonate)/crystalline-silicon Heterojunction Solar Cells with Improved Light-Induced Stability,” en, *Advanced Energy Materials*, vol. 5, no. 17, p. 1500744, Sep. 2015.
- [71] J. He, Y. Wan, P. Gao, J. Tang, and J. Ye, “Over 16.7% Efficiency Organic-Silicon Heterojunction Solar Cells with Solution-Processed Dopant-Free Contacts for Both Polarities,” en, *Advanced Functional Materials*, vol. 28, no. 34, p. 1802192, 2018.
- [72] S.-S. Yoon and D.-Y. Khang, “High Efficiency (>17%) Si-Organic Hybrid Solar Cells by Simultaneous Structural, Electrical, and Interfacial Engineering via Low-Temperature Processes,” en, *Advanced Energy Materials*, vol. 8, no. 9, p. 1702655, Dec. 2018.

- [73] P. Yu, C.-Y. Tsai, J.-K. Chang, C.-C. Lai, P.-H. Chen, Y.-C. Lai, P.-T. Tsai, M.-C. Li, H.-T. Pan, Y.-Y. Huang, C.-I. Wu, Y.-L. Chueh, S.-W. Chen, C.-H. Du, S.-F. Horng, and H.-F. Meng, “13% Efficiency Hybrid Organic/Silicon-Nanowire Heterojunction Solar Cell *via* Interface Engineering,” en, *ACS Nano*, vol. 7, no. 12, pp. 10 780–10 787, Dec. 2013.
- [74] X. Dai, T. Chen, H. Cai, H. Wen, and Y. Sun, “Improving Performance of Organic-Silicon Heterojunction Solar Cells Based on Textured Surface *via* Acid Processing,” en, *ACS Applied Materials & Interfaces*, vol. 8, no. 23, pp. 14 572–14 577, Jun. 2016.
- [75] W.-R. Wei, M.-L. Tsai, S.-T. Ho, S.-H. Tai, C.-R. Ho, S.-H. Tsai, C.-W. Liu, R.-J. Chung, and J.-H. He, “Above-11%-Efficiency Organic–Inorganic Hybrid Solar Cells with Omnidirectional Harvesting Characteristics by Employing Hierarchical Photon-Trapping Structures,” en, *Nano Letters*, vol. 13, no. 8, pp. 3658–3663, Aug. 2013.
- [76] B. Ozdemir, M. Kulakci, R. Turan, and H. Emrah Unalan, “Silicon nanowire - poly(3,4-ethylenedioxythiophene)-poly(styrenesulfonate) heterojunction solar cells,” en, *Applied Physics Letters*, vol. 99, no. 11, p. 113 510, Sep. 2011.
- [77] L. He, Rusli, C. Jiang, H. Wang, and D. Lai, “Simple Approach of Fabricating High Efficiency Si Nanowire/Conductive Polymer Hybrid Solar Cells,” *IEEE Electron Device Letters*, vol. 32, no. 10, pp. 1406–1408, Oct. 2011.
- [78] S.-C. Shiu, J.-J. Chao, S.-C. Hung, C.-L. Yeh, and C.-F. Lin, “Morphology Dependence of Silicon Nanowire/Poly(3,4-ethylenedioxythiophene):Poly(styrene sulfonate) Heterojunction Solar Cells,” en, *Chemistry of Materials*, vol. 22, no. 10, pp. 3108–3113, May 2010.
- [79] J. P. Thomas, Q. Shi, M. Abd-Ellah, L. Zhang, N. F. Heinig, and K. T. Leung, “Charge Transfer in Nanowire-Embedded PEDOT:PSS and Planar Heterojunction Solar Cells,” en, *ACS Applied Materials & Interfaces*, vol. 12, no. 10, pp. 11 459–11 466, Mar. 2020.
- [80] T.-G. Chen, B.-Y. Huang, E.-C. Chen, P. Yu, and H.-F. Meng, “Micro-textured conductive polymer/silicon heterojunction photovoltaic devices with high efficiency,” en, *Applied Physics Letters*, vol. 101, no. 3, p. 033 301, Jul. 2012.
- [81] H. Jeong, H. Song, Y. Pak, I. K. Kwon, K. Jo, H. Lee, and G. Y. Jung, “Enhanced Light Absorption of Silicon Nanotube Arrays for Organic/Inorganic Hybrid Solar Cells,” en, *Advanced Materials*, vol. 26, no. 21, pp. 3445–3450, Jun. 2014.
- [82] J. He, Z. Yang, P. Liu, S. Wu, P. Gao, M. Wang, S. Zhou, X. Li, H. Cao, and J. Ye, “Enhanced Electro-Optical Properties of Nanocone/Nanopillar Dual-Structured Arrays for Ultrathin Silicon/Organic Hybrid Solar Cell Applications,” en, *Advanced Energy Materials*, vol. 6, no. 8, p. 1 501 793, Apr. 2016.
- [83] S. Thiyagu, B. Devi, Z. Pei, Y.-H. Chen, and J.-C. Liu, “Ultra-low reflectance, high absorption microcrystalline silicon nanostalagmite,” en, *Nanoscale Research Letters*, vol. 7, no. 1, p. 171, 2012.

- [84] R. Liu, S.-T. Lee, and B. Sun, “13.8% Efficiency Hybrid Si/Organic Heterojunction Solar Cells with MoO<sub>3</sub> Film as Antireflection and Inversion Induced Layer,” vol. 26, no. 34, pp. 6007–6012, Jul. 2014.
- [85] D. Chi, B. Qi, J. Wang, S. Qu, and Z. Wang, “High-performance hybrid organic-inorganic solar cell based on planar n-type silicon,” en, *Applied Physics Letters*, vol. 104, no. 19, p. 193 903, May 2014.
- [86] M. Pietsch, M. Y. Bashouti, and S. Christiansen, “The Role of Hole Transport in Hybrid Inorganic/Organic Silicon/Poly(3,4-ethylenedioxy-thiophene):Poly(styrene sulfonate) Heterojunction Solar Cells,” en, *The Journal of Physical Chemistry C*, vol. 117, no. 18, pp. 9049–9055, May 2013.
- [87] D. McGillivray, J. P. Thomas, M. Abd-Ellah, N. F. Heinig, and K. T. Leung, “Performance Enhancement by Secondary Doping in PEDOT:PSS/Planar-Si Hybrid Solar Cells,” en, *ACS Applied Materials & Interfaces*, vol. 8, no. 50, pp. 34 303–34 308, Dec. 2016.
- [88] M.-U. Halbach, D. Zielke, R. Gogolin, R. Sauer, W. Lövenich, and J. Schmidt, “Reduction of parasitic absorption in PEDOT:PSS at the rear of c-Si solar cells,” Lausanne, Switzerland, Aug. 2018, p. 040 008.
- [89] M.-U. Halbach, D. Zielke, R. Gogolin, R. Sauer-Stieglitz, W. Lövenich, and J. Schmidt, “Improved surface passivation and reduced parasitic absorption in PEDOT: PSS/ c-Si heterojunction solar cells through the admixture of sorbitol,” en, *Scientific Reports*, vol. 9, no. 1, p. 9775, Dec. 2019.
- [90] S.-S. Yoon and D.-Y. Khang, “Roles of Nonionic Surfactant Additives in PEDOT:PSS Thin Films,” en, *The Journal of Physical Chemistry C*, vol. 120, no. 51, pp. 29 525–29 532, Dec. 2016.
- [91] J. Wang, H. Wang, A. B. Prakoso, A. S. Togonal, L. Hong, C. Jiang, and N. Rusli, “High Efficiency Silicon Nanowire/organic Hybrid Solar Cell with Two-step Surface Treatment,” en, *Nanoscale*, Feb. 2015.
- [92] J. Sheng, K. Fan, D. Wang, C. Han, J. Fang, P. Gao, and J. Ye, “Improvement of the SiO<sub>x</sub> Passivation Layer for High-Efficiency Si/PEDOT:PSS Heterojunction Solar Cells,” en, *ACS Applied Materials & Interfaces*, vol. 6, no. 18, pp. 16 027–16 034, Sep. 2014.
- [93] Z. Ge, L. Xu, Y. Cao, T. Wu, H. Song, Z. Ma, J. Xu, and K. Chen, “Substantial Improvement of Short Wavelength Response in n-SiNW/PEDOT:PSS Solar Cell,” en, *Nanoscale Research Letters*, vol. 10, no. 1, p. 330, Dec. 2015.
- [94] K. Sato, M. Dutta, and N. Fukata, “Inorganic/organic hybrid solar cells: Optimal carrier transport in vertically aligned silicon nanowire arrays,” en, *Nanoscale*, vol. 6, no. 11, p. 6092, May 2014.

- [95] S.-S. Yoon, G.-R. Lee, and D.-Y. Khang, "Contact-printed ultrathin siloxane passivation layer for high-performance Si-PEDOT:PSS hybrid solar cells," en, *Microelectronic Engineering*, vol. 170, pp. 1–7, Feb. 2017.
- [96] Y.-H. Nam, J.-W. Song, M.-J. Park, A. Sami, and J.-H. Lee, "Ultrathin Al<sub>2</sub>O<sub>3</sub> interface achieving an 11.46% efficiency in planar n-Si/PEDOT:PSS hybrid solar cells," en, *Nanotechnology*, vol. 28, no. 15, p. 155402, Apr. 2017.
- [97] Z. P. Ling, Z. Xin, G. Kaur, C. Ke, and R. Stangl, "Ultra-thin ALD-AlO<sub>x</sub>/PEDOT:PSS hole selective passivated contacts: An attractive low cost approach to increase solar cell performance," en, *Solar Energy Materials and Solar Cells*, vol. 185, pp. 477–486, Oct. 2018.
- [98] D. Liu, Y. Zhang, X. Fang, F. Zhang, T. Song, and B. Sun, "An 11%-Power-Conversion-Efficiency Organic-Inorganic Hybrid Solar Cell Achieved by Facile Organic Passivation," *IEEE Electron Device Letters*, vol. 34, no. 3, pp. 345–347, Mar. 2013.
- [99] J. Liu, Y. Ji, Y. Liu, Z. Xia, Y. Han, Y. Li, and B. Sun, "Doping-Free Asymmetrical Silicon Heterocontact Achieved by Integrating Conjugated Molecules for High Efficient Solar Cell," en, *Advanced Energy Materials*, vol. 7, no. 19, p. 1700311, May 2017.
- [100] J. He, P. Gao, M. Liao, X. Yang, Z. Ying, S. Zhou, J. Ye, and Y. Cui, "Realization of 13.6% Efficiency on 20  $\mu\text{m}$  Thick Si/Organic Hybrid Heterojunction Solar Cells via Advanced Nanotexturing and Surface Recombination Suppression," *ACS Nano*, vol. 9, no. 6, pp. 6522–6531, Jun. 2015.
- [101] Z. Yang, P. Gao, J. He, W. Chen, W.-Y. Yin, Y. Zeng, W. Guo, J. Ye, and Y. Cui, "Tuning of the Contact Properties for High-Efficiency Si/PEDOT:PSS Heterojunction Solar Cells," en, *ACS Energy Letters*, vol. 2, no. 3, pp. 556–562, Mar. 2017.
- [102] A. Burgers, J. Eikelboom, A. Schonecker, and W. Sinke, "Improved treatment of the strongly varying slope in fitting solar cell I-V curves," in *Conference Record of the Twenty Fifth IEEE Photovoltaic Specialists Conference - 1996*, May 1996, pp. 569–572.
- [103] G. G. Malliaras, J. R. Salem, P. J. Brock, and J. C. Scott, "Photovoltaic measurement of the built-in potential in organic light emitting diodes and photodiodes," en, *Journal of Applied Physics*, vol. 84, no. 3, pp. 1583–1587, Aug. 1998.
- [104] Q. Chen, L. Mao, Y. Li, T. Kong, N. Wu, C. Ma, S. Bai, Y. Jin, D. Wu, W. Lu, B. Wang, and L. Chen, "Quantitative *operando* visualization of the energy band depth profile in solar cells," en, *Nature Communications*, vol. 6, no. 1, p. 7745, Nov. 2015.

- [105] R. Sinton, A. Cuevas, and M. Stuckings, “Quasi-steady-state photoconductance, a new method for solar cell material and device characterization,” in *Conference Record of the Twenty Fifth IEEE Photovoltaic Specialists Conference - 1996*, May 1996, pp. 457–460.
- [106] T. Trupke, R. A. Bardos, M. C. Schubert, and W. Warta, “Photoluminescence imaging of silicon wafers,” en, *Applied Physics Letters*, vol. 89, no. 4, p. 044 107, Jul. 2006.
- [107] T. Trupke, B. Mitchell, J. W. Weber, W. McMillan, R. A. Bardos, and R. Kroeze, “Photoluminescence Imaging for Photovoltaic Applications,” *Energy Procedia*, vol. 15, pp. 135–146, 2012.
- [108] A. Richter, S. W. Glunz, F. Werner, J. Schmidt, and A. Cuevas, “Improved quantitative description of Auger recombination in crystalline silicon,” en, *Physical Review B*, vol. 86, no. 16, p. 165 202, Oct. 2012.
- [109] J. Chen, L. Yang, K. Ge, B. Chen, Y. Shen, J. Guo, H. Liu, Y. Xu, J. Fan, and Y. Mai, “On the light-induced enhancement in photovoltaic performance of PEDOT:PSS/Si organic-inorganic hybrid solar cells,” en, *Applied Physics Letters*, vol. 111, no. 18, p. 183 904, Oct. 2017.
- [110] T. Dittrich, *Materials Concepts for Solar Cells*, en, 2nd ed. World Scientific (Europe), Apr. 2018.
- [111] R. Gogolin, D. Zielke, A. Descoeur, M. Despeisse, C. Ballif, and J. Schmidt, “Demonstrating the high Voc potential of PEDOT:PSS/c-Si heterojunctions on solar cells,” en, *Energy Procedia*, vol. 124, pp. 593–597, Sep. 2017.
- [112] Q. Liu, I. Khatri, R. Ishikawa, K. Ueno, and H. Shirai, “Effects of molybdenum oxide molecular doping on the chemical structure of poly(3,4-ethylenedioxythiophene): Poly(stylenesulfonate) and on carrier collection efficiency of silicon/poly(3,4-ethylene dioxythiophene): Poly(stylenesulfonate) heterojunction solar cells,” en, *Applied Physics Letters*, vol. 102, no. 18, p. 183 503, May 2013.
- [113] A. S. Erickson, A. Zohar, and D. Cahen, “N-Si-Organic Inversion Layer Interfaces: A Low Temperature Deposition Method for Forming a p-n Homojunction in n-Si,” en, *Advanced Energy Materials*, vol. 4, no. 9, p. 1 301 724, Jun. 2014.

# Appendix

## Deep Level Transient Spectroscopy

Deep Level Transient Spectroscopy (DLTS) can be used to get information about the traps/defects present in a material. By adjusting the voltage to probe different portions of the diode, information about the relative trap concentrations at the interface and in the bulk can be obtained. Figure 5.1 shows the change in capacitance,  $\Delta C$  measured for both the bulk and the interface, by courtesy of Espen Førdestrøm Verhoeven at the MiNa lab at UiO.

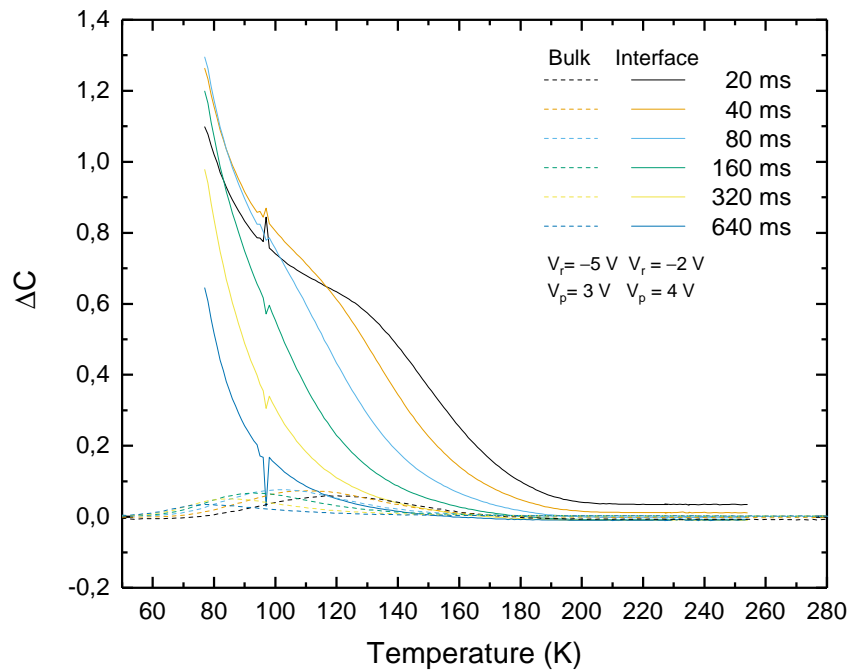


Figure 5.1: DLTS on a sample with Ag as front and back contact and a freshly grown native oxide layer between PEDOT:PSS and Si.

As expected, there is almost no change in the bulk since this is a high-quality Si wafer with a low defect concentration. At the interface, on the other hand, the downward slope from a peak is observed at 80–180 K. Unfortunately, the peak is positioned below the temperature limit for the setup used. Nevertheless, the results show that there are considerably more traps at the interface compared to the bulk.

Due to a lack of both features and time, this was not pursued any further.

## Sheet resistance and contact resistivity

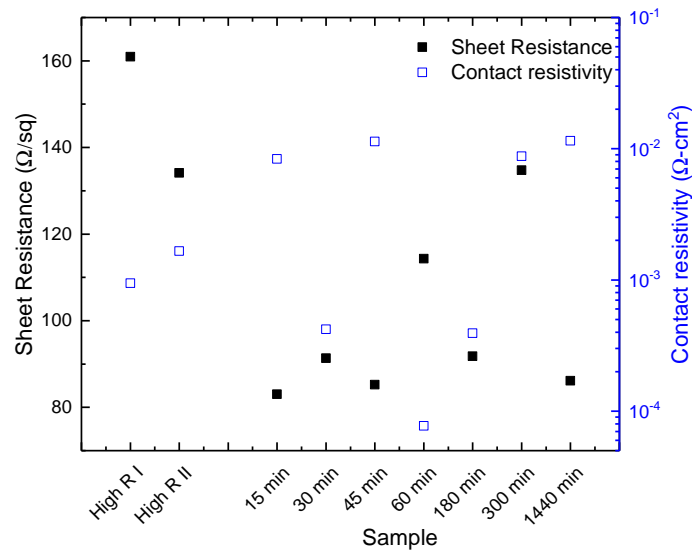


Figure 5.2: Sheet resistance from TLM measurements including PEDOT:PSS/ $\text{SiO}_2$ / $n$ -Si samples with various oxide growth times. Probably due to contributions from the wafers, the measurements from the different oxide thicknesses were inconclusive.

## Current-voltage of PEDOT:PSS on p-type silicon

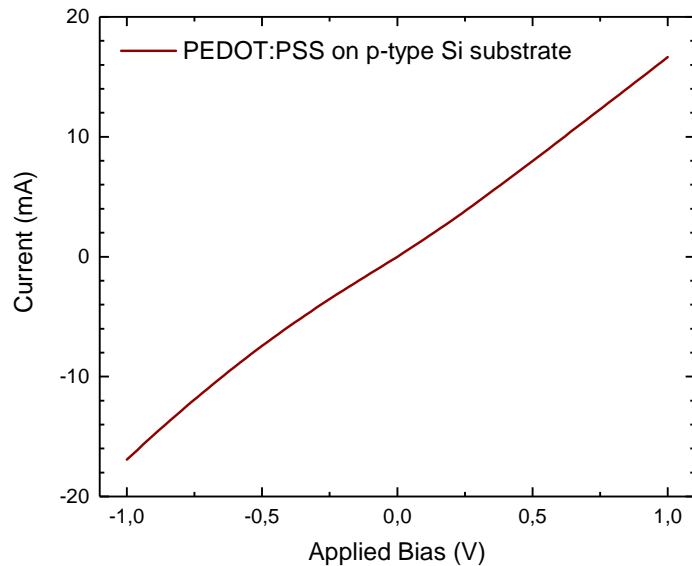


Figure 5.3: IV characteristics of PEDOT:PSS on p-type silicon. The measured diode shows near-perfect Ohmic behaviour which is expected for hole-conducting PEDOT:PSS on p-Si.